A.I. Alikhanyan **N**ational **S**cience **L**aboratory
(**Y**erevan **P**hysics **I**nstitute)

Yeranuhi Ghandilyan

COHERENT PHOTOPRODUCTION OF PROTON AND ANTI-PROTON PAIR ON DEUTERIUM WITH CLAS

A THESIS

for acquiring the degree of candidate of physical-mathematical sciences in division 01.04.16 “nuclear, elementary particles and cosmic ray physics”

Supervisor: **Stepan Stepanyan**
Thomas Jefferson National Accelerator Facility, Newport News, Virginia 23606

Yerevan – 2016

Contents

ACKNOWLEDGMENTS

First of all, I would like to gratefully and sincerely thank my scientific supervisor Stepan Stepanyan for his guidance, understanding and patience. I joined the group with little knowledge of computer programming and I have learned so much from him, which has enabled me to finish my analysis and PhD thesis. He provided me a large amount of time and effort for discussions and explanations of many things conserning to the CLAS eg3 run period and the data analysing. His mentorship was paramount in providing a well-rounded experience consistent my career goals. He encouraged me to not only grow as an experimentalist and physicist but also as an independent thinker. I am also thankful to him for daily issues. When we were away from home for 6 months, he like a parent has shown great care and attention to us; his students.

A very special thanks to Natalya Dashyan for giving me practical and detailed help, for her valuable advices and most important for her support when I didn't success she encouraged me to finish my analysis and PhD thesis. My academic style will be imprinted with her force for the years to come.

I'd like to thank A. I. Alikhanyan National Laboratory, especially those members of Lab#122 for their input, valuable discussions and accessibility. In particular I want to thank Nerses Gevorgyan for providing me helpful suggestions in computing system.

My gratitude goes to Hrant Gulqanyan, for being so supportive and assistance. I really appreciate his advices and remarks.

There are also a number of people who I would like to thank for reasons non related to physics. First and foremost, I need to thank my family for their faith in me. My parents, Sergo and Hasmik Ghandilyans, my sister and brother, Tatevik and Ruben, for their devotion and continuous support. I am deeply indebted to my parents for this life, the freedom to explore its meaning. They gave me a big love to the books, to science and they always encoriging

me for new achivements. Despite the dificult and challenging times in my country, they spared nothing for my education.

I am grateful to the members of my dissertation committee. Their academic support, input, and personal cheering are greatly appreciated.

Finally, I would like to thank all those people who helped me; my coworkers, my lovely friends.

I may have omitted some by accident. Please know I am truly appreciate everyone that has helped and supported me.

THESIS CONSTRUCTION

This thesis consists of Abstract, Introduction, five chapters, appendix and summary. The format will be as follows:

Abstract: Here we introduce the main goal of the work and result.

Introduction: In this section we presents the basic forces of nature, hadrons. Here we summarize the main idea of the thesis work.

Chapter 1: In this chapter we briefly indroduce the history of proton-antiproton studies, different hypothesis of narrow resonanseces of $p\bar{p}$ states, theoretical predictions and results.

Chapter 2: A description of CEBAF, Hall B, CLAS experimental apparatus will be given, including several major pieces.

Chapter 3: Here we describe the conditions during the CLAS eg3 run period.

Chapter 4: In this section we explain the analysis procedure in detail. Here we also present the event reconstraction procedures used to select and identify the reaction $\gamma d \rightarrow p\bar{p}d$, as well background reactions: $\gamma d \rightarrow \pi^+\pi^-d$ and $\gamma d \rightarrow K^+K^-d$. Here we also decsribe Monte Carlo simulations of the process.

Chapter 5: In this chapter we present and discus the experimental results.

Summary: Here we will provide a summary of our studies, results of the analysis and conclusions.

ABSTRACT

In this project coherent production of proton anti-proton pairs on deuterium with a high energy bremsstrahlung photon beam is studied. The main objective is to study claims of several groups on existence of two meson states, masses $\sim 2.02\ \mathrm{GeV}$ and $\sim 2.2\ \mathrm{GeV}$. Coherent production on deuterium has an advantage compared to the production on hydrogen. It will eliminate ambiguities in the production mechanism, since only t-channel production of $(\mathrm{p\bar{p}})$ is allowed.

Data from the CLAS detector at Jefferson Lab (TJNAF) has been analyzed. The experiment run in 2004-2005 with tagged bremsstrahlung photon beam of up to 5.5 GeV and a 40 cm long liquid deuterium target. During the experiment the CLAS torus magnet polarity was set to bend negatively charged particles outwards from the beam line. During the run the main trigger was tagger hodoscopes in relevant energy region in coincidence with three prong event in CLAS. The reactions $\gamma d \to p\bar{p}d$, $\gamma d \to \pi^+\pi^- d$, and $\gamma d \to K^+K^- d$ in fully exclusive final states has been analyzed, and the cross sections have been extracted.

INTRODUCTION

a) Fundamental Forces

Our Universe is governed by four basic forces: gravitational, weak, electromagnetic, and strong.

Gravitational Force: The gravitational force induced by the mass provides the stage of time and space for the other interactions. It forms stars, galaxies, and large-scale structures in the universe. The other three interactions, electromagnetic, weak and strong, govern the behavior of fundamental particles.

Electromagnetic Force: The matter around us in normal life is composed of atoms bound by electromagnetic interaction. The electromagnetic force binds nuclei and electrons together to form atoms, which are the building blocks of the matter.

Strong Force: The atom is composed of a nucleus and electrons orbiting it. The nucleus is composed of nucleons; protons and neutrons.The strong force holds quarks together to form nucleons and holds nucleons together to form nuclei, which are responsible for most of the mass in the visible universe.

Weak Force: Free neutrons can decay to protons and hyperons to nucleons, which are processes of weak interaction. The weak force changes quark flavors and breaks parity.

With the exception of gravity, the other three forces are unified in the Standard Model. How the strong interaction glues quarks together to form nucleons is still not understood in its full complexity. Only in short distances the strong interaction can be described in the language of a perturbative quantum field theory of Quantum Chromodynamics (pQCD) within the

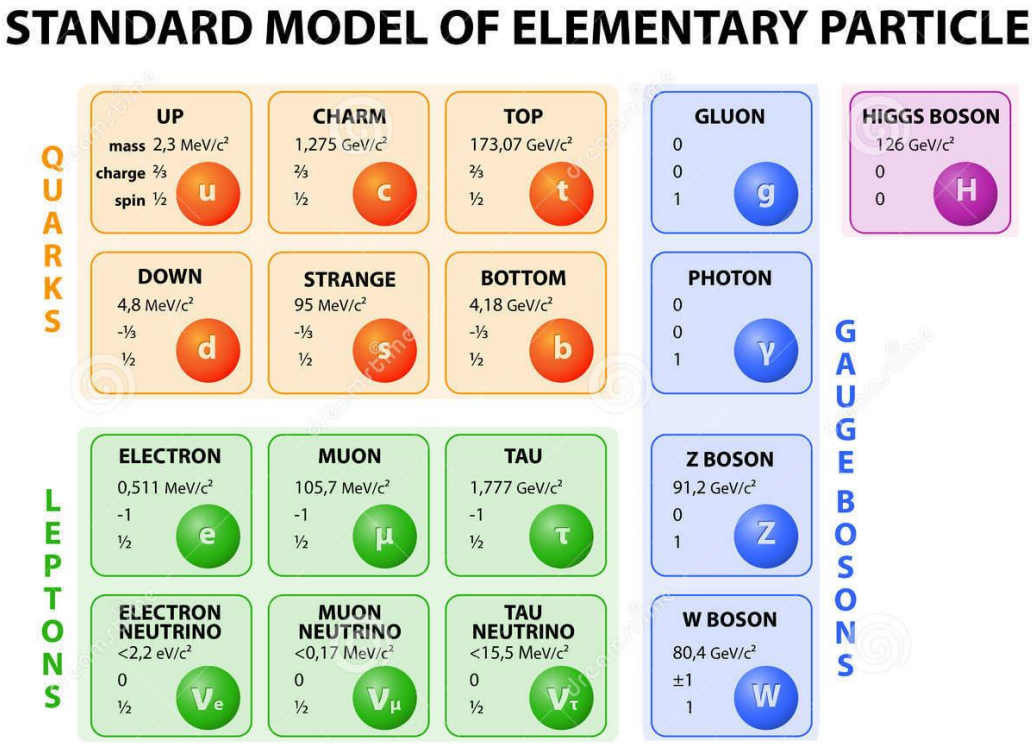

Figure a.1. The **Standard Model** table of elementary particles.

framework of the Standard Model of particle physics (**Fig. a.1**). The electromagnetic and weak force can be described by a single theory: the Quantum Electrodynamics (QED). The basic elements are quarks and leptons, and the force carriers are photon, W and Z bosons, and gluon.

b) Hadron Spectroscopy

Hadron spectroscopy is the study of hadrons, which are grouped into two categories, baryons and mesons. The hadrons are composed of quarks and gluons: baryons are composed of three quarks and mesons are composed of one quark and one antiquark. The baryon number is strictly conserved. It is defined as $B = \frac{1}{3}(n_q - n_{\bar{q}})$ and during the interaction, it is not violated. During the last half century, many new hadrons have been identified expanding our understanding of nature. A main goal of nuclear physics is the discovery and the study of forms of hadronic matter. This includes identifying new mesons and baryons, pure quarkless objects called glueballs, and other forms of exotic matter like gluonic hybrids, pentaquarks, and other multiquark states. The energy necessary to study these states scales with mass of resonances.

New hadrons can be produced through the use of high energy particle beams that interact with targets or other particle beams [**1.0**]. Examples of particle beams are electrons, photons, pions, protons, and antiprotons. These beams are used to produce many hadronic interactions, of which the byproducts are observed by particle detectors.

c) Reaction Mechanisms

Possible production mechanisms which describe the photoproduction of a proton-antiproton pair are diffraction (the exchange particle (like pomeron) carries the quantum number of vacuum), meson exchange (t-channel meson exchange assumes a meson exchange), baryon exchange, and antibaryon exchange. In each process, an intermediate resonance may be produced. We can search for these states first as structures in the invariant mass and angular distributions. As known, the momentum exchange variables are Mandelstam variables s,t, and u. These variables are numerical quantities that encode the energy, momentum, and angles of particles in a scattering process in a Lorentz-invariant fashion (**Figure c.1)**. The Mandelstam variables defined for a two-body final state, whereas our reaction has a three-body final state. The variables are defined by

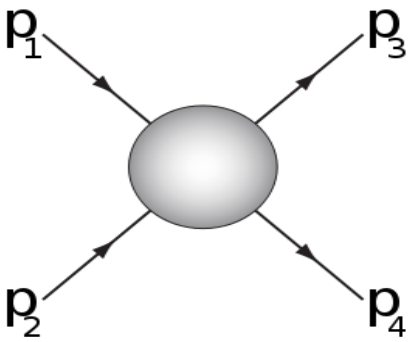

$$\mathbf{s} = (p_1 + p_2)^2 = (p_3 + p_4)^2$$

$$\mathbf{t} = (p_1 - p_3)^2 = (p_2 - p_4)^2$$

$$\mathbf{u} = (p_1 - p_4)^2 = (p_2 - p_3)$$

Figure c.1. The diagram of two-body reaction. This diagram illustrates how the Mandelstam variables are defined.

Where p_1 and p_2 are the four-momenta of the incoming particles and p_3 and p_4 are the four-momenta of the outgoung particles, and here we are using

relativistic units (c=1). **s** is also known as the square of the center-of-mass energy (invariant mass) and **t** is also known as the square of the four-momentum transfer. The Feynman diagram for these channels are represented in **Figure c.2.**

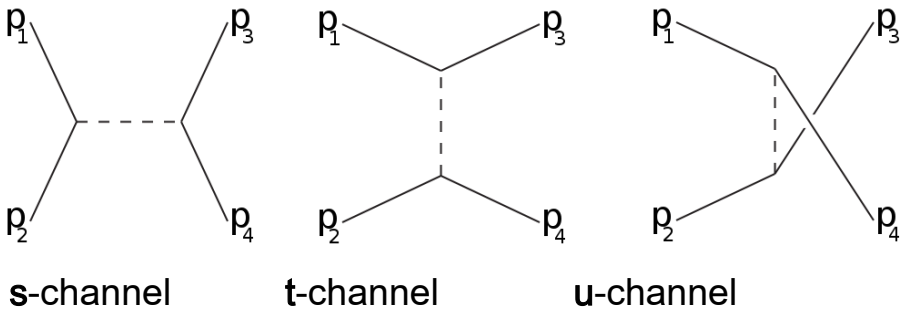

Figure c.2. The Feynman diagram for three s, t, u channels

d) This work

This thesis is dedicated to the study of meson states decaying to $p\bar{p}$. The results represented in this thesis are obtained by using data from CLAS eg3 run period, collected in 2004-2005 at Thomas Jefferson National Accelerator Facility (**TJNAF**). At Jefferson Lab, electrons are accelerated using the **C**ontinues **E**lectron **B**eam **A**ccelerating **F**acility (**CEBAF**). The experiment was done with a tagged bremsstrahlung photon beam of up to 5.5 GeV interacting wtih a 40 cm long liquid deuterium target. When the photon interacts with a deuterium, the products are projected forward into the CLAS detector, and the properties of those products are measured. In this work fully exclusive final state (all final state particles are detected) has been analyzed: $\gamma d \rightarrow d p\bar{p}$. When $p\bar{p}$ pair is produced on deuterium and there is no ambiguity in the production mechanism and only one diagram will contribute. In case of

hydrogen target there is a recoil and produced (decay) proton ambiguity and this is shown in **Figure d.1**. In our case only t-channel production of a neutral meson will remain (graph (a) of **Figure d.1**)

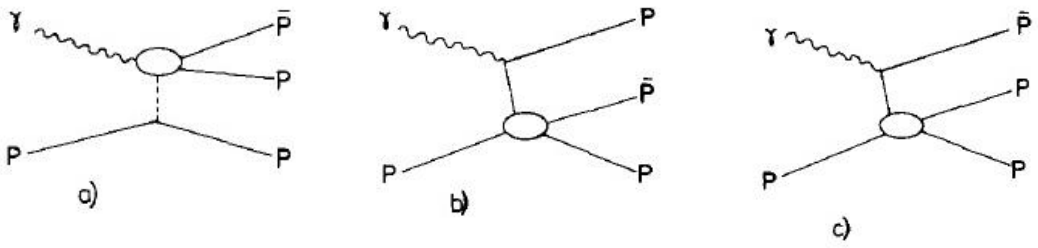

Figure d.1. Diagrams for proton antiproton photoproduction,
(a) t-channel diagram,
(b) antinucleon exchange diagram,
(c) nucleon exchange diagram [**1.11**]

Due to relatively high transfered momentum (t_{min}) in this reaction at available beam energies, deuterons are energetic enough and will be detected in CLAS. The goal of the project is to examine invariant mass distribution of the $p\bar{p}$. Depending on the available statistics, t-dependences of the cross section was studied as well.

In this work detail studies of two other coherent photoproduction reactions with $\pi^+\pi^-$ and K^+K^- final states have been performed since this exclusive final states can be reconstructed as $p\bar{p}$ due to particle misidentification. After the particle identification, detector efficiency was calculated with the standart sequence of programs: GSIM (GEANT simulation code of CLAS), GPP (GEANT Post Processor) and RECSIS (Reconstruction System).

Chapter 1

PHYSICS MOTIVATION AND HISTORICAL BACKGROUND

1.1 Physics Motivation

Meson spectroscopy plays an important role in hadron physics in particular for understanding the mechanism of confinement. It has been more than forty years since QCD was postulated as the theory of strong interactions. While much progress has been made in understanding perturbative phenomena, the non-perturbative regime, the regime of hadrons, has remained largely impervious to our varied assaults. There is a discrepancy between model predicted and experimentally observed baryon and meson states. One of unsolved mysteries is the lack of exotics, especially in light quark sector. These are states that are not a bound state of 3-quarks (baryon) or $q\bar{q}$ (mesons) but have, for example, explicit gluonic component (valence gluon). Such states are predicted in variety of QCD models, but have not been identified cleanly in experiments. In order to address these questions more studies of hadron spectroscopy with different production and decay modes are needed. One of interesting channels to look for exotic states is the proton-antiproton system. This channel has been studied for many years, using hadronic and electromagnetic probes. Some of experiments even reported evidences for resonance states, been as mesons or molecule-like baryonium states. However, there are no clear, high statistics proof of any of reported states. The debate on the existence of these states has greatly lingered on due to a lack of statistics, supporting evidence, and conflicting experimental results.

In this analysis, coherent production of hadron pairs, $p\bar{p}$, $\pi^+\pi^-$ and K^+K^-, on deuterium were studied with main focus on a possible production and decay of a mesonic state(s) to $p\bar{p}$. By saying "coherent" we understand that the target nucleus (in this case deuteron) stays intact. The reaction of interest is:

$$\gamma d \rightarrow h^+h^-d' \tag{1.1}$$

where h is the produced hadrons and the d′ is the recoil duteron. Coherent photoproduction of meson states often offers unique ways of pinning down production mechanism of otherwise complicated process. In this case, $p\bar{p}$ pair is produced coherently on deuterium and there is no ambiguity in the production mechanism and only one diagram will contribute (**Fig. 1.1**).

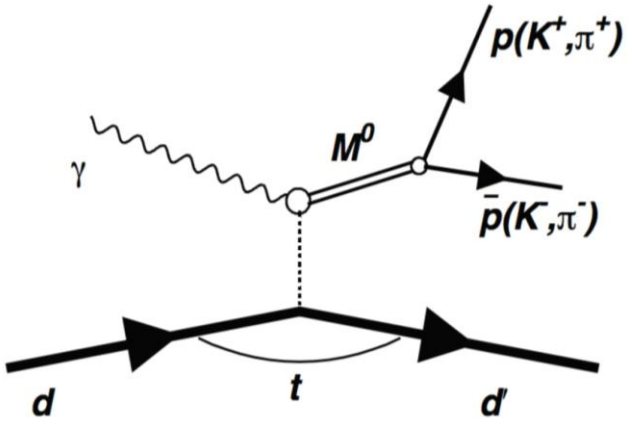

Figure.1.1. t-channel diagram for proton antiproton photoproduction

1.2 Historical Background

Search for states decaying to $p\bar{p}$ has a rich history spanning many

decades. First experimental evidences are cited as early as 60's, 70's [**1.1-1.8**] and 80's [**1.9-1.10**]. In the late 1960's there were claims of a meson resonance with a mass of 1.93 GeV/c^2 seen using a missing mass spectrometer at the European Center for Nuclear Research (**CERN**) [**1.1**]. In 1968, it was hypothesized that this narrow resonance was a baryonium particle when it was observed in a $p\bar{p}$ elastic scattering bubble chamber experiment at Brookhaven National Laboratory (BNL) [**1.2**]. This implies that it should be possible to produce the state in $p\bar{p}$ decays. There were then claims that other experiments found in the resonance in proton-antiproton scattering experiments [**1.4**][**1.5**][**1.6**]. Beginning in the late 1970s there were additional claims of higher mass resonances at 2.02 and 2.20 GeV/c^2 in the proton-antiproton system [**1.7**][**1.8**][**1.11**]. However, subsequent experiments refuted these claims [**1.3**][**1.9**], and until recently the debate had diminished. Later experiments, e.g. [**1.12**], confirm existence of a state at 2.02 GeV. Recently BELLE published observation of $B \rightarrow p\bar{p}K^{\pm}$ [**1.13**], where they examine $p\bar{p}$ mass spectrum and found that it is inconsistent with phase space and is peaked towards low mass. Similar results were obtained by BES collaboration [**1.14**] in the analysis of $J/\Psi \rightarrow \gamma\, p\bar{p}$, where they reported a peak below $2m_p$ at M = 1.859 GeV.

From the study of the reaction $\pi^- p \rightarrow p_F p\bar{p}\pi$ using a fast proton (p_F) trigger device in the CERN Omega spectrometeter [**1.7**], the group find evidence of two narrow $p\bar{p}$ states produced mainly in association with a $\Delta^0(1232)$ and a $N^0(1520)$. This experiment was done with a π^- beam at 9 and 12 GeV/c interacting on a hydrogen target. The trigger required a fast proton emitted forward (±150 mrad) with a momentum greater than $P_{beam}/2$. This was ensured by two large aperture Cerenkov counters and by logic matrices associated to MWPC (**m**ulti-**w**ire **p**roportional **c**hamber) and and scintilation

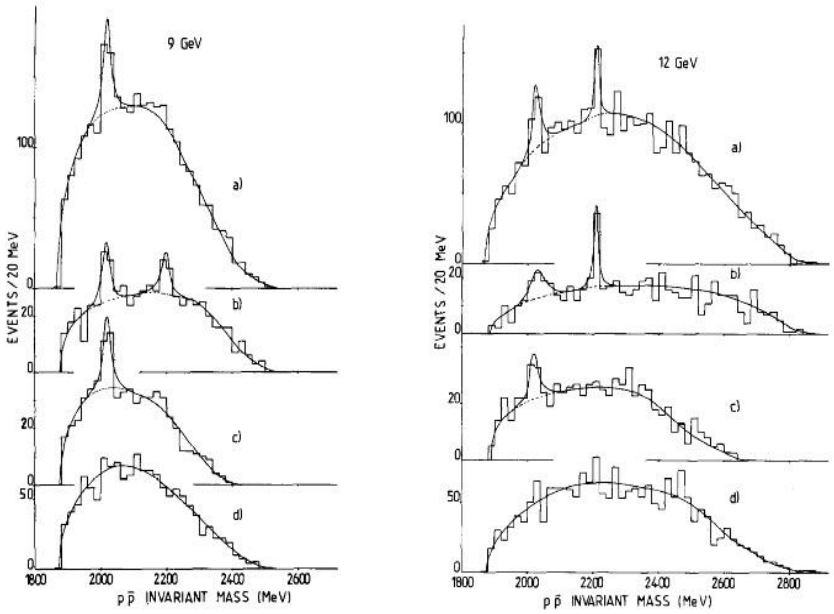

Figure. 1.2
Left: The distribution of the $p\bar{p}$ invariant mass at 9 GeV/c.
Right: The distribution of the $p\bar{p}$ invariant mass at 12 GeV/c.
(a) All the events.
(b) Events with invariant mass $p_F\pi^-$ in $\Delta^0(1232)$ region.
(c) Events with invariant mass $p_F\pi^-$ in the $N^0(1520)$ region.
(d) Events with invariant mass $p_F\pi^-$ outside the regions of **b)** and **c)**

keep the same hodoscopes. To keep the acceptance roughly the same at 9 and 12 GeV/c, the magnetic field intensity of the Omega magnet was reduced in the 9 Gev/c run. In **Fig. 1.2** we can see resultes which are part of a general experiment made with the CERN Omega spectrometer.

Masses and natural widths of these resonanses are respectively M_1= 2020±3MeV , Γ_1= 24±12MeV and M_2= 2204 ± 5MeV , Γ_2=16^{+20}_{-16} Mev.

Beggining in the late 1970s there were additional claims of higher mass resonances at 2.02 GeV/c^2 and 2.20 GeV/c^2 in the proton-antiproton scattering experiments [**1.4**], [**1.7**], [**1.8**]. In their work A.S. Carrol **[1.4]** have observed structures in $p\bar{p}$ and $d\bar{p}$ total cross sections at the same mass. In an attempt to clarify the problem of the possible existence of meson resonances in the mass region around 1950 MeV/c^2, they have measured $p\bar{p}$ and $d\bar{p}$ total cross sections using antiprotons of momenta 360 to 1050 MeV/c (center-of-mass total energies between 1910 and 2100 MeV/c^2).

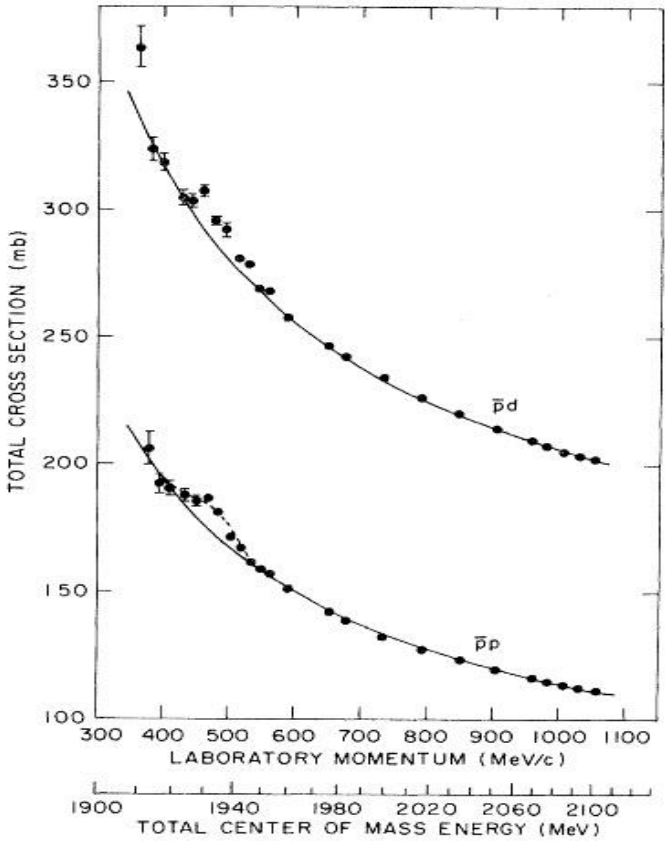

Figure.1.3 Results of the experiment for $\mathbf{p\bar{p}}$ and $\mathbf{d\bar{p}}$ total cross section.

The experiment was carried out in a partially separated beam produced from a target in the slow external beam of the Brookhaven National Laboratory alternating gradient synchrotron. The hydrogen, deuterium, and vacuum targets were 3 ft long for measurements above 680 MeV/c. For the $\bar{p}p$ mass 1932 (±2) MeV/c^2, width 9^{+4}_{-3} MeV/c^2, cross section: $\sigma=18^{-3}_{+6}$ mb. These structures could be one or more meson resonanses. The data suggest that the structures are in the isospin -1 states (**Figure. 1.3**).

The Belle collaboration **[1.13]** report the observation of the decay mode

$B^{\pm} \to p\bar{p}K^{\pm}$ and $B^{0} \to p\bar{p}K_S$. The group used a 29.4 fb^{-1} data sample, which contains 31.9 million produced $B\bar{B}$ pairs, collected with the Belle detector at **KEKB** asymmetric-energy e^+e^- (3.5 on 8 GeV) collider. The $p\bar{p}$ mass spectrum in this decay is inconsistent in phase space and is peaked at low mass. In **Figure 1.4** is shwon the signal yield as a function of $p\bar{p}$ invariant mass. ΔE and beam-constrained mass distributions for the signal candidates.

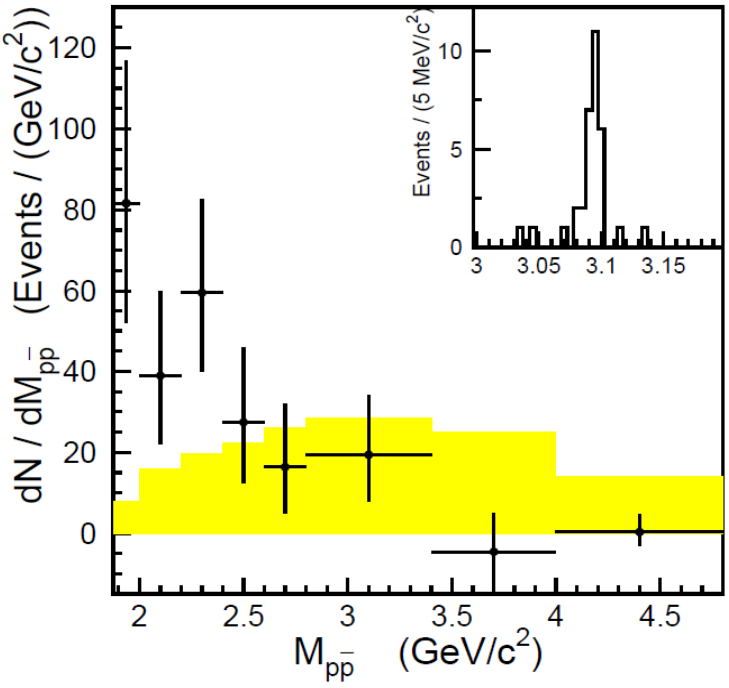

Figure. 1.4 The fitted yield divided by the size for $B^{+} \to p\bar{p}K^{+}$ as a function $p\bar{p}$ mass.

The Bes collaboration **[1.14]** observed a narrow enhancement near $2m_p$ in the invariant mass spectrum of $p\bar{p}$ pairs from radiative $J/\psi \rightarrow \gamma p\bar{p}$ decays. No similar structure is seen in $J/\psi \rightarrow \pi^0 p\bar{p}$ decays. The results were based on an analysis of a 58 million event sample of J/ψ decays accumulated with the BESSII detector at the Beijing electron-positron collider. There is an accumulation of evidence for anomalous behavior in the proton-antiproton $(p\bar{p})$ system very near the $M_{p\bar{p}} = 2m_p$ mass threshold. In studies of $\bar{p}$ annihilations at rest in deuterium, anomalies in the charged pion momentum spectrum from $pd \rightarrow \pi^-\pi^0 p$ and $\pi^+\pi^- n$ [**1.15**] reactions and the proton spectrum from $\bar{p}d \rightarrow p2\pi^+3\pi^-$ [**1.16**] have been interpreted as effects of narrow, below-threshold resonances. There are no well established mesons that could be associated with such states. The proximity in mass to $2m_p$ is suggestive of nucleon-antinucleon $(N\bar{N})$ bound states. In **Figure 1.5** is shown the $p\bar{p}$ invariant mass distribution for surviving events. As we can see, the distribution has a peak near $M_{p\bar{p}} = 2.98$ GeV/c^2 , a broad enhancement around $M_{p\bar{p}}$ ~ 2.2 GeV/c^2 , and a narrow, low-mass peak at the $p\bar{p}$ mass threshold.

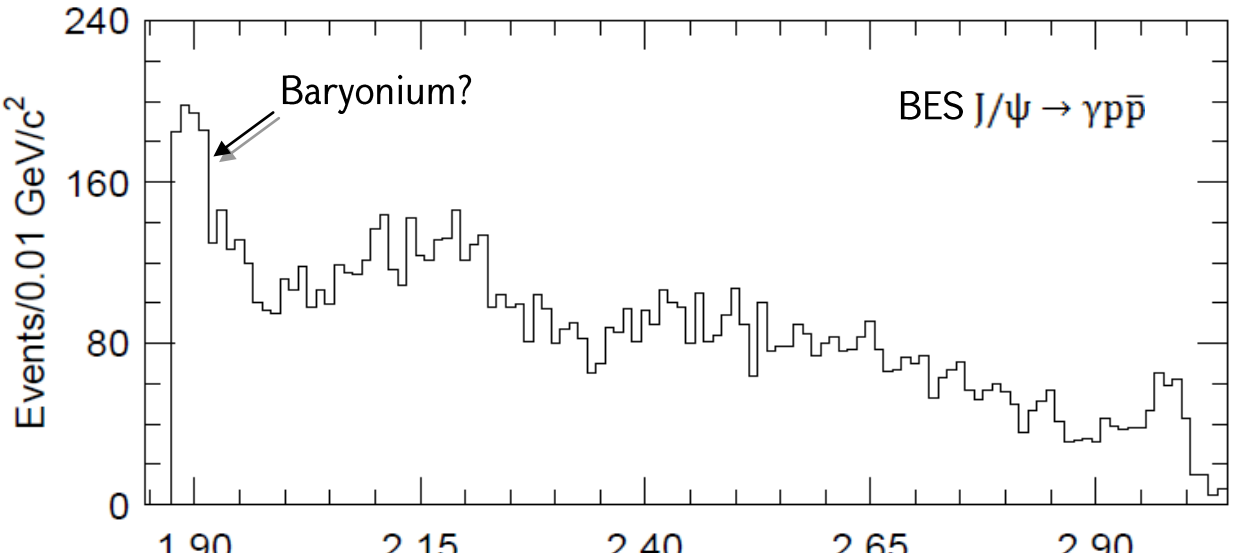

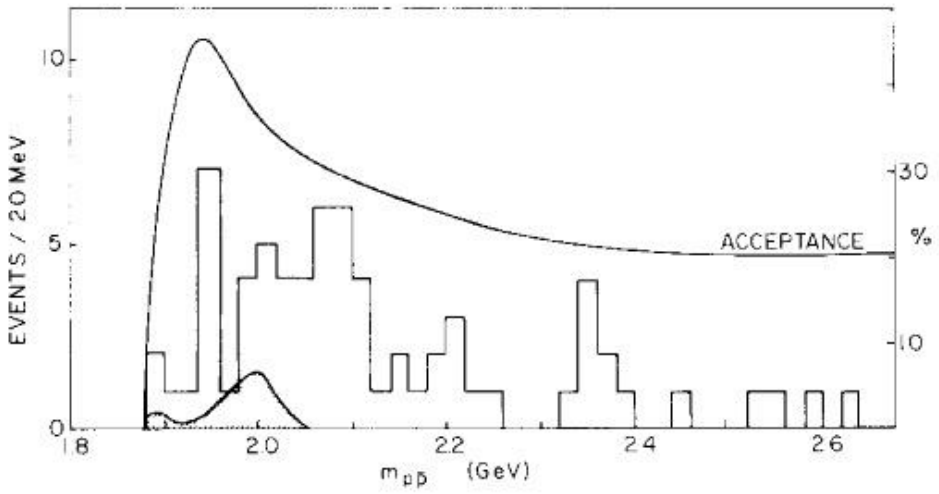

Figure. 1.6. Invariant mass spectrum for elastically produced $p\bar{p}$ pairs (69 events), background and overall acceptance.

Also an experiment was done on CERN OMEGA spectrometer and the results published by D. Aston et all [**1.10**]. The data were recorded at the CERN SPS (**S**uper **P**roton **S**ynchrotron), using a tagged photon beam with the Omega Spectrometer. The exclusive $\gamma(p) \rightarrow p\bar{p}(p)$ was recorded by trigger requiring a multiplicity of 2 forward charged particles passing through the system, with no light detected in Cherenkov counter. The $p\bar{p}$ mass $m_{p\bar{p}}$ is shown in figure bellow (**Fig.1.6**), together with the calculated background and the overall aacceptance for recording and identifying the event.

The other results from a photoproduction experiment studing the reaction $\gamma p \rightarrow p p \bar{p}$ was performed at 7 GeV Electron Synchrotron DESY at Hamburg. The bremsstrahlung photon beam was in the energy range $4.74 \leq E\gamma \leq 6.55$ GeV. Experimental tools used in this experiment were a Cherenkov counter, a magnetic wire chamber spectrometer and a time-of-flight facility.

Other experiments with lower statistics supported the 2.02 GeV/c^2 resonance [**1.8**][**1.11**], but an experiment at BNL [**1.9**] refuted these claims. The BNL experiment observed approximately 7000 events of the type $\pi^- p \rightarrow \pi^- p_F p \bar{p}$. They did not observe resonances, and an upper limit of 3nb was placed on the resonance cross section.

The first experiment to produce proton-antiproton pairs via photoproduction used the 7 GeV electron Synchrotron DESY at Hamburg in 1983 [**1.11**]. The experiment recorded 230 events of the $\gamma p \rightarrow p p \bar{p}$. The experiment claimed to observe a $p\bar{p}$ resonance with a mass of 2.024 GeV/c^2 with a width of 27 MeV/c^2 (**Fig.1.7**), and a cross section of 14±5 nb.

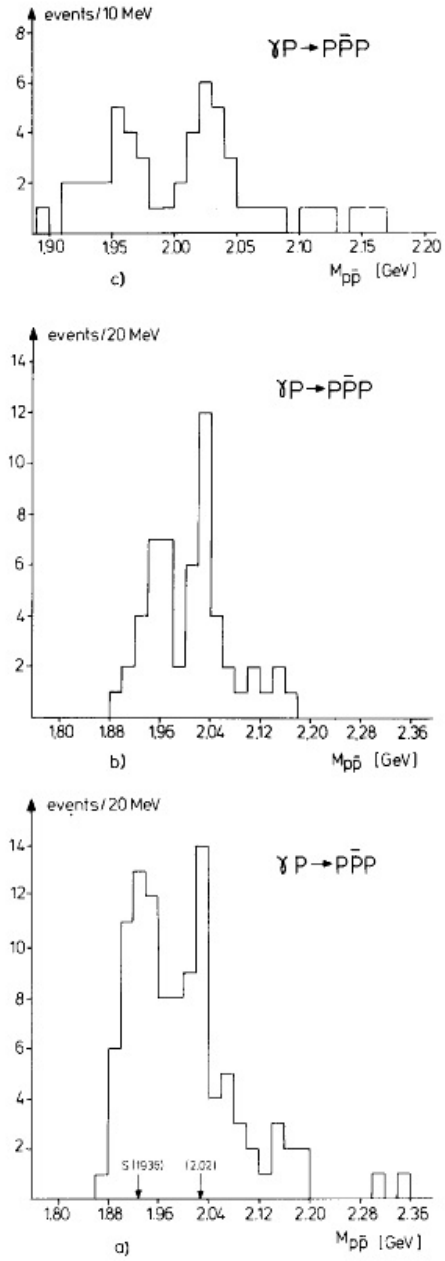

Figure. 1.7. Distribution of the invariant $p\bar{p}$ mass of events with fast protons (>2 GeV).
(a) uncut, uncorrected $p\bar{p}$ mass distribution,
(b) 50^0 cut around the helicity axis,
(c) distribution 3b plotted in 10 MeV bins.

Chapter 2

CEBAF and CLAS

2.1 TJNAF (Thomas Jefferson National Accelerator Facility)

The experiment was carried out in Hall B at the Thomas Jefferson National Accelerator Facility (TJNAF), also known as Jefferson Laboratory or JLab, in Newport News, Virginia, USA. A view of the facility is shown in **Figure 2.1**.

Figure 2.1: Thomas Jefferson National Accelerator Facility

At TJNAF, the linear Continuous Electron Beam Accelerator Facility (CEBAF) can deliver a high-intensity electron beams to the three experimental Halls A, B, and C (since 2014 Hall D have been constructed on the opposite end of the accelerator from the other three halls) simultaneously, with mostly independent beam parameters. A schematic layout of the machine and

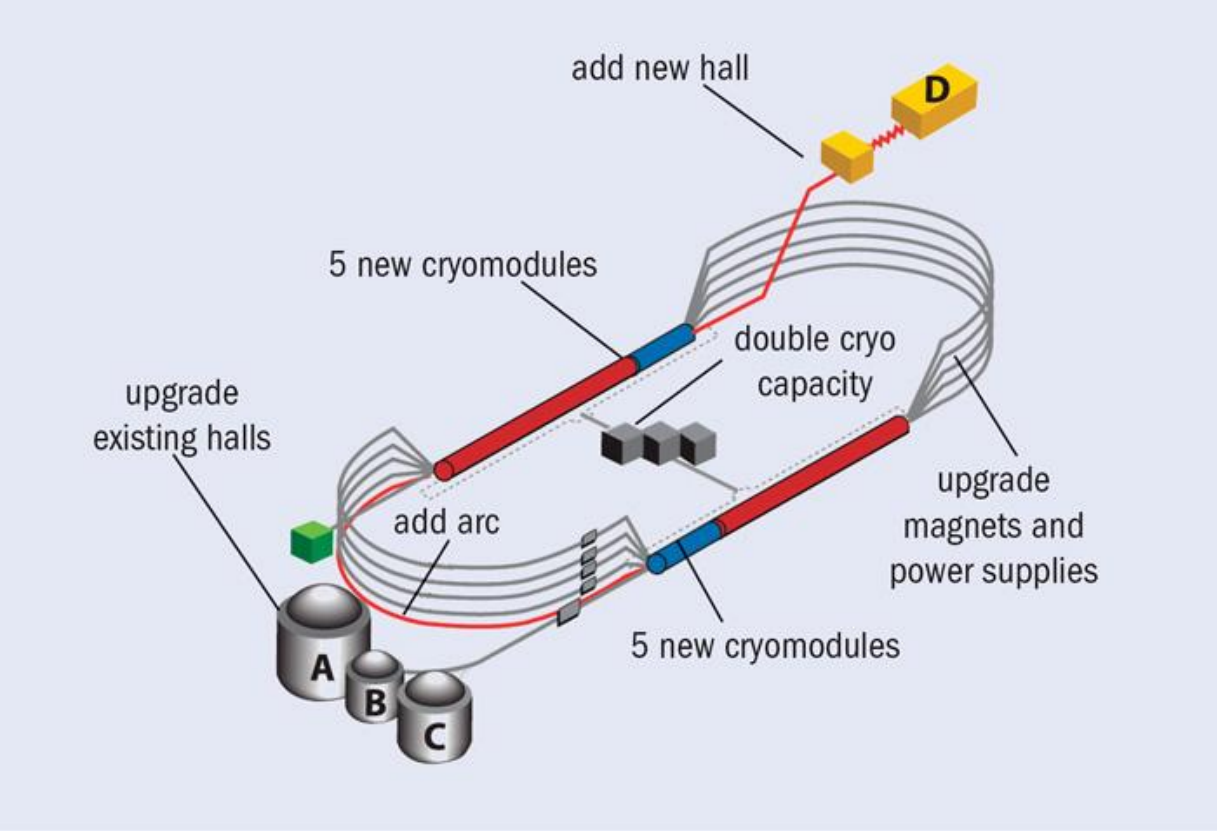

Figure 2.2: Layout of **T**homas **J**efferson **N**ational **A**ccelerator **F**acility, showing injector, linear accelerator, recirculation arcs and three halls (Now they are 4)

experimental hals is shown in **Figure 2.2**. All halls have fixed targets. Hall A and Hall C have small-angle detectors dedicated for hadrons and electrons separately, whereas Hall B has a spherical detector of large acceptance covering almost 4π solid angle to detect multiple particles.

2.2 CEBAF (Continues Electron Beam Accelerator Facility)

The superconducting radio frequency (RF) Continuous Electron Beam Accelerator Facility (CEBAF) is an underground, racetrack shaped electron accelerator capable of producing a continuous wave electron beam up to nearly 6 GeV in energy. The CEBAF is for investigation of the electromagnetic structure of mesons, nucleons, and nuclei. Beams supplied to Halls A and C can range between 1 and 200 μA, and between 1 and 200 nA in Hall B **[2.1]** The accelerator is illustrated in **Figure 2.3**. The primary electron beam from the CEBAF accelerator can be separated and sent to three different experimental areas for simultaneous experiments.

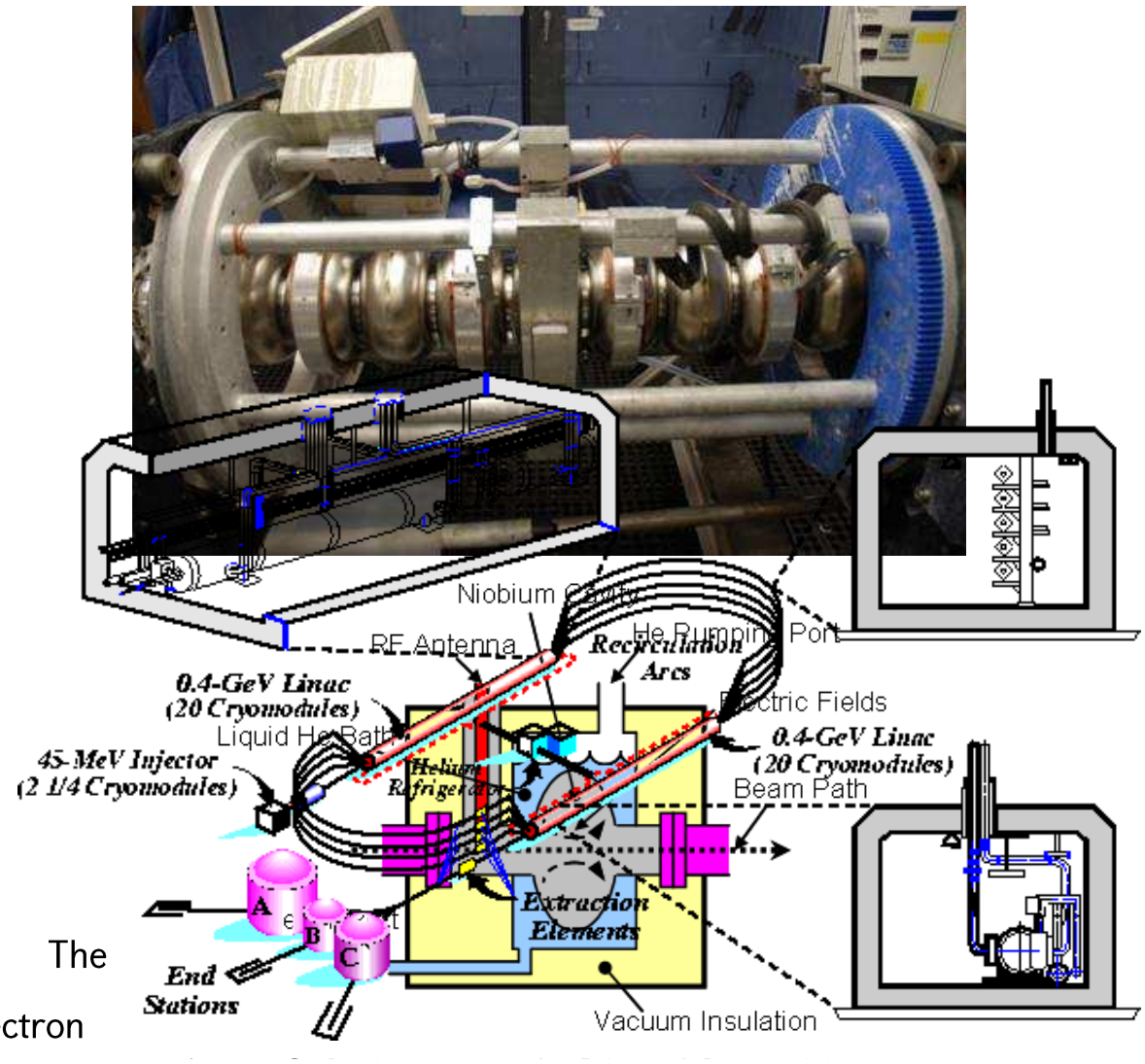

Figure 2.3 How **CEBAF** works

The electron beam starts from the injector. The electrons are generated by shining a pulsed laser on a GaAs photocathode and then accelerated to 45 MeV by going through 2 and 1/4 **SRF** (**S**uperconducting **R**adio **F**requency) cavities (**Figure 2.4**), which allow for continuous, high-gradient acceleration.

With the usage of the SRF cavities, the accelerator can deliver ”continuous” electron beams. The laser pulses generate electron bunches for each experimental hall every 2.004 ns.

The injector system then cleanly separate the bunches before recirculating them through the linear accelerators (LINACs) of CEBAF **Figure 2.3**.

There are two LINACs, and each LINAC has 168 SRF cavities. The cavity temperature is at 2K using liquid helium to maintain its superconducting state. In the cavities, the acceleration of the electron beam by RF electromagnetic standing waves does not depend on the speed of electrons once they have

reached the 45 MeV provided by the injector and hence close to the speed of light.

It is counted as one pass for an electron to go through both LINACs after bending by the recirculation arcs. Each LINAC can accelerate electrons by ~600 MeV. After one pass, the electrons gain ~1.2 GeV. Currently CEBAF can operate at up to 5 passes so electron beam energies can reach 6 GeV before delivery to each experimental hall by extraction elements.

The acceleration process was carefully designed to focus electrons into beam buckets, and each bunch has a width of only several picoseconds.

2.3 CLAS (CEBAF Large Acceptance Spectrometer)

The Hall-B houses CEBAF Large Acceptance Spectrometer (CLAS) [**2.1**]. Detector CLAS is a spherical, multi-component detector system as shown in **Figure 2.5**. It detects charged and neutral particles produced by the interaction of electrons or photons with a cryogenic target placed in the beam path near the center of CLAS.

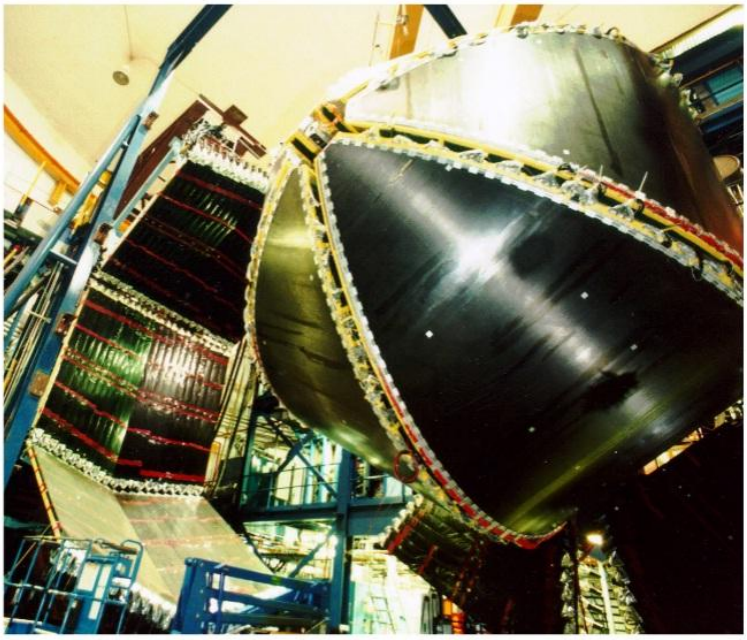

Figure 2.5 A picture of **CLAS**. The drift chamber detectors (**DC**) are closed inside, and the time-of-flight detectors **(TOF)** are opened up and peeled away.

2.3.1 Main Detector Components

The main components of CLAS include a superconducting torus magnet (Torus) [**2.1**], drift chambers (DC) [**2.2**] to determine charged particle's trajectory, a gas Cherenkov counter (CC) [**2.3**] for electron indentification, time-of-flight scintillator counters (SC) [**2.4**] and an electromagnetic calorimeter (EC) [**2.5**] to detect showering particles (electrons and photons) and neutrons. In the experiment with photon beams a start counter (ST) [**2.6**] is used to provide the time at the production vertex. An illustration of the main components and a cut view are shown in **Figure. 2.6** and **Figure. 2.7**.

As near 4π detector, CLAS has each of its components split in 6 sectors as shown in **Figure 2.6**. The segments are individually instrumented to form six essentially independent magnetic spectrometers with a common target, trigger and data-acquistion (DAQ) system.

The reasons for this design were the ability to measure charged particles with good momentum resolution, provide geometrical coverage of charged particles to large angles in the laboratory frame, and keep a magnetic-field-free

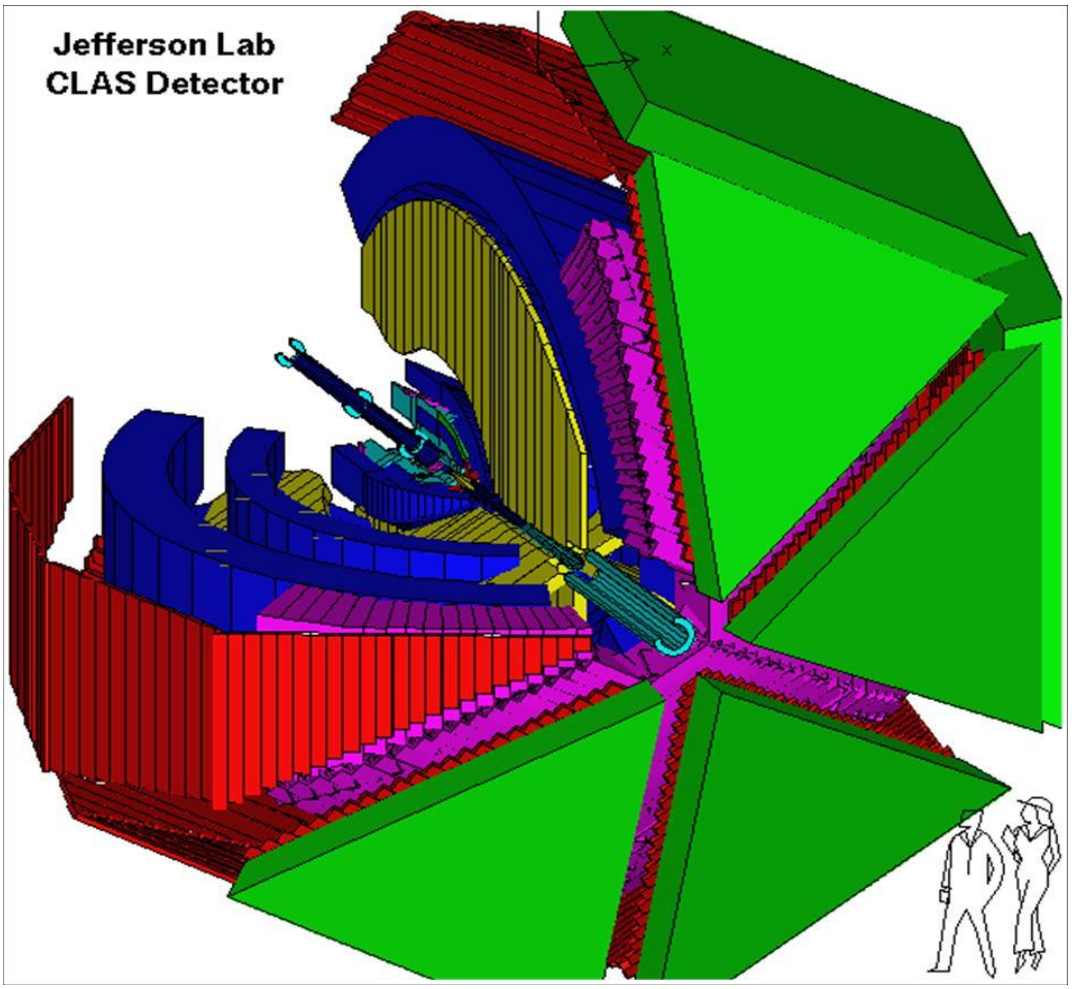

Figure 2.6 Side view of the **CLAS** detector in Hall B beamline and associated equipment.

region around the target to allow the use of dynamically polarized targets. A view of the CLAS detector, its associated equipment, and the beamline is shown in **Figure 2.7** and **Figure 2.8**.

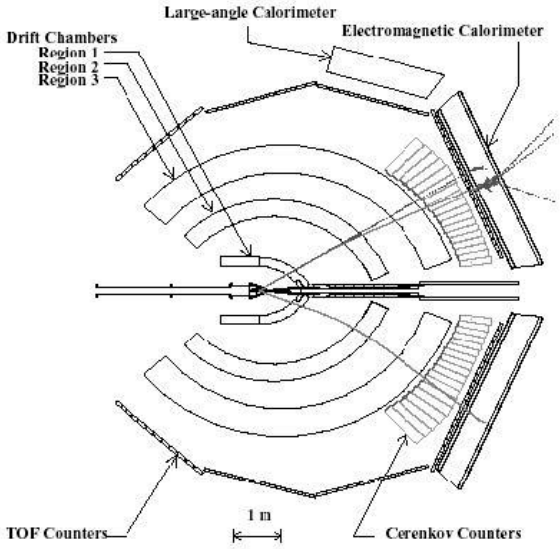

Figure 2.7 A sample trajectories of charged particles

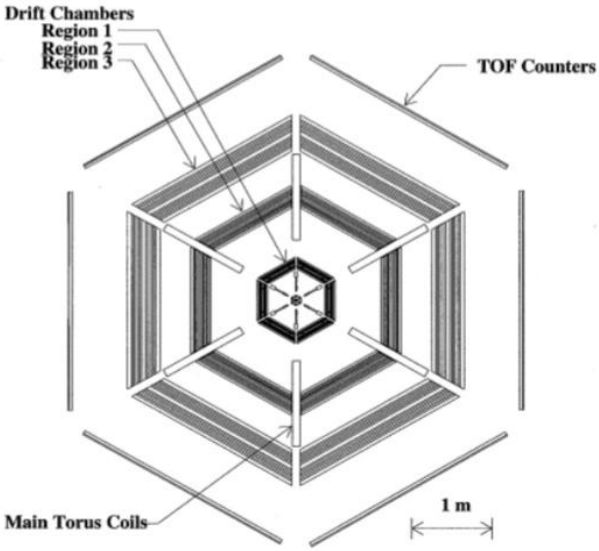

Figure 2.8 Azimuthal view of the **CLAS** detector. The six sectors are shown.

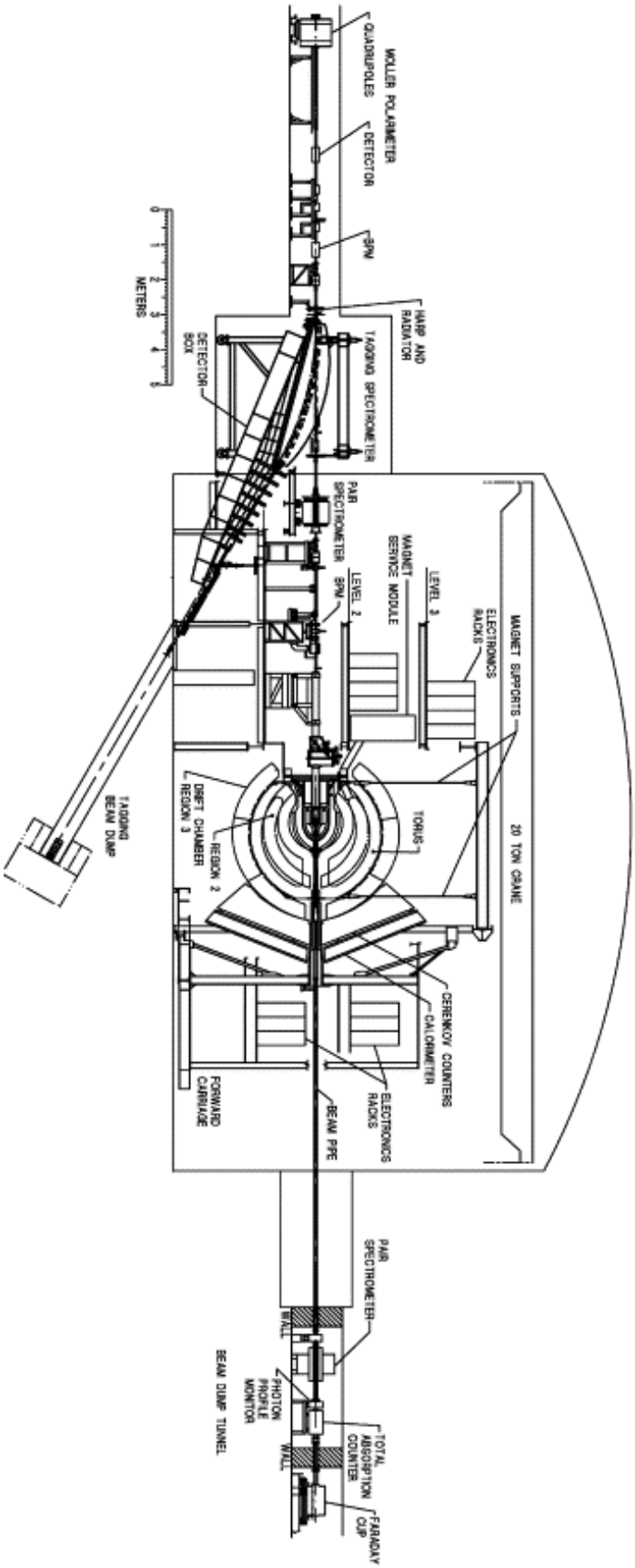

Figure 2.9 Side view of the **CLAS** detector in Hall B with beamline and associated equipment.

2.3.2 The Torus Magnet

The detector itself is designrd around six superconducting coils that produce an azimuthal magnetic field surrounding the beam line. This field bends charged particles going through the drift chambers for momentum measurements. The CLAS toroidal magnet bends charged particles toward or away from the beam axis but leaves the azimuthal angle essentially unchanged. As seen in **Figure 2.10**, the magnetic field from the superconducting torus coils is negligible in the region near the beam line, allowing for the use of polarized targets. The coils are approximately five meters in length. The field reaches 2.5 Tm in the forward region, dropping to 0.6 Tm at a 90^{o} scattering angle. All non-active parts of the detector, such as the Cherenkov counter, photomultiplier tubes, and the drift chamber support structure are confined to the shadow of the torus coils to provide maximum angular resoution.

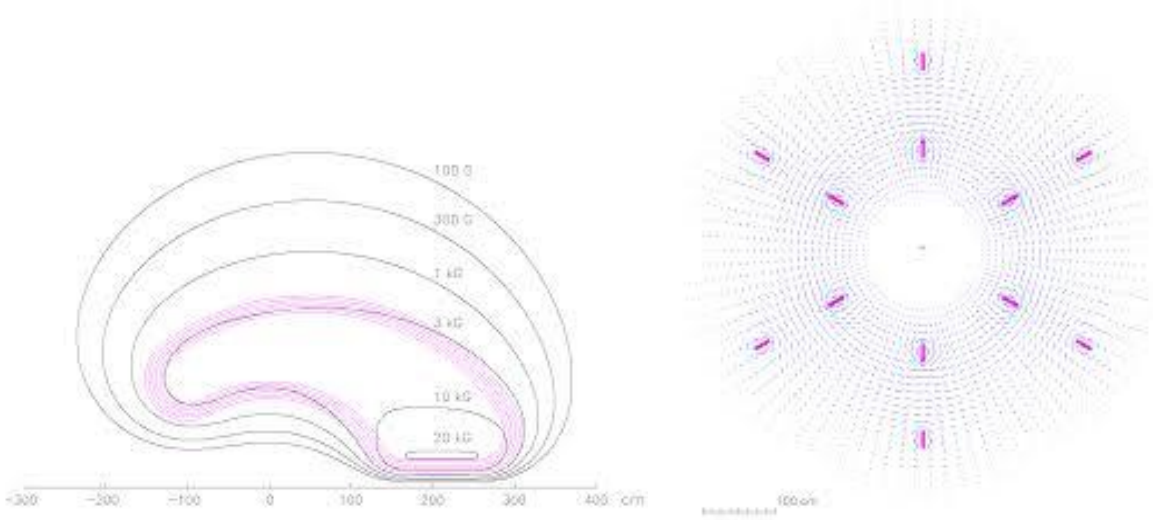

(A) (B)

Figure 2.10 (A) Magnetic field strength in the plane between two of the torus coils. The concentration of violet lines is the projection of the coils midplane. (B) Magnetic field vectors in the cross section of **CLAS** perpendicular to the beam line.

2.3.3 The Drift Chamber

The drift chambers in CLAS are designed to provide good position resolution and efficiency while maintaining a large acceptance [**2.2**]. The six superconducting coils split the detector into six separate tracking sectors. In each sector the drift chambers are divided into three regions, located at different distances from the beam line. The chambers span from 8° to 145° in polar angle ($8^{\circ} < \Theta < 142^{0}$) from the beam line, while the azimuthal coverage per sector is ~50°, giving a total of 300° (out of 360°). The missing azimuthal coverage is due to the presence of the magnet coils, and while strictly not constant in θ, the angles quoted here are a reasonable estimate. Overall, CLAS covers ~74% of 4π. **Figure 2.7** and **Figure.2.8** illustrate the curved shape and location of the drift chamber regions within the CLAS detector. In the drift chambers, wire layers are arranged such that the wires form a hexagonal pattern. In this arrangement there are six field wires surrunding each sense wire, as shown in **Figure 2.11**.

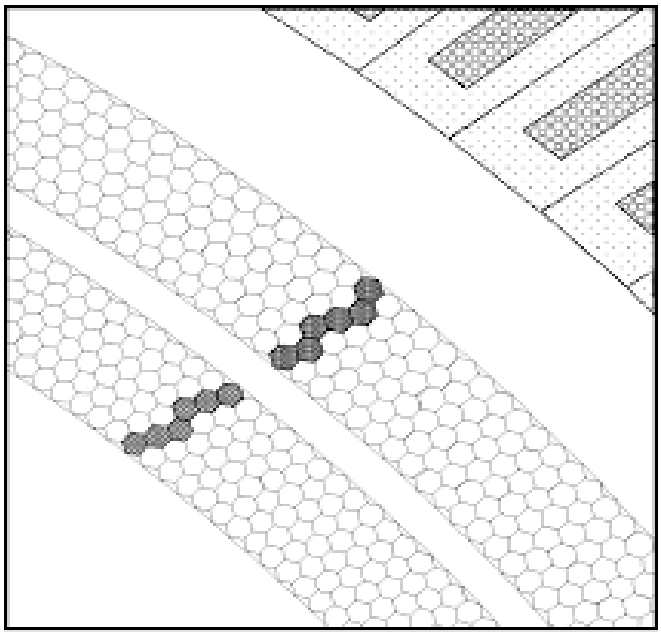

Figure 2.11. The two superlayers of the Region 3 drift chambers. The highlighted cells indicate where a sense wire has fired, one in the center of each of the hexagonal cells of field wires.

Radial locations are reffered to as Regions. For each region of the drift chambers, the wires are grouped into two super-layers, each consisting of six wire layers. The wires within the first super-layer of each region are aligned perpendicular to the magnetic field's bend plane in order to best measure the track curvature. The second super-layer for each region by a 6^0 stereo angle with respect to the first in order to provide azimuthal tracking information.

The six 'Region One' chambers (**R1**) surround the target in an area of low magnetic field. All six inner R1 chambers were assembled into a single self-supporting structure. The six 'Region Two' chambers (**R2**) are situated between the magnet coils in an area of high field near the point of maximum track sagitta. The six 'Region Three' chambers (**R3**) are located outside of the magneti coils (see **Figure 2.8**). Each R3 chamber was installed by attaching it to the outside edges of the cryostats. From considerations of system safety, as well as to improve the operating lifetime, an 88-12% mixture of argon and CO_2 was selected. The probability that a good hit is recorded in a wire layer through which a charged particle has passed-of greater than 98%.

2.3.4 The Cherenkov Counters

The Cherenkov Counter(CC) serves the dual function of triggering on

electrons and separating electrons from pions [**2.3**]. The design of the

Cherenkov detector aims at maximizing the solid-angle coverage in each of the

six sectors out to an angle $\Theta = 45^{o}$. This is achieved by placing the light-

collecting cones and photomultiplier tubes (PMTs) in the regions of shadowed

by torus coils. The light-collection optics was designed to focus the light only in

the azimuthal direction (**Fig.2.12**), which preserves information on the electron polar angle Θ_e. The full Θ range of each of the six sectors was divided into 18

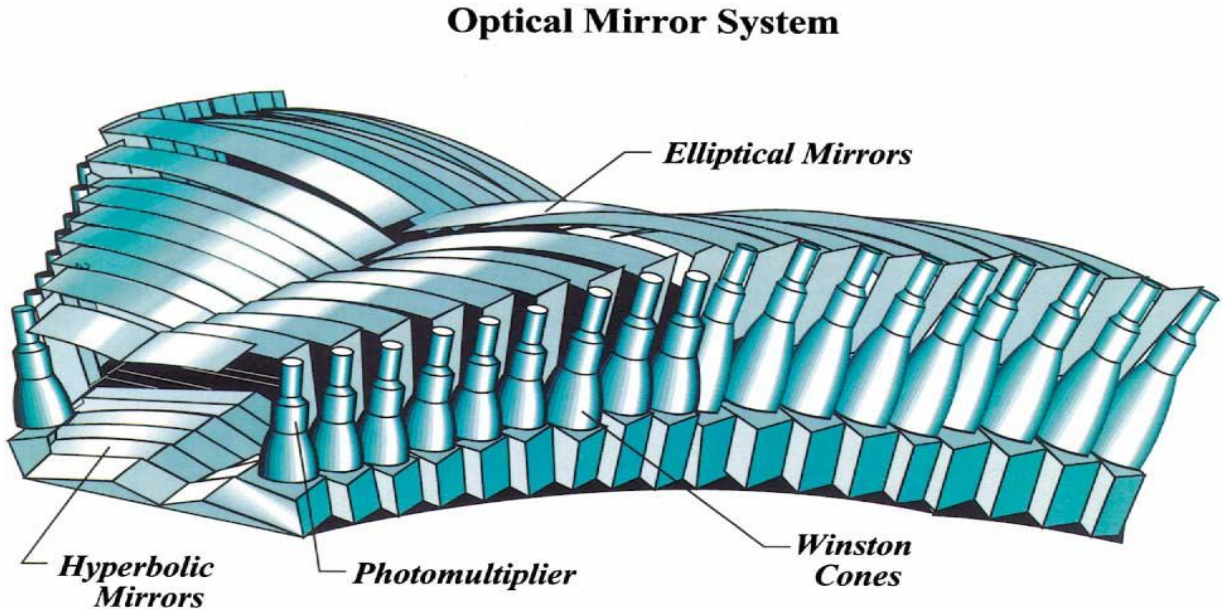

Figure 2.12. A diagram of one the Cherenkov counters **(CC)** spanning a sector in **CLAS**. An electron track and its subsequent radiation is shown in being reflected in to the light cone and detected by the **PMT**. [**2.1**].

regions and each Θ segment was divided into two sub-modules about the

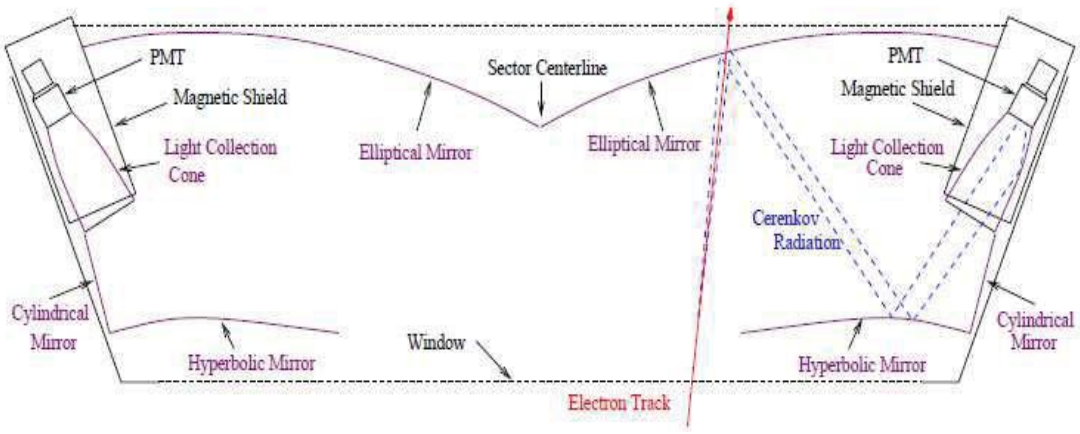

Figure 2.13. A schematic diagram of the array of optical modules in one sector of the six sectors.

symmetry plane bisecting each sector. This results in a total of 12 identical subsectors around the Φ direction for each Θ interval, and a total of 216 light-collection modules.

The Cherenkov Counters as shown in **Figure 2.13**, are located outside Region 3 of the drift chambers. These detectors are generally not operational during tagged photon runs but were operational for the eg3 data set.

2.3.5 Time–Of–Flight counters

The Time of Flight (TOF) [**2.4**] system is designed to measure the flight time of particles produced from beam target interaction. Charged particle identification is an important part of the physics program. If a particle's start position and momentum are known by taking the path length information to where it was detected in TOF, then one can calculate the velocity of that particular particle. In CLAS TOF scintillators are located radially outside the drift chambers and Cherenkov counters, but in front of the calorimeters. The average distance from the scintillators to the center of CLAS is 5m. The TOF scintillators for each sector are divided into 58 scintillator paddles which range from 32-445cm long. Each sector is divided into four panels. The forward panel scintillators are 15cm wide, whereas the three large-angle panels have 22cm wide scintillators. Each scintillator paddle has a PMT(**Fig.2.15**) readout at each end. The view of TOF scintillators and PMTs in both edges are shown in **Fig.2.14** Using the time difference between signals in the two PMTs allows for the determination of the distance from the PMTs to the hit. The large-angle scintillators are connected to bent light guides which are then connected to the PMTs. In order to reduce cost, the paddles of the largest-angle panel are paired into single PMT readouts. The TOF counters generate prompt signals for the CLAS trigger electronics as well as signals for pulse-height and timing

analysis. The trigger depends on a threshold energy deposited in the TOF counters. The typical time resolution of the TOF is 150-200ps.

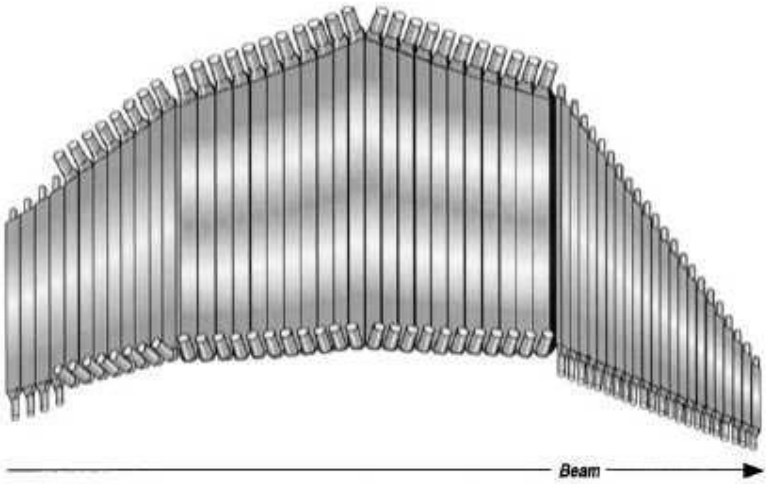

Figure 2.14. Schematic view of one time of flight **(TOF)** wall sector.

The time of flight system of CLAS uses the start to arrival time of a particle to determine its flight time. The system was purposed to include good time resolution to adequately identify particles and also obtain good segmentation to provide flexible triggering and pre-scaling.

The TOF system is equipped for a resolution of σ = 120 ps at the small angles and 250 ps at angles of 90° and larger. These specifications are required by the fact that at small angles, the most energetic particles are produced requiring a better resolution where this lessens with increase of θ angle. Using off-line analysis, the final time resolution for particles is achieved by correcting leading-edge discriminator based time measurements with pulse-height information for the introduced time-walk.

Thus, the system is required to give signals that represent a uniform response to selected particles that reach the time of flight detectors. Each counter has its signal readout by a QDC and a pipeline TDC, and can be used to generate prompt signals for the CLAS level 1 trigger. The TOF system was also used during the analysis to calculate the velocity of particles passing through CLAS by measuring the flight time between the start counter and itself.

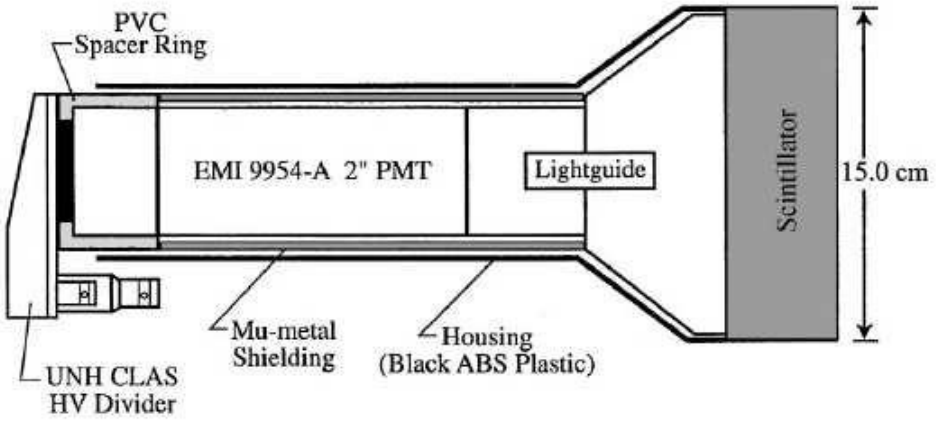

Figure 2.15. Sketch of a Photomultiplier Tube **(PMT)**.

The TOF system is not only used to determine the particles velocity but can also be used for energy-loss measurements. Energy loss in the counter is proportional to pulse-height information, which means there is a separate way to identify slow particles. In addition to excellent timing resolution and segmentation, the TOF system has to be able to operate in a high-rate environment.

2.3.6 Electromagnetic Calorimeter

The Electromagnetic Shower Calorimeters (ECs) [**2.5**] are primarily used to provide the electron trigger for CLAS in electron beam experiments, and for the reconstruction of π^0s, ηs from their decay photons. They can also be used for pion rejection and neutron detection (including neutron/photon discrimination). Each sector in CLAS has a calorimeter that covers scattering angles from 8^0 to 45^0. In two sectors this coverage is extended to 90^0 by the Large Angle Calorimeters (LACs). The EC in each sector was constructed in the shape of an equilateral triangle, in order to match the hexagonal geometry of CLAS. Each calorimeter consists of 13 identical submodules, with each submodule made up of three layers of 2-mm-thick lead plates, interleaved with

layers of 10-mm-thick, 10-cm-wide scintillator strips. The three layers of scintillator strips in a submodule are rotated 120^0 relative to each other, so that each layer is parallel to one side of the triangle. These three layers within each submodule are referred to as the U, V, and W-planes, and they enable stereoscopic readout, which is necessary to resolve multiple-particles in the EC. **Figure 2.16** shows the layout of EC. The layers are arranged in a projective geometry, which means that in the direction away from the target, each layer has a slightly larger area than the previous one. This minimizes shower leakage at the edges of the detector. The active volume of the EC is thus a (truncated) triangular pyramid, having a base of 8 m^2, with a projected apex at the CLAS target 5 m away [**2.5**]. Of the 13 submodules, five constitute the inner portion of the EC nearest to the target, while the other eight make up the outer portion. The inner and outer portions are read out independently, thus providing longitudinal sampling of the showers. The CLAS EC is thus a sampling calorimeter, which serves to provide better particle identification for electrons.

When an electron enters the EC it interacts with the scintillator-lead layers and loses energy by radiating a bremsstrahlung photon. This photon then induces the production of a e^+e^- pair which leads to more bremsstrahlung, thus producing an electormagnetic shower. To reconstruct a valid hit in the EC, the energy deposition is required in all three planes of a module. The energy and time of the hit can then be calculated by measuring the path lengths from the particle hit position to the readout edge.

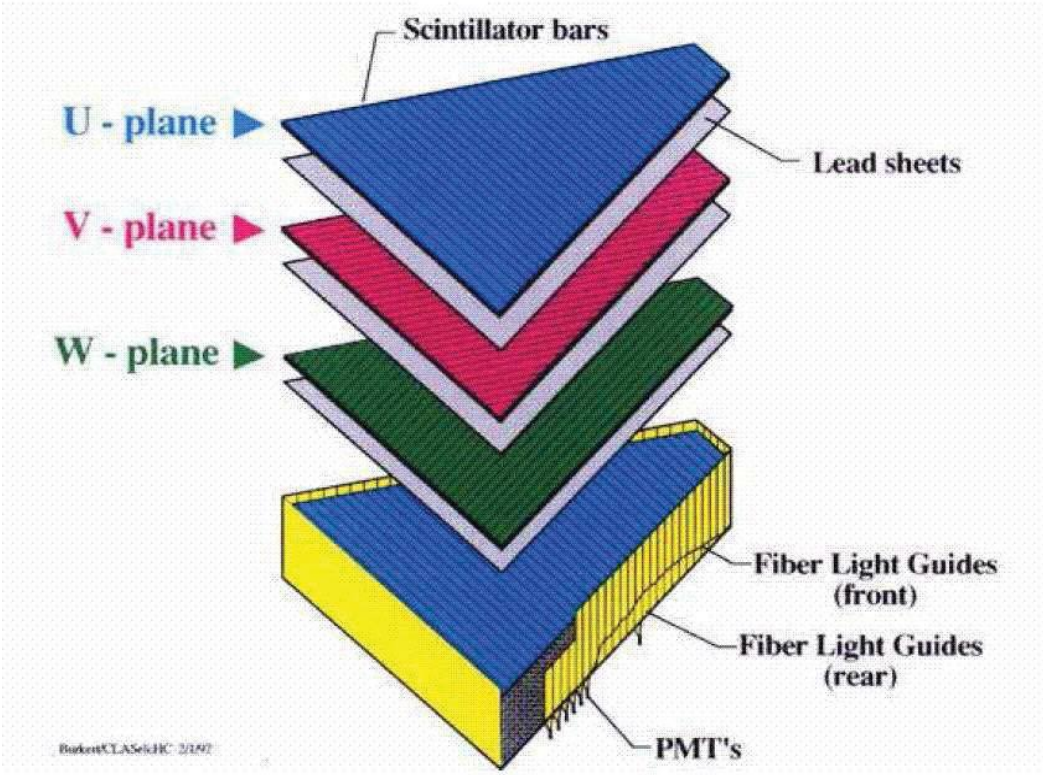

Figure 2.16. Exploded view of one of the six **CLAS** electromagnetic calorimeter **(EC)** modules.

2.3.7 The Start Counter

The purpose of the start counter (ST) is to provide the start signal for an event that occurs in the target. To serve this function, the ST consists of a collection of scintillator paddles that completely surround the target [**2.6**]. The scintillator paddles are constructed in a V-shaped arrangement (**Fig.2.17**). In

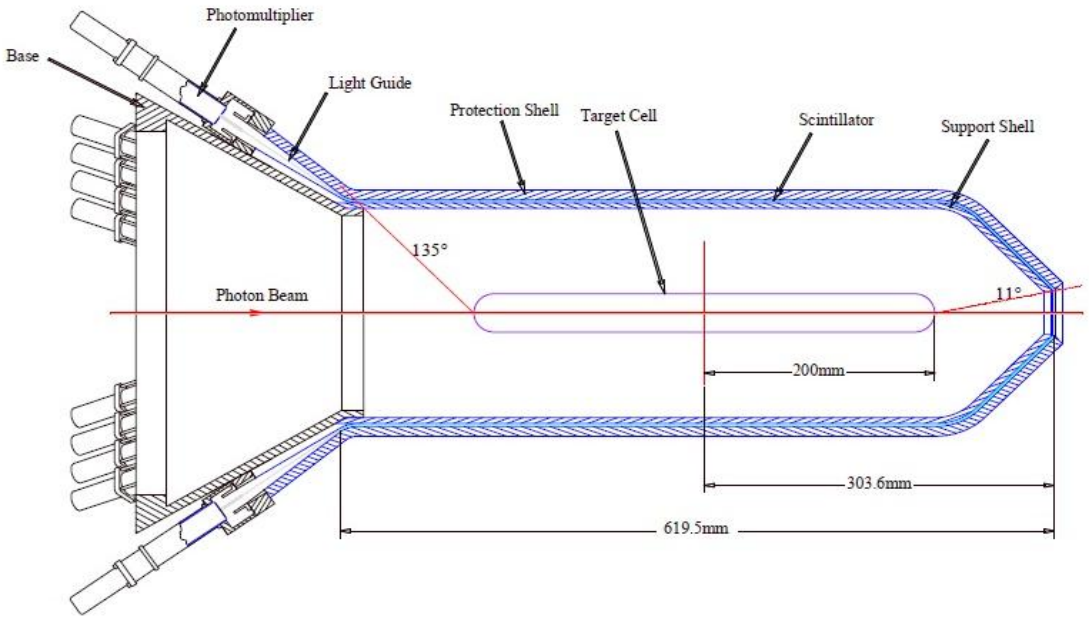

Figure 2.17. The **CLAS** start counter **(ST)** surrounding the target cell.

this way, each paddle provides coverage in CLAS, resulting in a hexagonal tube around the length of the target. The tube tapers to a hexagonally shaped cone at the downstream end of the target, where the paddles are bent inward so as to provide coverage for small angles. This design also enables the PMTs at each end of the scintillator to be situated upstream of the target so as to avoid interfering with the particles originating from the target, as well as to be out of the way of the photon beam which could potentially damage them. The paddles are only 3mm thick to minimize multiple scattering, and each section (covering one sector) is 60 cm long. The signal obtained from the ST is used in conjunction with the signals from the TOF paddles, the photon tagger, to provide the start time for each event.

2.3.8 The Photon Tagger

The Photon Tagger is the main component in photon beam production in Hall B [2.7]. The photon beam is made by directing the electron beam on a foil producing photons by the bremsstrahlung process. When an electron interacts with the radiator, it emits a bremsstrahlung photon, losing energy in the process.The bremsstrahlung recoil electrons are then deflected downwards by a uniform dipole magnetic field onto the Tagger focal plane, where energy and timing information are extracted. Electrons which did not radiate go into a secondary beam dump, while those that did radiate are detected by a scintillator hodoscope.

The bremsstrahlung photons are nearly collinear with the incident electron beam and pass through a hole in the magnet yoke, after which they are collimated, and then impinge on the target which sits in the center of the CLAS.

The photons themselves are not detected, instead they are tagged by matching them with the electrons that produced them. Photons that are produced with between 20% and 95% of the incident electron beam energy (E_0) are tagged in the hodoscope detector [**2.7**].

The tagger magnet's field strength is set such that electrons near energy E_0 will curve and strike a shielded beam dump below Hall B. However, electons that radiate energetic photons have significantly lower energy, thus curving more in the magnetic field to strike the scintillator hodoscope (**Figure.2.18**).

This hodoscope consists of two layers of scintillators and PMTs**.** The E-counters to determine the radiated photon's energy and the T-counters to determine its timing.

The E-counters are used to determine the momentum of the recoiling electrons simply by measuring which path the electron goes, because the path of electrons in the magnetic field is solely determined by the momentum. The E-counters are 384 partially-overlapping scintillators each 20 cm long and 4 mm thick, providing 757 channels for energy measurement [**2.7**]. The widths of these counters vary from 6 to 18 mm such that each spans a constant energy interval of 0.003 E_0. From the overlapping scintillator paddles, the energy of the incident electron beam, and the applied magnetic field, the photon energy can be determined with a resolution of 0.001 E_γ.

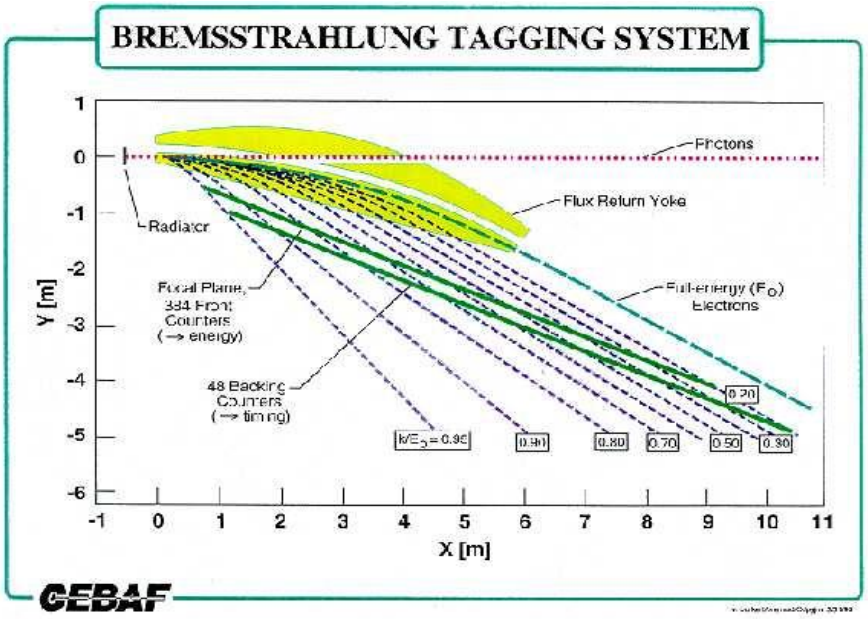

Figure 2.18. The schematic diagram of the tagger system in Hall B. The purple dashed line shows the trajectory of photons generated by bremsstrahlung of the electron beam. The cyan dashed lines are paths followed by recoil electrons. Each path corresponds to a fixed momentum of the recoil electrons.

The T-counters are 61 scintillator paddles, each 2 cm thick, which provide a time resolution of 110 ps. The first 19 paddles correspond to photon energies of 0.75 E_0 and greater, and are much narrower than the others. This allows experiments to run with a high photon beam flux while maintaining adequate electron-photon matching at low photon energies. Within each group, the T-counters vary in width to maintain the same counting rate in each paddle to account for the 1/E energy distribution of the bremsstrahlung photons. For CLAS eg3 run period, a 1.5 μm thick gold foil was used as the

radiator. Corresponding to 3×10^{-4} radiation lengths, this relatively thick radiator was used to provide large photon flux.

The time resolution from the tagger system is good enough to determine from which beam bunch the recoil electron come. In the off-line analysis, the time is corrected according to the beam bunch (RF (**r**adio-**f**requency) correction), which is obtained from the accelerator and the most accurate time information is available in the data. It is also corrected to the time when the photon reaches the target in order to serve as the start time of the event.

2.3.9 Trigger System

To filter out electronic noise and pick only events of interest, a trigger system is necessary. The trigger system for CLAS is essential to decide when a particular event will be written into the data stream to eventually be analyzed. A variety of processes such as electronic noise and cosmic rays passing through a detector element could produce a signal in a subsystem that does not correspond to a physics event. The CLAS trigger is therefore required to determine which set of signals correspond to a real physics process of interest. The CLAS trigger uses logic signals derived from the various detector subsystems to decide on whether to initiate the digitization and readout of ADCs (**A**nalog to **D**igital **C**onverter) and TDCs (**T**ime to **D**igital **C**onverter) or perform a fast clear/reset. Depending on the event rates in the detectors and the system live time the trigger can be configured to be highly specific to a signal state configuration of particles or relatively open ended [**2.1**]. This is implemented by 3 components: level 1 trigger, level 2 trigger and trigger supervisor. In brief, for photon beam experiments the **level 1 trigger** is initiated by the data from the start counter and is configured to make a

decision based on some combination of tagger master OR, TOF and start counter information. It uses a lookup table to identify true charged particle tracks by checking for a match between hits in the TOF and hits in the start counter which correspond to the same sector. The **level 2 trigger** uses tracking information from the drift chambers, looking for suitable particle tracks before declaring an event valid. The system is designed to give fast information on a physics event of interest in conjunction with the level 1 trigger, as well as providing a more stringent constraint on which events are read out. For example, a combination of noise and background events could trigger an event at level 1 but no correlated track would be present in the drift chambers and this would cause level 2 to send a fast clear signal to all TDCs. This event would then not be read into the data stream. The trigger supervisor takes all level 1 and level 2 trigger inputs and produces all common start and stop signals, busy gates and resets required by the detector electronics.

2.3.10 Data Acquisition

The CLAS data acquisition system (DAQ) builds events into a format that can be used for analysis using the CODA system [**2.1**]. The DAQ receives data from the various detector systems that is digitized in VME and FASTBUS crates in the hall before being collected by VME readout controllers. These digitized values are then tabulated in such a way that each event is associated with a unique identity number. These data arrays, or event fragments, are then buffered and sent to an online acquisition computer. At this point the event builder running on one of online computers assembles the fragments and converts them into an event in a BOS format [**2.8**]. The event builder then

passes the completed events on to the event transporter which transfers them to shared memory where they can be used for data monitoring or online analysis. Finally, the event recorder picks up all the events for permanent storage on the RAID array. From here the data can be transported to the JLab tape silo, where it becomes available for off-line analysis.

Chapter 3

CLAS EG3 run period

3.1 Running Condition

The eg3 run period of CLAS took place between December 6th, 2004 and February 1st, 2005 in Hall-B at JLab. For 29 days of production on liquid deuterium target, the eg3 run period collected about 4.2 billion physics events, 32 TB of raw data with an average 2.7 tracks per event. All of the CLAS detector components have to be carefully calibrated for every run period to make sure the recorded electronic signals can be used to determine meaningful physical observables with reasonable resolutions. During this process, the photon flux (gflux) was calculated for each photon energy bin with the effciency of the tagger system already included. For the eg3 run period the CLAS torus magnetic field direction was such that positively charged particles are bent towards the beam line. The field was optimized for forward going negatively charged particles.

3.2 Calibration and Processing

All of the CLAS detector components have to be carefully calibrated for every run period to make sure the recorded electronic signals can be used to derive meaningful physical observables with reasonable resolutions. A database called CALDB is used to store calibration constants for all CLAS runs. In particular, the set of calibration constants and its corresponding run period is linked by a database table run index. This gives the flexibility that one can test different sets of constants for different runs. Once the calibration constants for eg3 run period are in place, the eg3 data were processed with the

standard CLAS offline reconstruction software package "user_ana" [**3.1**]. It translates electronic signals into physical variables like time, position, energy, momentum, direction, etc. and furthermore combines and interprets them as individual particles from physics reaction events.

3.3 Golden Run List

Data taking in Hall B is grouped into runs. Run numbers for CLAS eg3 run period data set are from 45255 to 46351. The first good run starts at 45552 (See **Table 3.1**). The runs before it are mostly cross-check or optimization run or questionable for other reasons. Most good runs are using a beam current of 30 nA and there are four high luminosity runs at 35 nA. The runs from 45552 to 45627 have been performed before Christmas shutdown 2004, and the rest in January 2005. The list of golden runs is given in **Table 3.2**.

Table3.1 CLAS eg3 run period good runs

Run Range	Beam Current (nA)
45548-45556	30
45558-45563	30
45568-45609	30
45612-45614	5
45621-45626	30
45627	30
45804	10
45807-45811	35
45812-45852	30
45859-45937	30
45942-45943	10
45948-45975	30
45976-46113	30

Table 3.2 The Golden Run List

45552	45553	45554	45555	45556	45557	45558	45563	45566	45568
45569	45570	45571	45572	45576	45577	45578	45579	45580	45581
45582	45598	45599	45600	45601	456602	45603	45605	45606	45607
45608	45609	45612	45613	45614	456621	45622	45623	45624	45625
45626	45627	45804	45807	45808	45809	45810	45811	45812	45814
45815	45816	45817	45818	45847	45848	45851	45852	45860	45862
45863	45864	45866	45868	45869	45870	45872	45873	45874	45876
45891	45893	45894	45895	45896	45897	45902	45903	45904	45905
45906	45907	45911	45912	45913	45914	45916	45917	45918	45919
45920	45921	45922	45923	45924	45925	45926	45927	45928	45929
45930	45931	45932	45933	45934	45935	45936	45937	45938	45939
45942	45943	45944	45945	45946	45947	45948	45976	45977	45978
45981	45983	45984	45985	45987	45988	45989	45993	45995	45996
46000	46001	46002	46003	46004	46005	46009	46011	46012	46013
46014	46015	46016	46017	460108	46019	46020	46021	46022	46023
46024	46025	46028	46029	46030	46035	46036	46037	46038	46046
46047	46057	46058	46062	46063	46064	46065	46066	46069	46071
46072	46073	46074	46077	46078	46085	46086	46087	46088	46089
46093	46094	46096	46097	46098	46099	46100	46101	46104	46113

3.4 The Beam

The electrons were accelerated up 5.76 GeV in the CEBAF superconducing LINACs and passed through a radiator with a nominal thickness of 3 x 10^{-4} radiation length. The photon beam from the radiator impinged a 40 cm long and 4 cm diameter liquid deuterium target positioned 50 cm upstream of the nominal CLAS center (see **Figure 2.19**).

The characteristic half-angle, Θ_C, of the beam at 5.7 GeV is 8.7 x 10^{-5} rad, which projected to the target 22 m away is 2 mm [**3.2**]. The collimation system is designed to limit the beam to a diameter of 33 mm at the CLAS target [**2.7**]. Using the 8.61 mm diameter collimator, beam diameter was collimated aperture of 33 mm at the nominal location of the CLAS target.

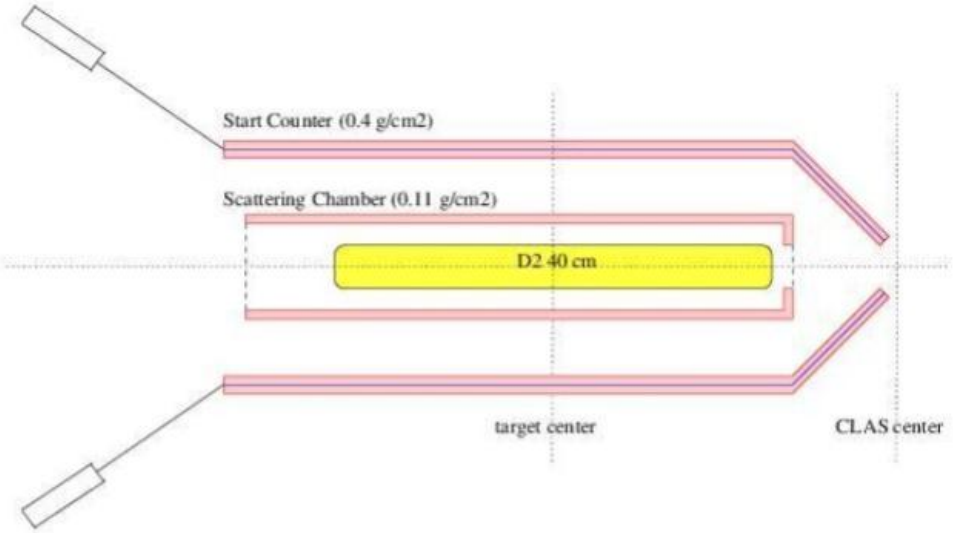

Figure 2.19. Schematic view of the target, foam scattering chamber [**3.2**].

For most of the running time, the electron beam current was chosen to be 30 nA, which was limited by the drift chamber performance. The CLAS

tagging system tags bremsstrahlung photon with energies ranging from 25% to 95% of the incoming electron energy, which is about 1.15-5.50 GeV for CLAS eg3 run period. Only energies above 4.5 GeV were included in the trigger.

3.5 The Target

For the experiment a liquid deuterium target was chosen. The target has a 4 cm diameter, providing sufficient coverage of the beam. The target length was chosen to be 40 cm with the upstream end located at the beginning of the start counter, allowing for a large event rate while maintaning an acceptable tagger rate.

Figure 2.20. Conical liquid deuterium target used for the eg3 run period, measuring 40 cm in length, and the 4cm in diameter at its widest. The beam axis runs along the center of the target. The entrance and exit windows of the target cell were made with thin aluminum.

Figure 2.20 illustrates the liquid deuterium target used during eg3 run period. It has a slightly conical shape and a rounded endcap with a thin aluminum window at the front. This window allows the remnants of the photon

beam to exit the target with minimal interactions.

Chapter 4

4.1 Data Analysis

The three coherent photoproduction reactions on deuterium in fully exclusive final states that have been analyzed are:

$$\begin{gathered} \gamma d \rightarrow \pi^+\pi^- d' \\ \gamma d \rightarrow K^+K^- d' \\ \gamma d \rightarrow p\bar{p}d' \end{gathered} \tag{4.1}$$

The analysis cover photon energy range $E_\gamma > 4.5$ GeV. This is the region of the Hall-B photon tagger that was in the trigger during the eg3 run period.

The analysis has been performed in multiple steps. First, events were selected based on the topology, one negatively and two positively changed tracks, and no neutrals. Then, three momentum conservation has been used to select exclusive events that have final state transverse momentum ≈ 0 within the detector resolution. After that, the photon was selected from detected hits in the tagger hodoscope. The z-component of the final three momentum and the photon energy measured in the tagger spectrometer, should be equal within the resolution. After selection of the photon and refining the event start time (calculated using tagged photon time) particle identification was performed using the time-of-flight method as well as energy deposition in scintillator counters (for deuterons only). The final selection of events in each final state, $\pi^+\pi^- d$, $K^+K^- d$, and $p\bar{p}d$ was done using the energy difference between the initial and final states [**4.2**].

Results of the analysis include study of the invariant mass and t-distributions of rates in $p\bar{p}$ as well as $\pi^+\pi^-$ and K^+K^- final states, and angular

distribution of p (or $\bar{p}$) (and similarly for other coherent production channels) in the decay CM (**C**enter of **M**ass) frame.

The end results is the extraction of photoproduction cross section for these reactions.

4.2 Event Selection, fully exclusive final state

The final state of interest contains three charged particles, two positively and one negatively charged, and nothing else. The first pass of analysis selects events with that topology. One of kinematic constraint of a fully exclusive final is the 3-momentum conservation:

$$\sum p^{i}_{x(y)} = 0 \text{ and } \sum p^{i}_{z} = E_{\gamma},$$

that uses only tracks momenta and do not need particle identification to be done. Since the incoming photon and the target deuteron do not have transverse momentum component, and the target deuteron is in rest, for an exclusive final state these relations should hold within the measurement uncertainties. Above, i is the final state track number, p is the track momentum and the E_{γ} is the incoming photon energy. These constraint will be used to select events before proceeding to PID. Three momentum conservation also will be used to select correct tagged photon and calculate proper start time for CLAS event.

4.2.1 Three-momentum conservation and tagged photon selection

In **Figure 4.1**, distribution of $\sum p^{i}_{y}$ vs. $\sum p^{i}_{x}$ is shown for events with three charged particles in final state: two of them are positive and one is negative.

No neutrals have been detected in these events. A sharp peak at $\sum p_x^i \approx 0$ and $\sum p_y^i \approx 0$ corresponds to events in fully exclusive reactions.

Due to momentum reconstruction uncertainties there may be a dependance of the width and the mean of $\sum p_y^i$ and $\sum p_x^i$ on the total energy of the final system. A p_z dependent cuts on $\sum p_x^i$ and $\sum p_y^i$ have been developed to select exclusive events. The $\sum p_x^i \left(\sum p_y^i\right)$ distributions in small bins of $\sum p_z^i$ has been fitted with sum of Gaussian and a second order polynomial function, see **Figure 4.2**. The mean and the standard deviation (σ) of Gaussian functions have been parametrized as a function of $\sum p_z^i$. As shown in **Figure 4.3**, the mean and standard deviations for both x and y components are almost independent on the Z-component of the total final state momentum. A linear parametrization has been used for $\sum p_z^i$ dependence of means and standard deviation of the Gaussian function:

$$\begin{aligned} &\text{Mean} \sum p_x^i, \sum p_y^i \left(\sum p_z^i\right) = p_0 + p_1 \times \sum p_z^i \\ &\sigma \quad \sum p_x^i, \sum p_y^i \left(\sum p_z^i\right) = p_0 + p_1 \times \sum p_z^i \end{aligned} \tag{4.2}$$

The parameters of these parametrization are shown in **Table 4.1.** For the next step, events have been selected using $\text{mean} \pm 3\sigma$ cut on $\sum p_x^i$ and $\sum p_y^i$.

After selecting events using cuts on transverse components of the final momenta, selection of the tagged photon from multiple hits in the tagger hodoscope has been performed. Due to accidental coincidences between tagger spectrometer and the CLAS, multiple photons will be detected in the event within the trigger time window. The average number of photons depends

on the luminosity. During the data processing, using initial timing information from CLAS event one of photons in the tagger is selected as a photon that interacted with the target and produced the event in CLAS. Then using time measured in the tagger CLAS event start time is defined. That start time is used for particle identification using time-of-flight method. For fully exclusive final state one can ignore time coincidence between CLAS and tagger and use kinematics to find the right photon in the tagger, in particular, use the z-component of momenta. This is especially important for very low rate reactions where out time high rate events can compromise timing of the CLAS event and hanse effect on the correct selection of the tagged photon.

Gaussian param.	Momentum comp.	p_0	p_1

Mean	$\sum p_x^i$	-0.6727×10^{-3}	0.451×10^{-3}
Me			

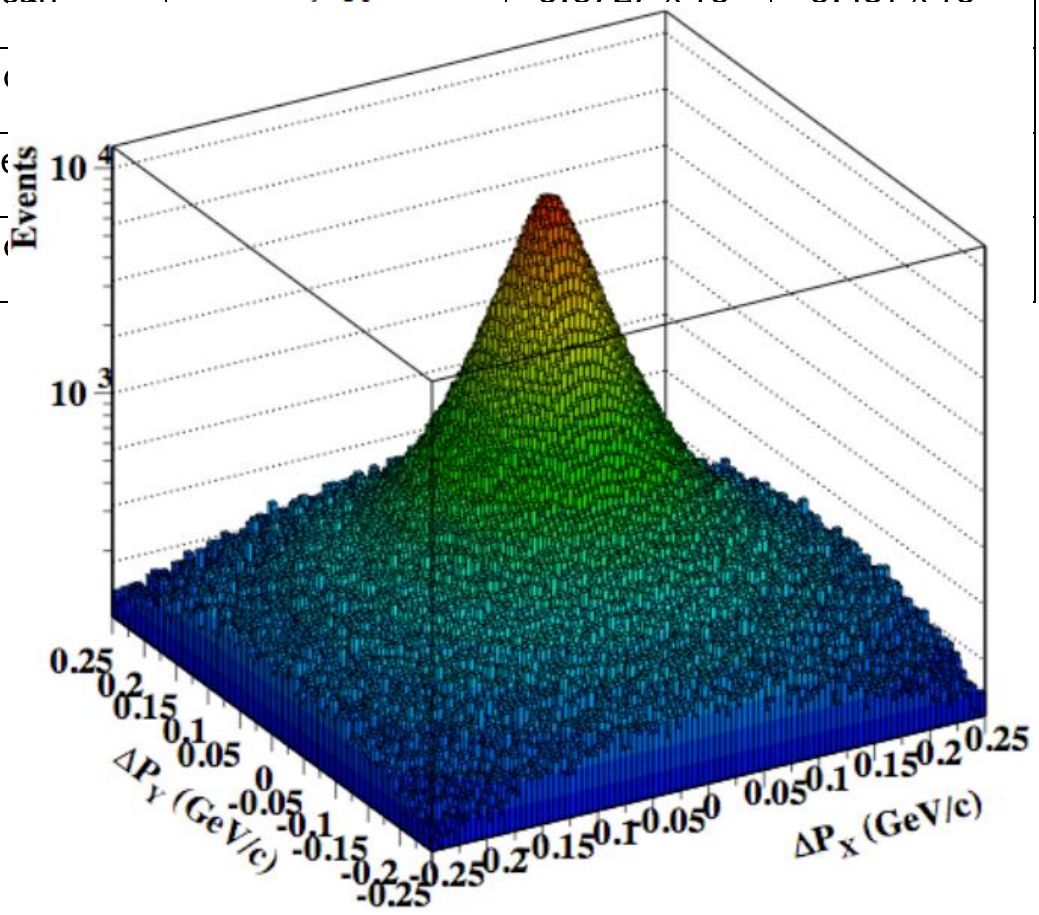

Figure 4.1. Transverse momentum distribution of 3-prong events.

Table 4.1. Parametrization of the mean and standart deviations of Gaussian fit parameters to $\sum \mathbf{p_y^i}$ and $\sum \mathbf{p_x^i}$ distributions.

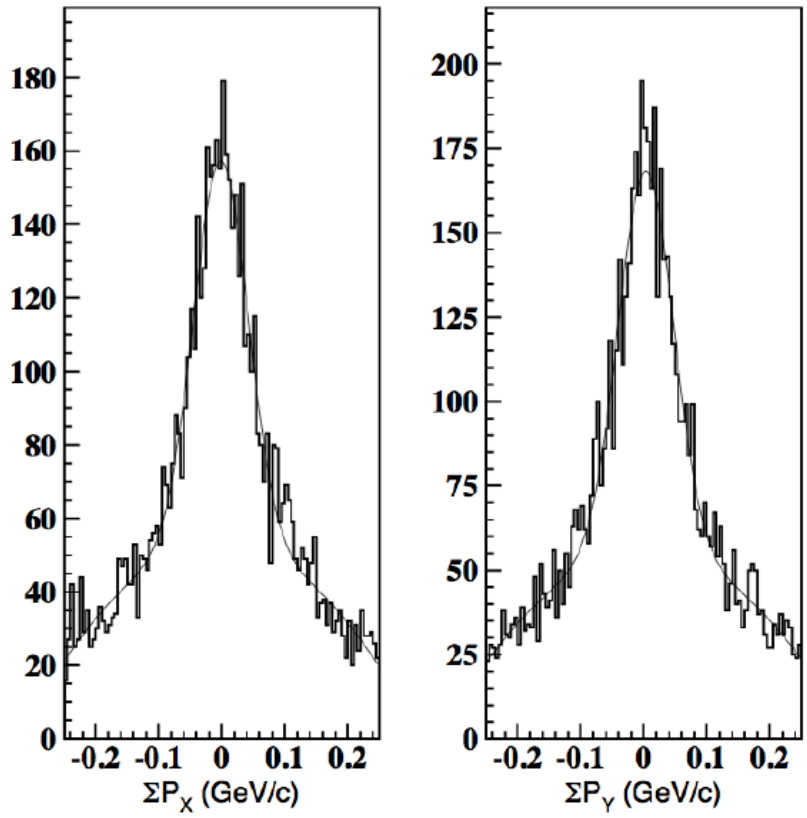

Figure 4.2. Example of fits to $\sum \mathbf{p_y^i}$ and $\sum \mathbf{p_x^i}$ distributions with sum of Gaussian and second order polynomial function in small bins of $\sum \mathbf{p_z^i}$

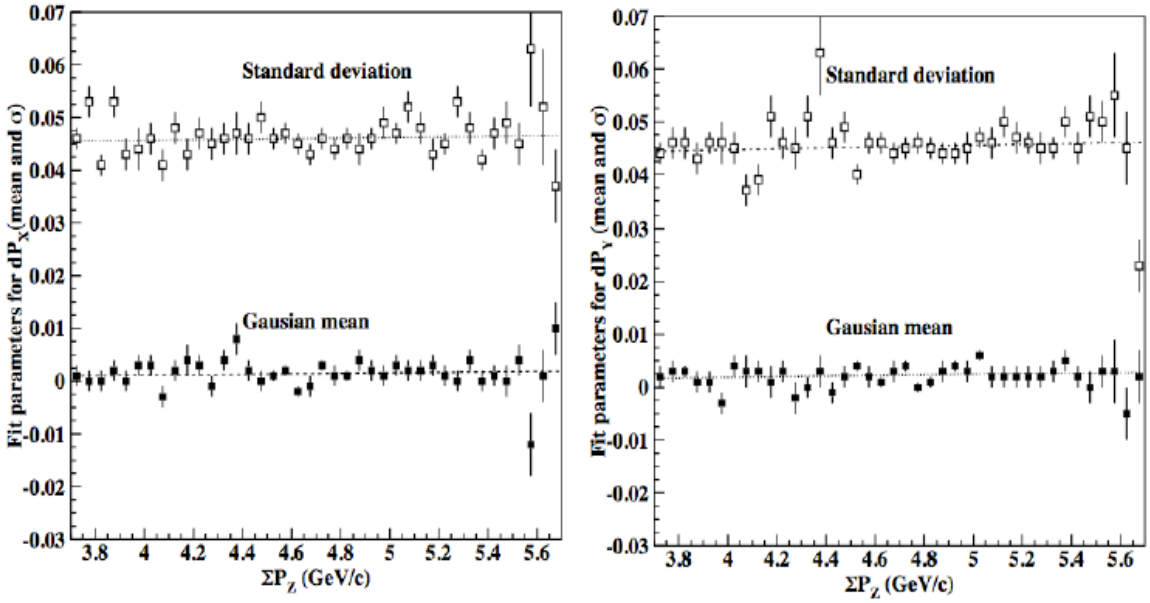

Figure 4.3. Parametrization of means and standart deviation of Gaussian fit function to $\sum \mathbf{p_x^i}$ and $\sum \mathbf{p_y^i}$.

Since the final state is fully exclusive, the z-component of final state 3-momentum vector ($\sum p_z^i$) should be equal to the incoming photon energy (E_γ):

$$E_\gamma \approx \sum P_z^i \tag{4.3}$$

In **Figure 4.4**, dependence of $dP_z = \sum P_z^i - E_\gamma$ on E_γ is shown for events that pass transverse momentum cuts. Again, clear peak near ~0 is seen, indicating exclusivity of final state. As in the case of transverse momentum components, z-momentum difference has been fitted with sum of Gaussian and 2nd order polynomial function in small bins of E_γ ($E_\gamma = 0.05\ GeV$). The mean and standard deviation of Gaussian fits are shown on the bottom graph of the figure. The energy dependance of standard deviations was parametrized with a linear function. The parameters of the linear fit are shown in **Table 4.2**. The energy dependance of the means was ignored since in the energy region of interest, $E_\gamma > 4.5\ GeV$ variations of means is $< 0.01\ GeV$ (or $< 0.2\%$). The $\pm 3\sigma$ cut has been applied to dP_z to select exclusive 3-prong events with matched photons.

There are two reasons that we need to know the photon causing an event. First, the energy of the event photon is needed to guarantee the exclusivity of a reaction. Second, we need to know the time of the event photon, which is used as the event start time to identify the final state particle.

Table 4.2. Linear function parameters for parametrization of standart deviation of $\sum p_y^i - E_\gamma$ distributions as function of E_γ.

Gaussian parameters	p_0	p_1

σ	0.2713×10^{-1}	0.5859×10^{-2}

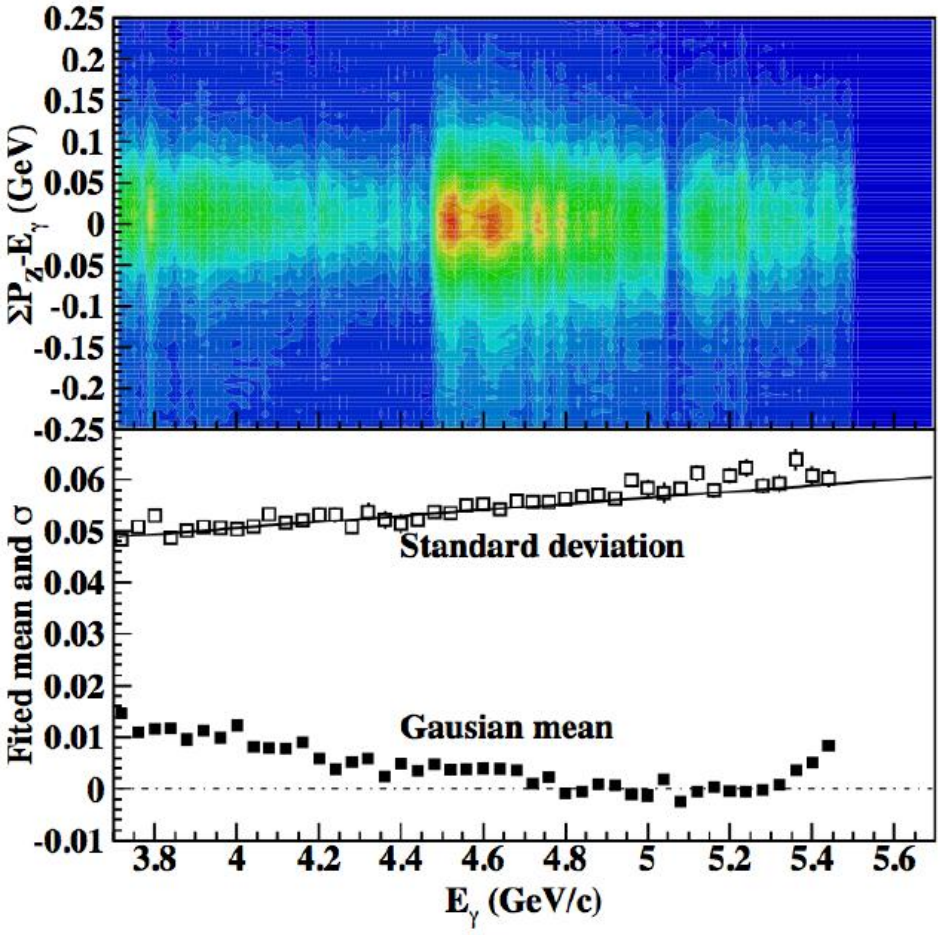

Figure 4.4. Distribution of $dP_z = \sum_{i=1}^{3} P_z^i - E_\gamma$ vs. $\mathbf{E_\gamma}$ for events selected after $\pm 3\sigma$ cuts on $\sum \mathbf{p_x^i}$ and $\sum \mathbf{p_y^i}$ (top graph). Gaussian fit parameters (bottom graph). The solid line is a fit to standard deviation as a function of energy with linear

The number of matched photons with CLAS event after the cut on dPz is shown in the left panel of **Figure 4.5**. As can be seen, number of events with more than 2 matched photons is $< 0.5\%$ of the total number of 1 and 2 matched photon events and therefore they have been discarded. Events with 2 matched photons are about 10% of 1 matched photon events. However, if we

take a closer look, it turns out that the number of useful events with 2 matched photons is also negligible. This is illustrated on the right panel of **Figure 4.5**.

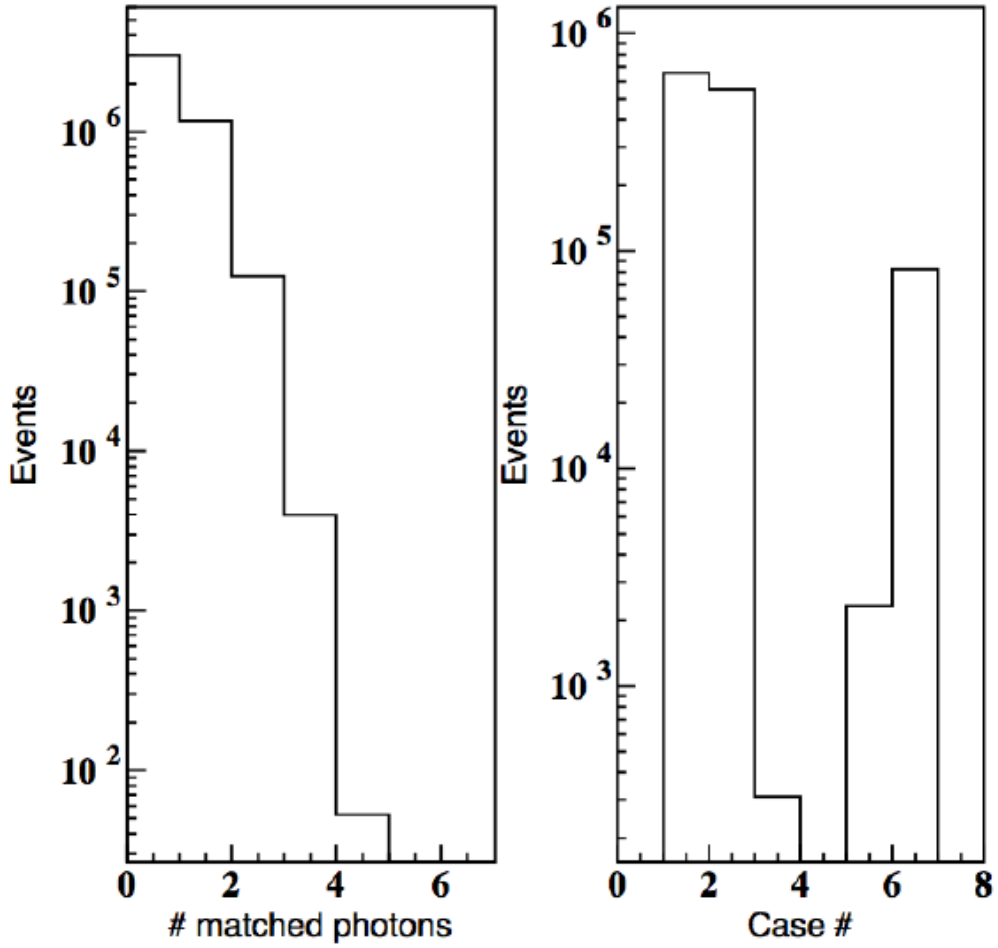

Figure 4.5. Left panel: number of tagged photons satisfying $\pm 3\sigma$ cut on istribution $\sum \mathbf{P}_z^i - \mathbf{E}_\gamma$. Right panel: number of events for different cases of 1 and 2 matched tagged photons (see Case description in the text).

In the plot, the case numbers on x-axis correspond to the following:

- **Case 1** – one matched photon and that photon is the one that was selected during the data processing,

- **Case 2** – one matched photon but the photon is different from the one that was selected during the data processing,
- **Case 3** – two matched photons and only one has energy above 4.5 GeV,
- **Case 5** – two matched photons and both photons have energy above 4.5 GeV,
- **Case 6** – two matched photons but both photons have energy less than 4.5 GeV.

As it can be clearly seen, number of useful cases when there are two matched photons, #3 and #5, are less than 0.3% of 1 photon cases. Further analysis will ignore 2 matched photon cases as well, and only events with 1 matched photon after 3-momentum conservation cuts will be used.

The next step of event selection includes timing analysis of the CLAS event. As was stated above, there are two cases, almost equal number of events, when one matched photon is found. In the Case #1 this photon is the same one that was used for event start time calculation during the data processing and therefore nothing needs to be corrected for timing analysis. In the Case #2 found photon is different and event start time must be correct by the time difference of beam buckets of the new (t^{n}_{tagg}) and previously (during the data processing) used photon (t^{p}_{tagg}). This time difference $t^{n}_{tagg} - t^{p}_{tagg}$ is shown in **Figure 4.6**. The new event start time t^{new}_{st} was corrected as:

$$t^{new}_{st} = t^{old}_{st} + (t^{n}_{tagg} - t^{p}_{tagg}) \quad (4.4)$$

Where t^{old}_{st} is the event start time determined during the data processing.

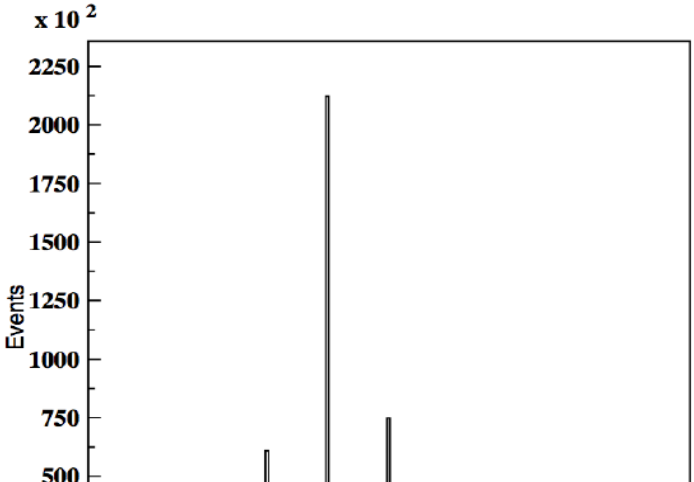

4.2.2 Particle identification

After recalculating the event start time using matched photon, time-of-flight and the speed (β) for each track was defined using the measured time in scintillator counters (CLAS TOF counters), t_{SC}, and the path length from the production vertex to TOF counter, R_{SC}, measured by the DC tracking:

$$\beta = \frac{R_{SC}}{t.o.f} \tag{4.5}$$

$$t.o.f. = t_{SC} - t_{st}^{new} \tag{4.6}$$

Then the mass squared have been calculated for each track using the momentum p, and the velocity, β:

$$m^2 = \frac{p^2}{\beta^2/(1-\beta^2)} \tag{4.7}$$

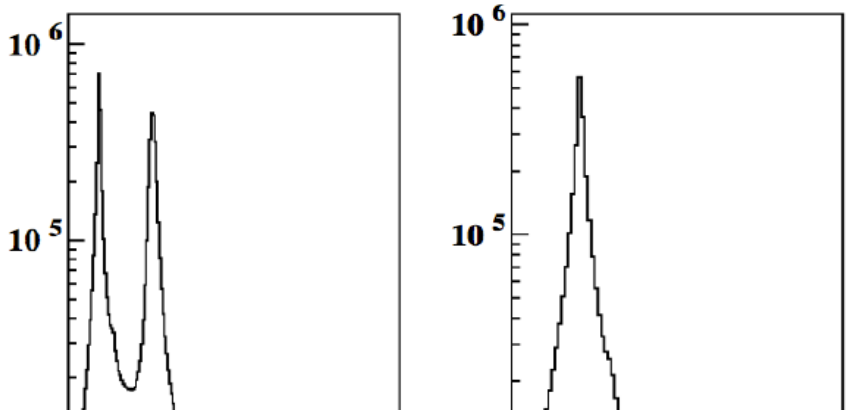

In **Figure 4.7** mass squared distribution for positively (left panel) and negatively (right panel) charged tracks are shown. A loose cuts were used in the first step of particle identification. The cuts on m^2 were not inclusive, meaning that there were overlapping regions of mass squared for different particle spices. A track could have multiple identity that was cleared in the later stages of analysis. In **Table 4.3**, cuts used for $\pi's$, $K's$, protons, and deuteron is listed.

Particle type	Mass squared cut
π^+/π^-	$m^2 < 0.15\ GeV^2$

Table 4.3. Cuts used on mass squared for initial PID.	
$p\bar{p}$	$0.5 < m^2 < 1.5\ GeV^2$
d	$m^2 > 2.75\ GeV^2$

4.2.3 Deuteron ID

In addition to the mass cut, for identification of deuteron candidates cut on the energy deposition in scintillator counters were applied. It was required that the energy deposited in the scintillator counter to be above lines shown in **Figure 4.8**. The lines are defined as:

$$229 \cdot p - 100 \text{ for } p < 0.6\ GeV/c \tag{4.8}$$

$$3 \cdot p + 25/p^2 \text{ for } p \geq 0.6\ GeV/c \tag{4.9}$$

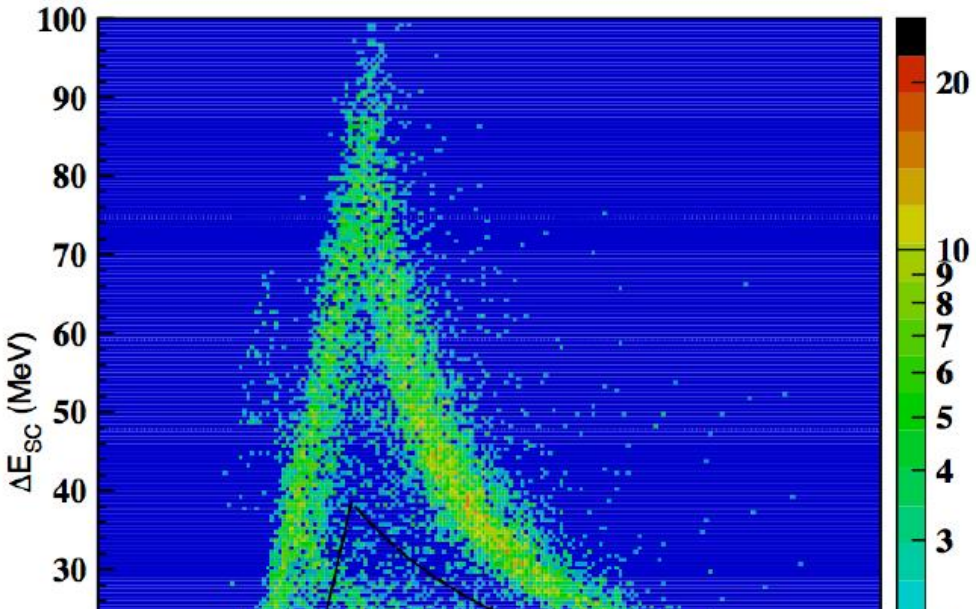

Further refinement of deuteron ID was done using cuts on vertex time calculated using the time-of-flight from the production vertex to the scintillator counter (SC) and the event start time:

$$t_v = t_{SC} - t_{st} - \frac{R_{SC}}{\beta' c} \tag{4.10}$$

where t_{SC} and R_{SC} are the time measured by SC and the distance from the production vertex to SC, respectively. The t_{st} is the event start time determined by the tagged photon (corrected for production vertex), c is the speed of light and the $\beta = p/\sqrt{p^2 + m_d^2}$, where p is the track momentum and the $m_d = 1.8756\ \mathrm{GeV}/c^2$ is the deuteron mass. The vertex time distribution of deuteron candidates as a function of momentum is shown on left panel of **Figure 4.9**.

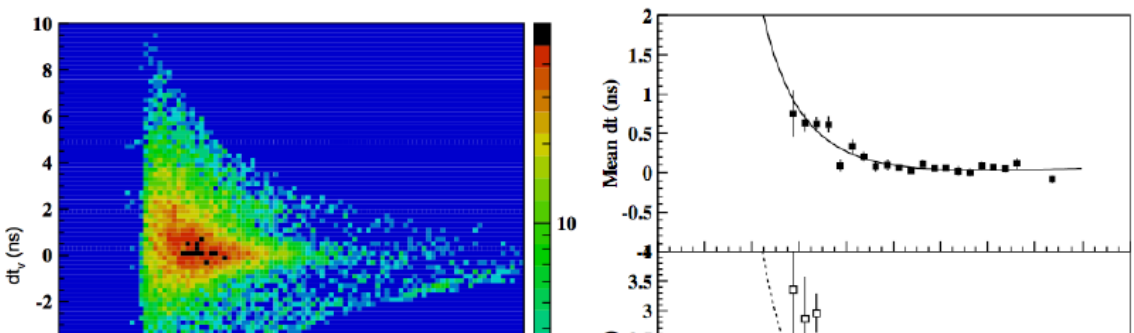

In order to select final sample of deuterons, this distribution has been sliced in small bins of momenta and each slice was fitted with sum of Gaussian and polynomial functions. Then the mean and standard deviation of the Gaussian fits have been parametrized as function momentum. The parametrization function has the form:

$$\mathrm{Mean}(\sigma) = f_0 + \frac{f_1}{p} + \frac{f_2}{p^2} \tag{4.11}$$

where f_i are the fit parameters, and are shown in **Table 4.4**, and p is the deuteron momentum. For the next step of analysis deuterons have been selected using $\pm 3\sigma$ cut on t_v.

In **Figure 4.10** energy loss in scintillator counter by deuteron candidates after t_v cut is shown, demonstrating a clean identification of deuterons. Distributions for each of CLAS sectors are shown in Appendix.

Table 4.4. Parameters of momentum depend parameterization of the mean and the standard deviation of Gaussian fits to the t_v distribution of deuteron candidates.

Gaussian parameters	f_0	f_1	f_2
Mean	0.4828	-1.2516	0.8669
σ	0.9618	-1.901	1.4498

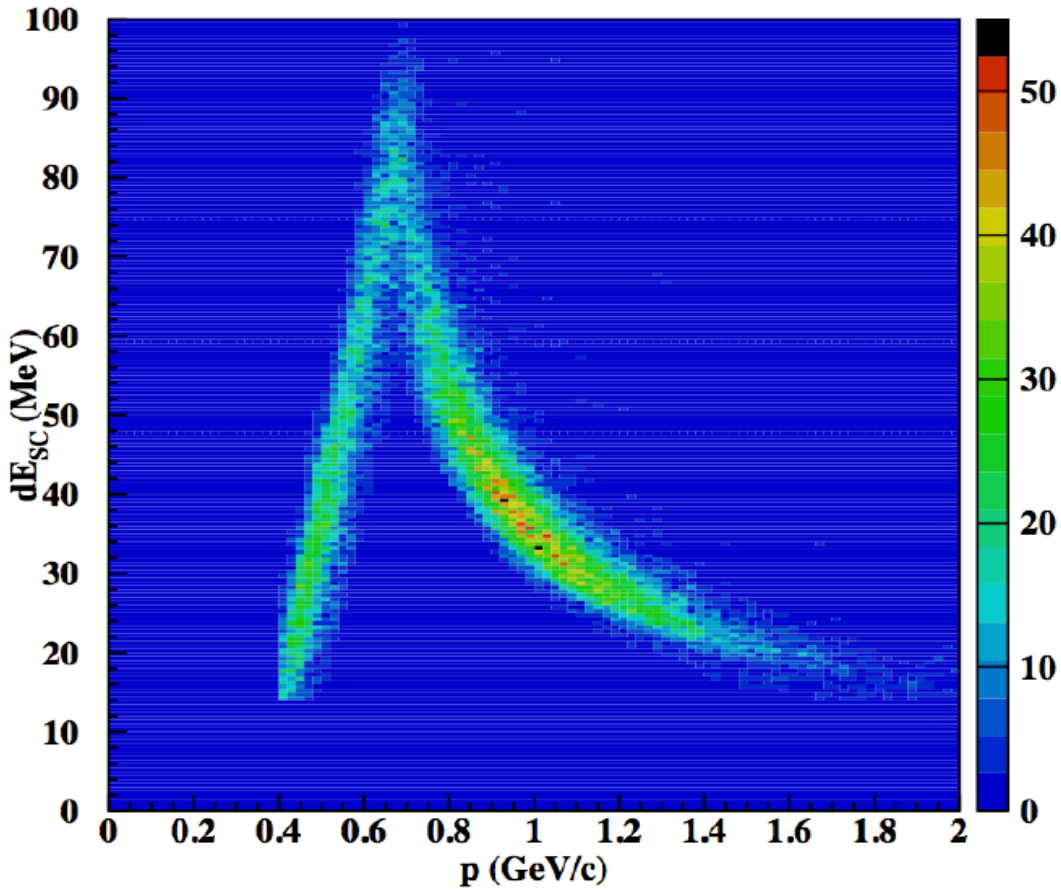

Figure 4.10. Energy loss in SC paddles by deuteron candidates as a function of track momentum after $\pm 3\sigma$ cut on vertex time.

4.2.4 Deuteron momenta corrections

For deuteron candidates momentum corrections have been applied in order to correct for energy loss and for momentum reconstruction imperfections. In **Figure 4.11** difference of deuteron's measured momentum and the missing momentum in the reaction $\gamma d \to \pi^+\pi^- d$ are plotted as a function of measured momentum before (top) and after (bottom) momentum correction. As can be seen after momentum corrections the difference is lined up around zero and no momentum dependance is seen.

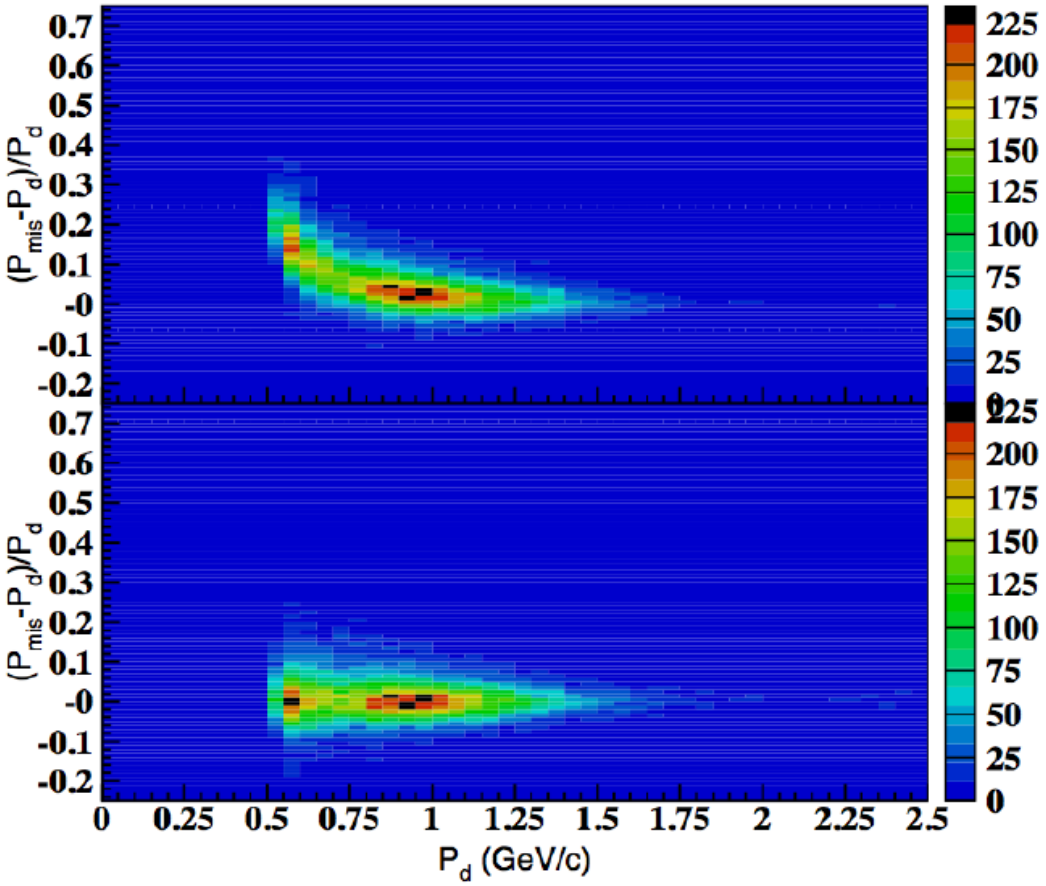

Figure 4.11. Relative difference of missing momentum of $\pi^+\pi^-$ and reconstructed deuteron momentum in the reaction $\gamma d \to \pi^+\pi^- d$ before (top) and after (bottom) momentum correction.

4.3 Final state identification

The key quantity for the final state identification, for selection of events in the three coherent production reactions presented in **Equation 4.1**, is the initial and final energy balance. The energy relation that will be analyzed is based on **Equation 4.3** $(E_\gamma \approx \sum P_z^i)$. If the final state particles are identified correctly (masses defined correctly) then:

$$\Delta E = \sum_{i=1}^{3} p_z^i + m_d - \sum_{i=1}^{3} E_i \qquad (4.12)$$

Here $E_{i=}\sqrt{p_i^2 + m_i^2}$ where p_i is the momentum of i^{th} particle and m_i is its PDG (**P**article **D**ata **G**roup) mass. One should note that due to relatively large p_z, most of uncertainties in this difference arising from momentum measurement will cancel out in the correlation of p and p_z and the resolution in ΔE is much better than if E_γ is used instead of $\sum p_z^i$. The event sample, after cuts on the three-momentum and selection of the tagged photon with $E_\gamma \geq 4.5\ GeV$, was divided into two groups: events with and without identified deuteron candidate. The events that does not have deuteron candidate identified are dominantly from the final state $pp\pi^-$. In top graph of **Figure 4.12** the ΔE vs. $dt_v = t_v^1 - t_v^2$ is shown for all events where the ΔE, is calculated assuming $pp\pi^-$ final state.

Here t_v^i is the vertex time of positively charged tracks assuming they are protons calculated as in **Equation 4.10**.

Events concentrated around the zero in both variables are from reaction $\gamma d \to pp\pi^-$. The same distribution for events with identified deuteron shown in the bottom graph of the figure. No events are present around zero, clearly showing quality of deuteron identification. Events at the upper right corner are from $\pi^+\pi^- d$ final state.

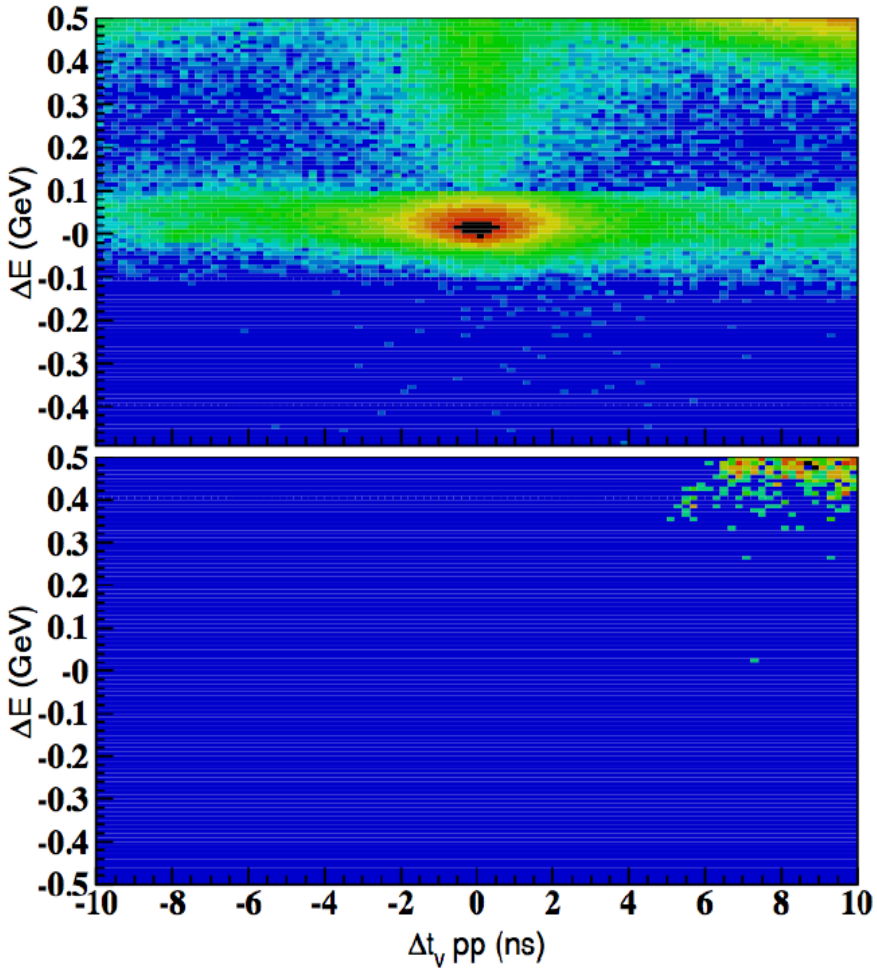

Figure 4.12. The ΔE vs. $dt_v = t_v^1 - t_v^2$ for events without deuteron is the event (top) and with deuteron identified using cuts described (bottom).

To separate events in the three coherent production reactions, **Equation 4.1**, in addition to ΔE analysis, vertex time of kaons and protons were studied as well. Also, a cut was applied to the z-vertex of negatively charged track, $-75\ \mathrm{cm} < z_v < -30\ \mathrm{cm}$, to eliminate events outside of the target region. The z-vertex correlation between positively and negatively charged tracks have been examined as well, see **Figure 4.13**, and expected correlation between tracks produced in the same interaction has been observed. No cuts have been made on the z-vertex difference.

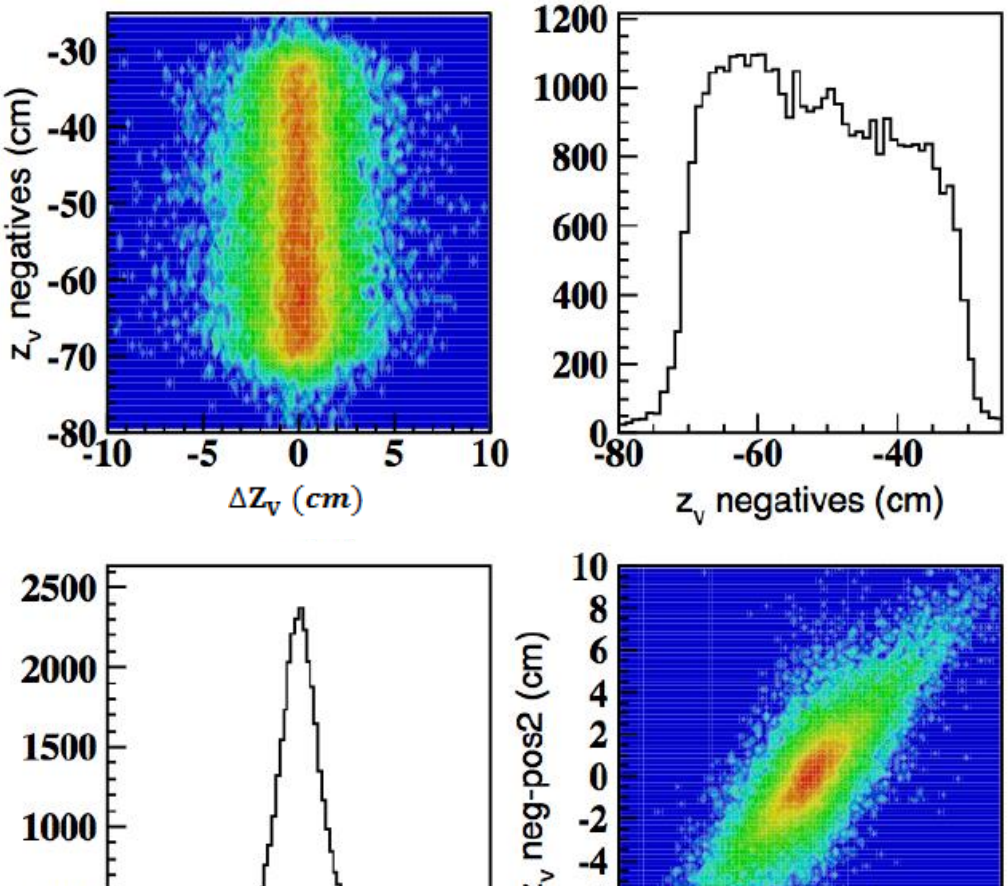

4.3.1 Final state $\pi^+\pi^-d$

Events with a deuteron and two oppositely charged tracks with TOF mass squared $< 0.15\ \mathrm{GeV}$ were identified as events from the reaction $\gamma d \to \pi^+\pi^- d$. In **Figure 4.14**, the distribution ΔE of these events is shown. The tail of the distribution on the left side is due to non-Gaussian effects in the momentum resolution. While longer and larger tail on the right is mostly from non $\pi^+\pi^- d$ events, which got into the pion sample due to a loose mass squared cuts for PID.

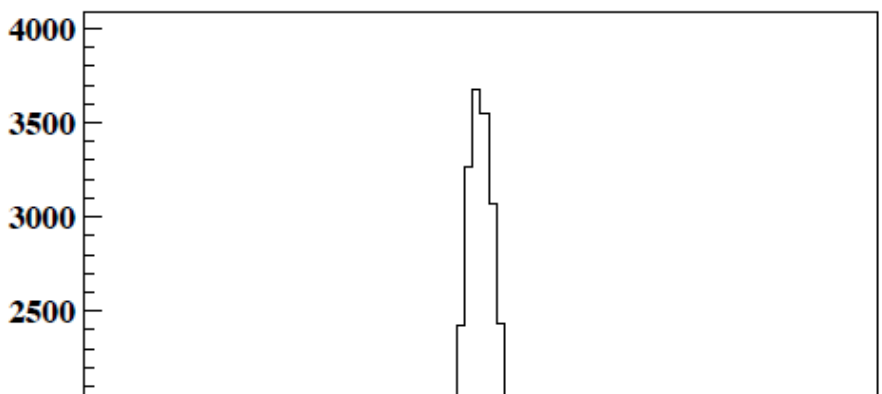

In **Figure 4.15** the ΔE distribution of the same events are plotted assuming the two oppositely charged hadrons are kaons, K^+K^-, (left) or protons, $p\bar{p}$, (right). The kaon pair production events are clearly seen, peak at zero. No peak is seen for proton anti-proton kinematics. The mass squared cut for pions overlaps with the tail of the kaon mass squared distribution and therefore there are kaon pairs in the pion sample. As mentioned above the mass squared cuts are (not inclusive)/exclusive, so the same kaon events will be accounted in the kaon sample as well. One important note is that the ΔE distributions are well separated for three reactions in **Equation 4.1**.

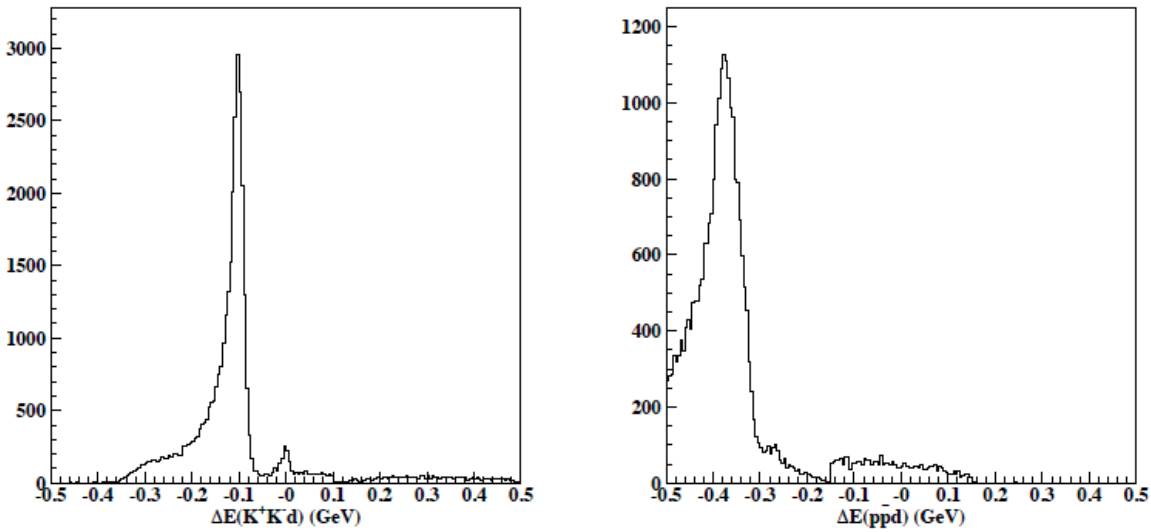

Figure 4.15. The ΔE distribution for $\pi^+\pi^-d$ events calculated assuming they are K^+K^-d (left) or $p\bar{p}d$ (right).

The final sample of pion events was selected with the cut $|\Delta E| < 0.02$ GeV. The scattering angle vs. momentum for all three particles in the final $\pi^+\pi^-$d events are shown in **Figure 4.16**. A large number of events with lower energy deuterons corresponds to region of small $\pi^+\pi^-$ invariant mass, mostly coherent ρ events, see **Figure 4.17**.

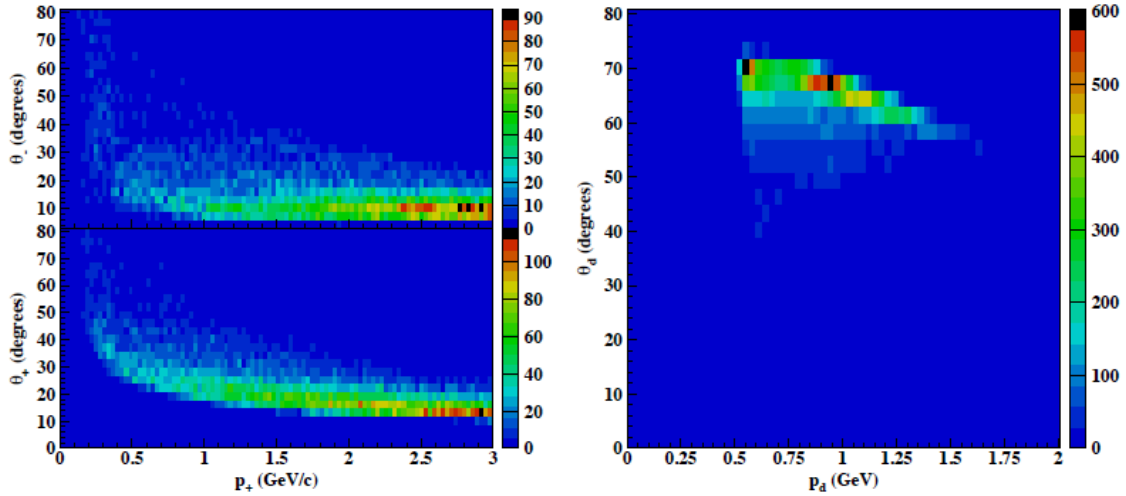

Figure 4.16. The scattering angle, θ, vs momentum for pions (left) and deuteron (right) for final $\pi^+\pi^-d$ events.

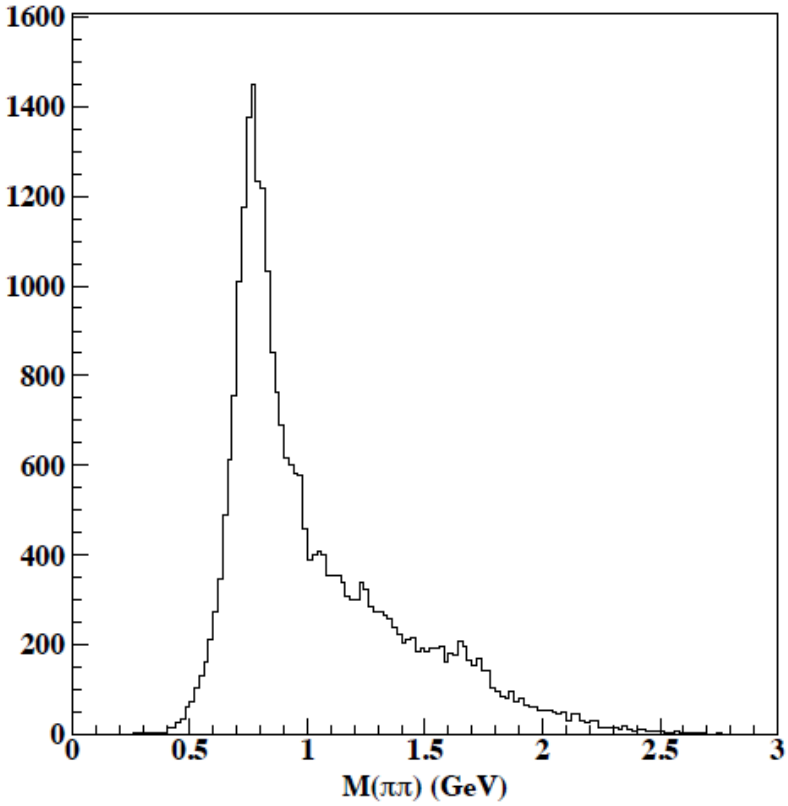

Figure 4.17. The invariant mass distribution of $\pi^+\pi^-$ in the reaction $\gamma d \to \pi^+\pi^- d$. The distribution is not corrected for detector efficiency.

4.3.2 Final state K^+K^-d

Slightly larger cut was applied to ΔE kaon pair distribution, shown in **Figure 4.18**. The cut for selection of K^+K^-d was $|\Delta E| < 0.025\,\mathrm{GeV}$. The background in the kaon events after this cut was estimated to be $\sim 20\%$.

The scattering angle vs. momentum distributions for all three particles in the final K^+K^-d events are shown in **Figure 4.19**. The average momentum of deuterons somewhat larger than in case of $(\pi^+\pi^-)$ since the minimum transferred momentum squared is larger. The final invariant mass distribution of kaon pairs shown in **Figure 4.20** showing $\varphi^0(1020)$ meson at $m \sim 1\ GeV$ and a broad distribution centered at $\sim 1.6\ GeV$ and extending up to $2.6\ GeV$.

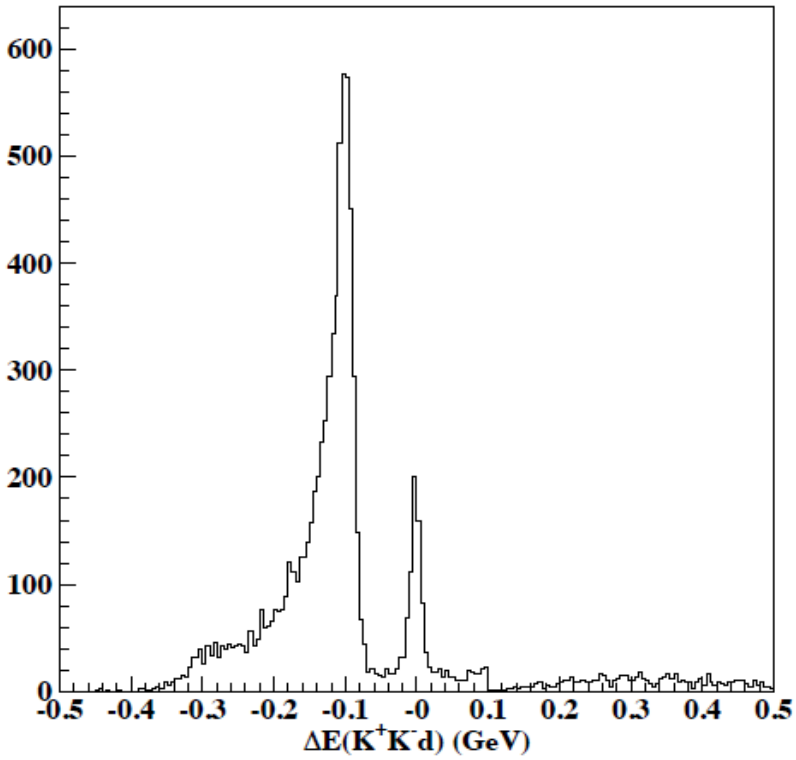

Figure 4.18. The ΔE distribution for K^+K^-d final events.

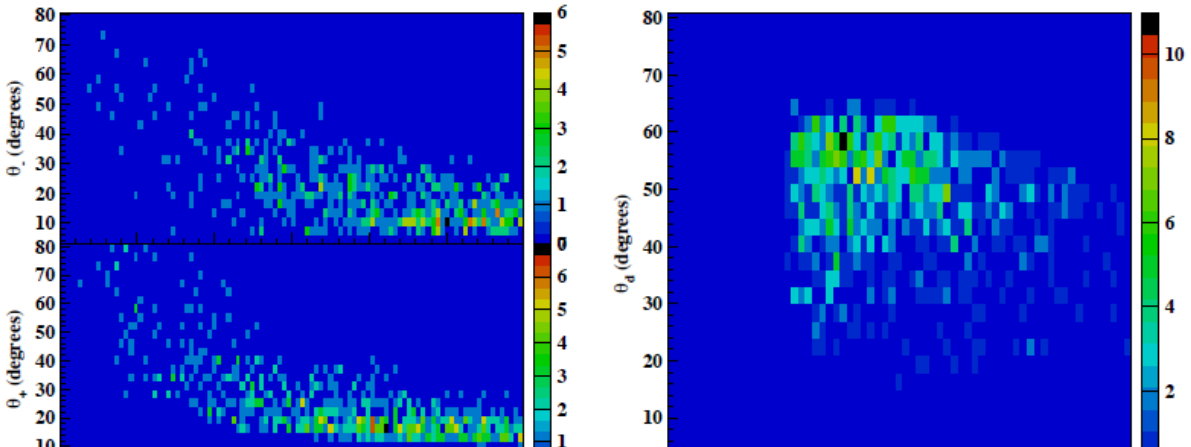

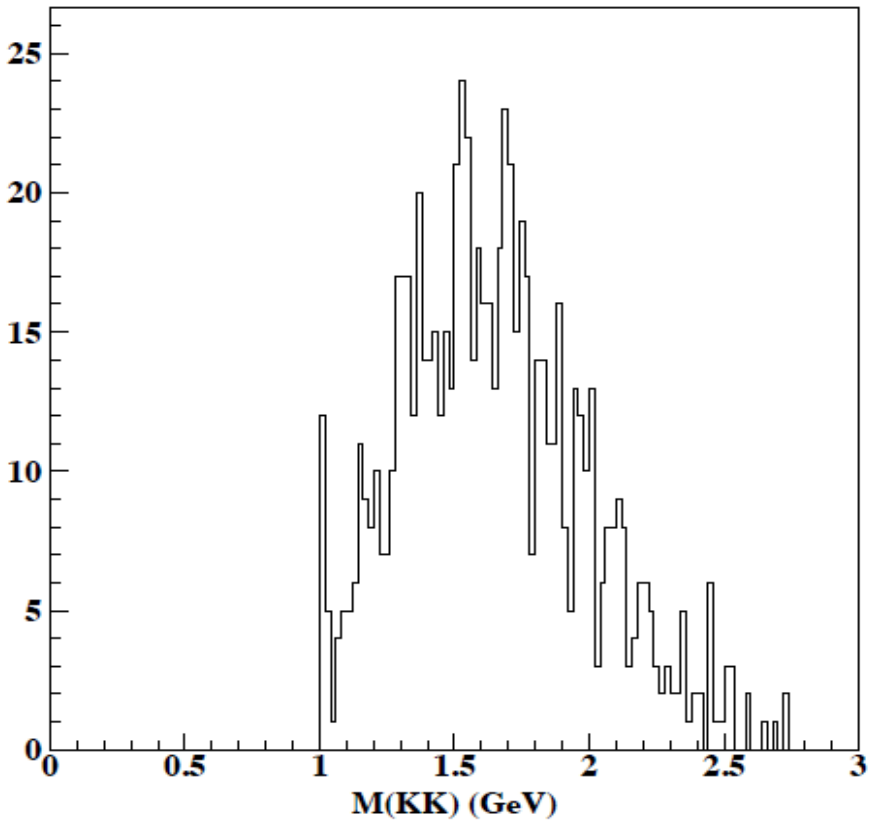

Figure 4.20. The invariant mass distribution of K^+K^- in the reaction $\gamma d \to K^+K^- d$. The distribution is not corrected for detector efficiency.

4.3.3 Final state $p\bar{p}d$

In **Figure 4.21** the ΔE distribution of $p\bar{p}d$ events selected after loose PID cut is shown. The final sample was selected with $|\Delta E| < 0.05\ GeV$ cut. The scattering angle vs. momentum distributions for all three particles in the final $p\bar{p}d$ events are shown in **Figure 4.22**. Due to large minimum transferred momentum square defined by energy range $4.5\ GeV < E_\gamma < 5.5\ GeV$ and large final state $p\bar{p}$ invariant mass, see **Figure 4.23**, the average momentum of deuterons is $\sim 1.25\ GeV$ and they produced mostly in forward region, $\theta < 40^0$.

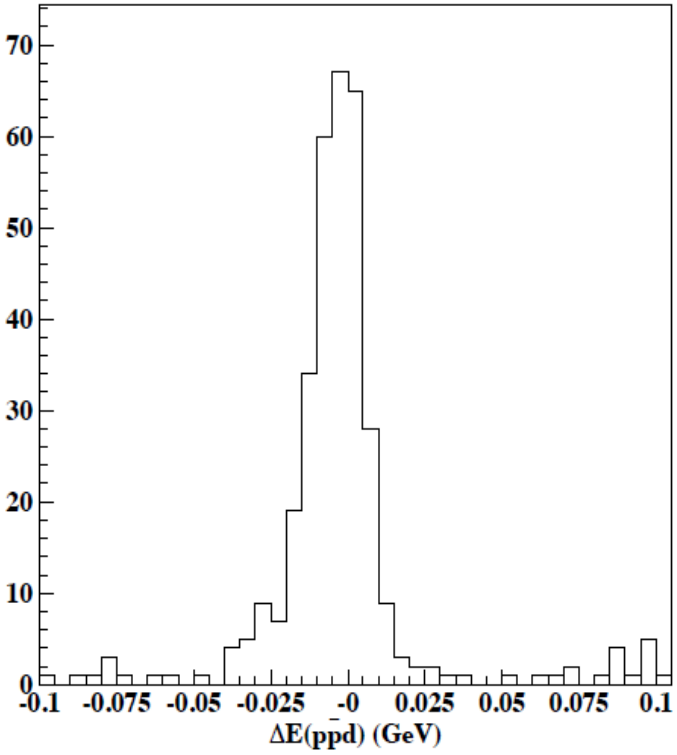

Figure 4.21. The ΔE distribution for $p\bar{p}d$ final events.

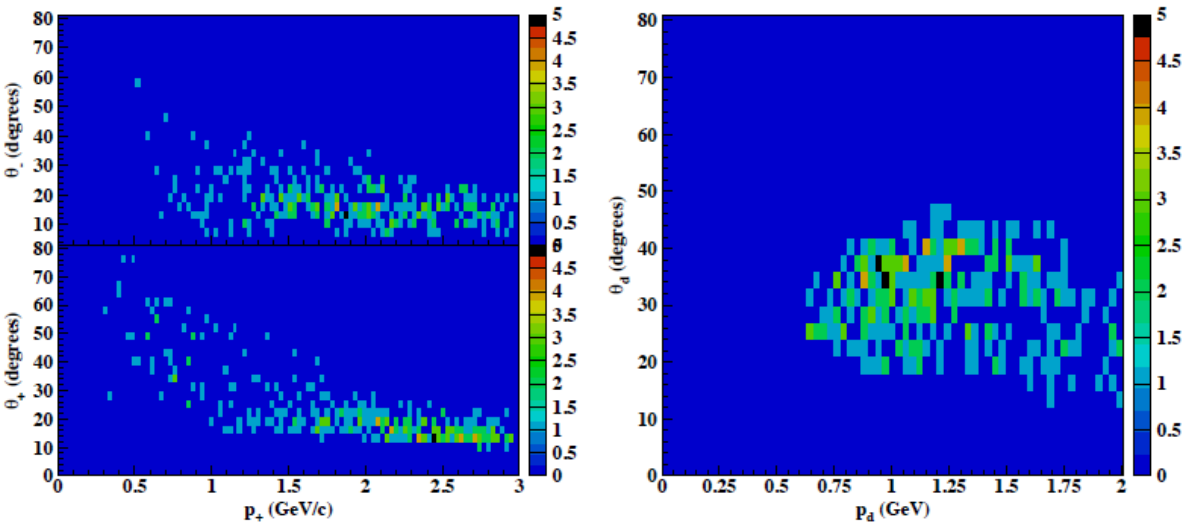

Figure 4.22. The scattering angle, $\boldsymbol{\theta}$, vs momentum for proton/anti-protons (left) and deuteron (right) for final $\mathbf{p\bar{p}d}$ events.

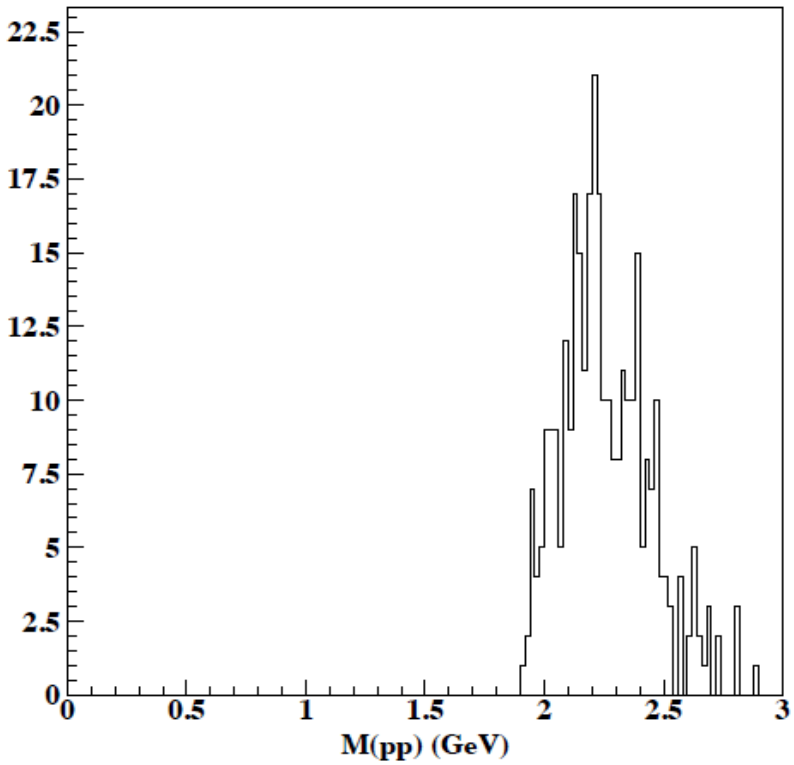

Figure 4.23. The invariant mass distribution of $\mathbf{p\bar{p}}$ in the reaction $\boldsymbol{\gamma d \rightarrow p\bar{p}d}$. The distribution is not corrected for detector efficiency.

4.4 Acceptance simulations

In order to calculate the cross section from experimental yields, the detector efficiency needs to be calculated. The efficiency was obtained by passing the simulated events through the same reconstruction program used for the measured data, and by calculating

$$\text{Acceptance} = \frac{\text{Number of reconstructed events in a bin}}{\text{Number of generates events in the same bin}} \qquad (4.3.0)$$

The effciency of the CLAS detector for detecting three particles in final state in the exclusive coherent photoproduction reactions:

$$\gamma d \rightarrow d' p \bar{p}$$

$$\gamma d \rightarrow d' K^+ K^- \qquad (4.3.1)$$
$$\gamma d \rightarrow d' \pi^+ \pi^-$$

was determined using the standard chain of simulation tools: EvGen (**Ev**ent **Gen**erator) /GSIM (**G**eant **Sim**ulation) /GPP (**G**EANT **P**ost **P**rocessor) /Recsis (**Rec**onstruction system).

4.4.1 Event Generator

In the event generator step, events are produced as much like real events as possible up to of our level knowledge. For an unknown production channel, it is typical to produce events according to the phase space distribution, where events are evenly distributed in the phase space. Event generator did not include any resonances, the kinematics of the final state particles were generated using a t-channel production model, see **Figure 1.7**, where mass of the pair, $p\bar{p}$, K^+K^-, $\pi^+\pi^-$ produced in the t-channel was constrained by the phase space and has different shapes for each final state. The decay angular distribution in the pair CM system was simulated isotropically. The bremsstrahlung spectrum was used for beam photons energy distribution. An exponential t-dependence was assumed with the slope of 3 $(GeV/c)^{-2}$:

$$\sigma \propto e^{-3|t|} \qquad (4.3.2)$$

4.4.2 GSIM

The basis of the acceptance calculation is the GEANT-based simulation (GSIM) of the CLAS detector, which is the CLAS standard simulation package.

After events are produced by the event generator, they are processed by GSIM. GSIM propagates each particle through all CLAS components from the vertex produced by the event generator. The particles travel through the simulated detector where it is possible for them to lose energy due to ionization, decay with probabilities according to PDG values, and undergo multiple-scattering with detector materials as it would happen in the real detector.

The package also simulates the response of each detector component to the incident particles. The digitized signals from each component are collected and stored just like real experimental data.

4.4.3 GSIM Post Processing

The GSIM output is then processed by the GSIM Post Processing (GPP) package, which smears the detector signals to be more realistic. The scintillator timing is

smeared according to the length of the scintillator. GPP also smears the drift chamber signal according to the average drifting time of ionization electrons to the sensor wires. GPP has a series of parameters allowed to be changed by users to match with the resolution of each experiment.

The output of GSIM is then processed by the analysis program and by the analysis thereafter just like experimental data.

4.4.4 Acceptance Calculation

The trigger for eg3 run period included only tagger T-counters for photon energies above 4.5 GeV, and this created a discontinuity in the event yield versus photon energy at around 4.5 GeV. It also required in at least three

sectors for each event (as discussed in trigger efficiency section). The simulation of this is easily done by requiring that each event reconstructed has tracks coming from at least three sectors.

For all completed simulation files we applied the same cuts used on the experimental data to calculate the acceptance. These include the vertex timing cuts that were made on the skimmed data, the energy conversion. All the corrections were also applied to the simulated data in order to achieve reliable acceptance for the selection cuts that were applied as part of the two-pion skim program.

In **Figure 4.24** simulated mass and transferred momentum distributions are shown for two decay modes: $\pi^+\pi^-$ (left) and $p\bar{p}$ (right). The lower 1D plots are projections of top ones to the x-axis and show simulated transferred momentum squared distributions (simulated t-dependancies).

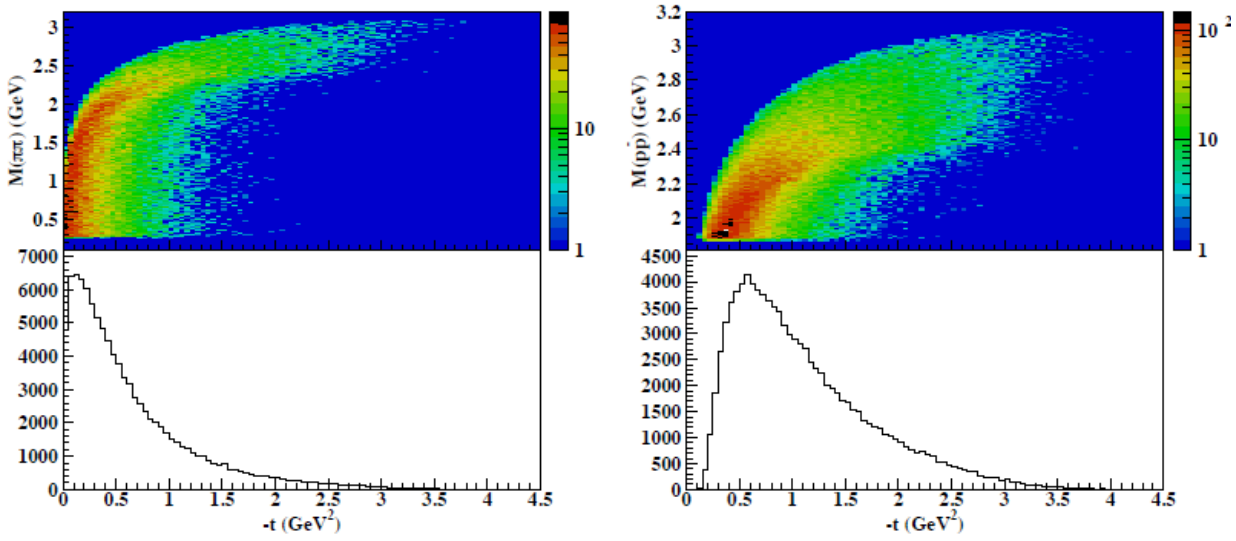

Figure 4.24 The simulated mass vs. transferred momentum distribution for, $\pi^+\pi^-$ (left) and $p\bar{p}$ (right).

A full information for the simulated and reconstructed events were stored in HBOOK column-wise Ntuples. A total of 10 million events were simulated and processed for each reaction in **Equation 4.1**. After the processing the same analysis code that was used for analysis of experimental data is used also for analysis of the simulated data for determination of acceptances. As an acceptance correction the ratio of the number of reconstructed events in each kinematic bin to the number of simulated events in that bin was taken.

In **Figure 4.25** comparison of the t- and the invariant mass dependences of coherent $\pi^+\pi^-$ production from simulation and the experiment are shown. The same distributions for the K^+K^-, and $p\bar{p}$ are shown in **Figures 4.26** and **4.27**, respectively. The exponential t-dependence used in the event generator for all three final states reproduces the dependences in the experimental data reasonably well. This is important since the CLAS acceptance varies strongly with the particle angle and momentum, especially in forward direction, and the correct simulation of kinematics of the final sate particles is required for correct determination of the acceptance correction factors.

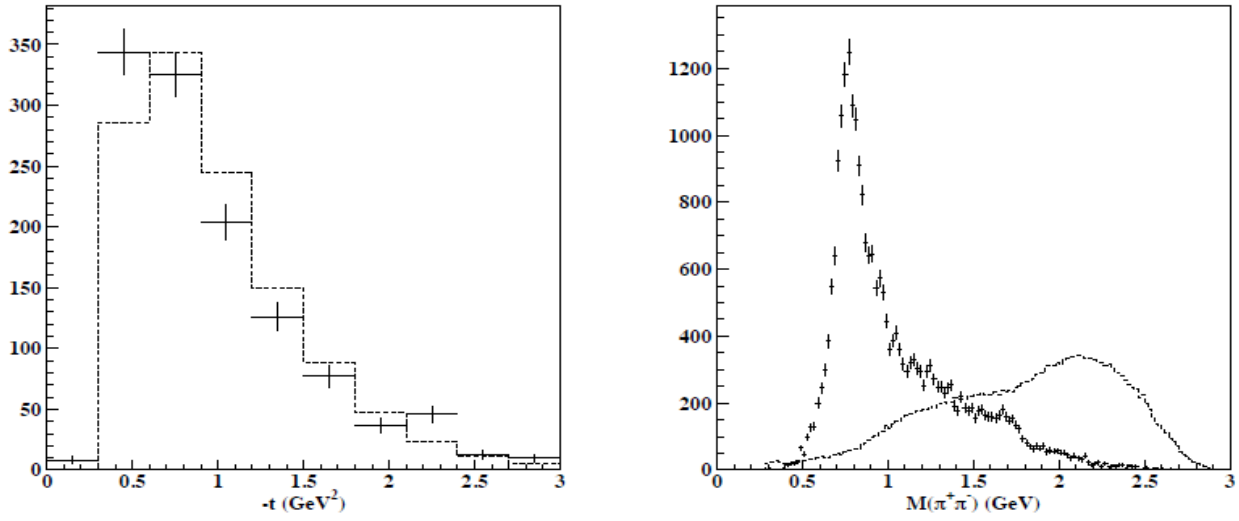

Figure 4.25 Comparison of the t – (left) and the invariant mass (right) distributions from data, points with error bars, and the reconstructed events simulations, dotted histograms, for $\pi^+\pi^-$.

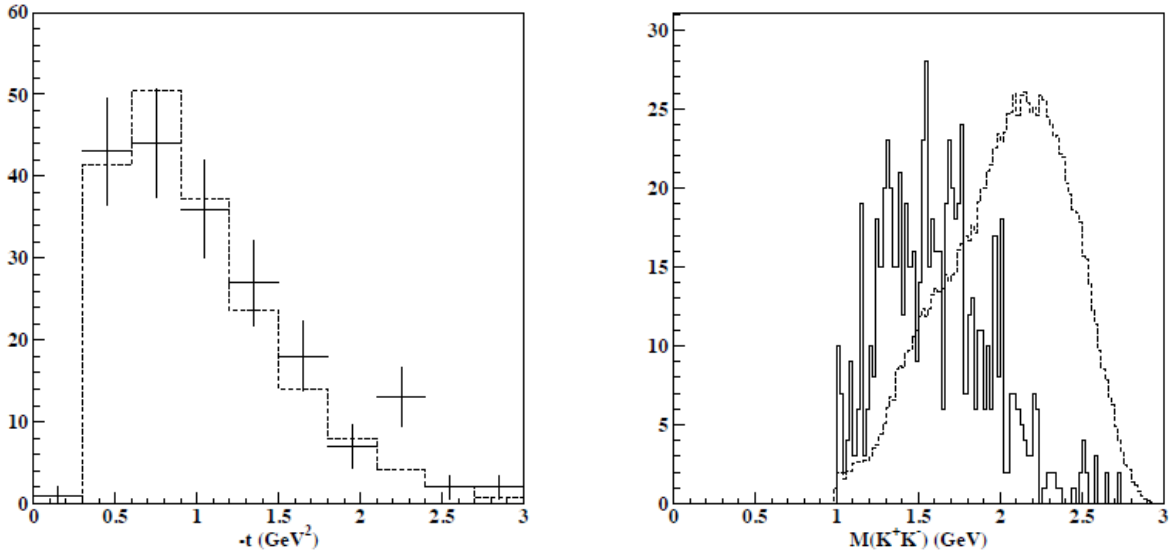

Figure 4.26 Comparison of the t – (left) and the invariant mass (right) distributions from data, points with error bars, and the reconstructed events simulations, dotted histograms, for $\mathbf{K^+K^-}$.

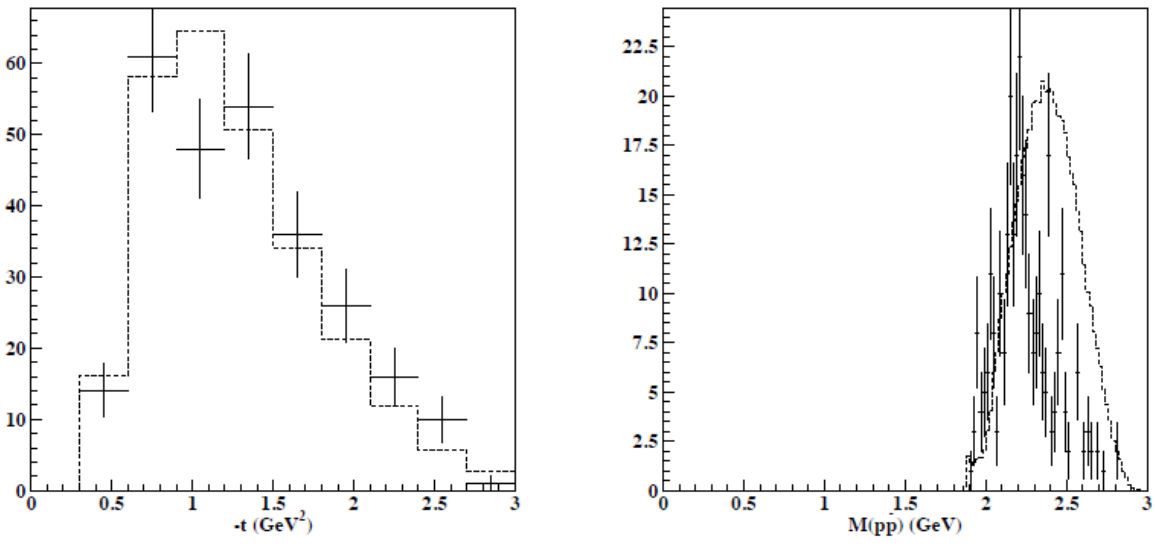

Figure 4.27 Comparison of the t – (left) and the invariant mass (right) distributions from data, points with error bars, and the reconstructed events simulations, dotted histograms, for $\mathbf{p\bar{p}}$.

On the other hand, since the event generator does not have any specific dynamics, no resonances or energy dependent production rate were implemented other than the phase space and bremsstrahlung beam energy spectrum, the invariant mass distributions in the simulation and in the data are different. However, since the goal of this analysis is to extract yields in a small invariant mass range above two proton mass, this difference will not play significant role in the acceptance calculations.

Detector acceptance corrections have been calculated in each kinematic bin. In **Figure 4.28** the 2D distribution of the ratios of reconstructed to simulated invariant mass vs $\cos\theta_{CM}$ distributions are shown for both the $\pi^+\pi^-$ (top) and $p\bar{p}$ (bottom) final states. In average the acceptance for both is in few % range. The acceptance for the $p\bar{p}$ is $\times 2$ smaller than for $\pi^+\pi^-$.

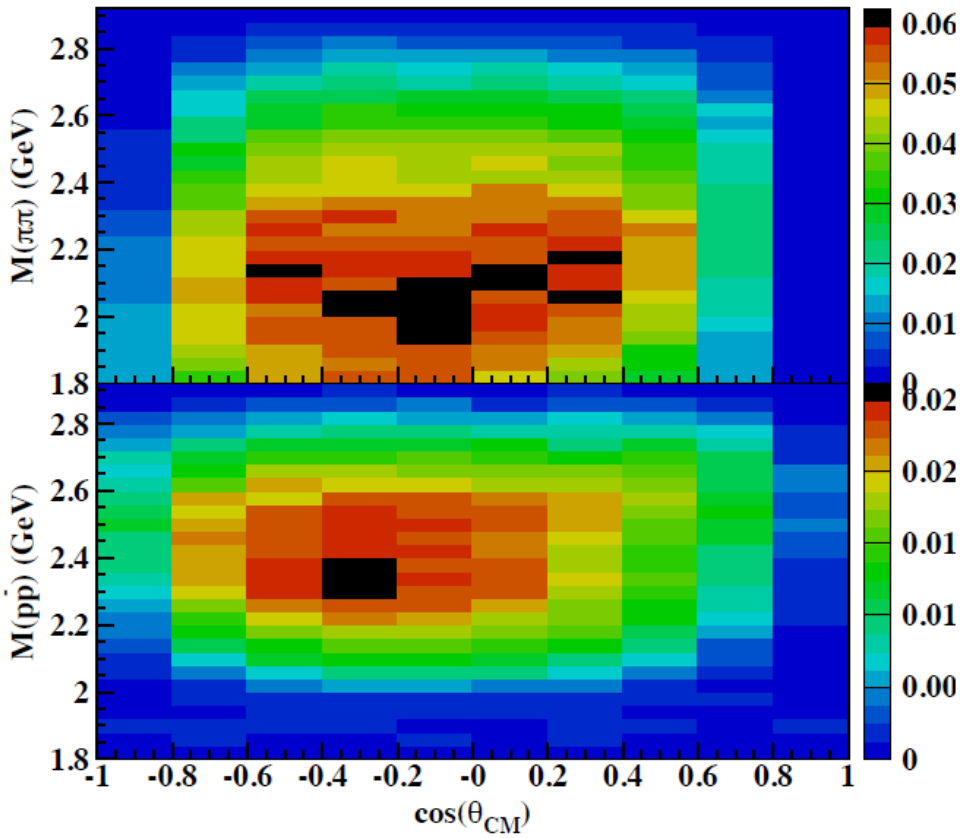

Figure 4.28 The CLAS acceptance (z-axis) as function of mass and $\cos\theta_{CM}$ for $\pi^+\pi^-$ (top) and $p\bar{p}$ (bottom) production reactions on deuterium as described in **Equation 4.1**

In **Figure 4.29**, acceptances as a function of pair invariant mass are shown. Events were integrated in all other kinematic variables. The acceptance is the largest for pion final state in the whole mass range. At given invariant mass of pair, acceptance for lightest mass pair is larger than for heaviest pair, as one would expect since CLAS has a poor detection acceptance in the forward region.

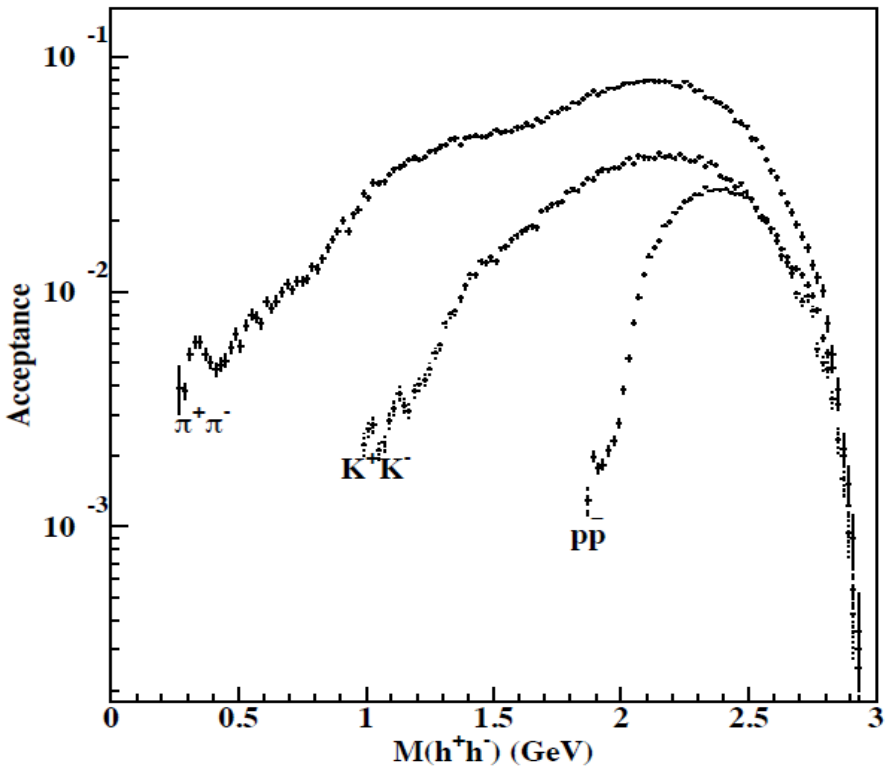

Figure 4.29 CLAS acceptance for three coherent reactions as a function of pair invariant mass.

One of important checks for the current analysis is the coherent production of ρ^0 meson. This reaction has been studied in other experiments. In **Figure 4.30**, the t- and $\cos\theta^*$ dependences of ρ detection acceptances are shown.

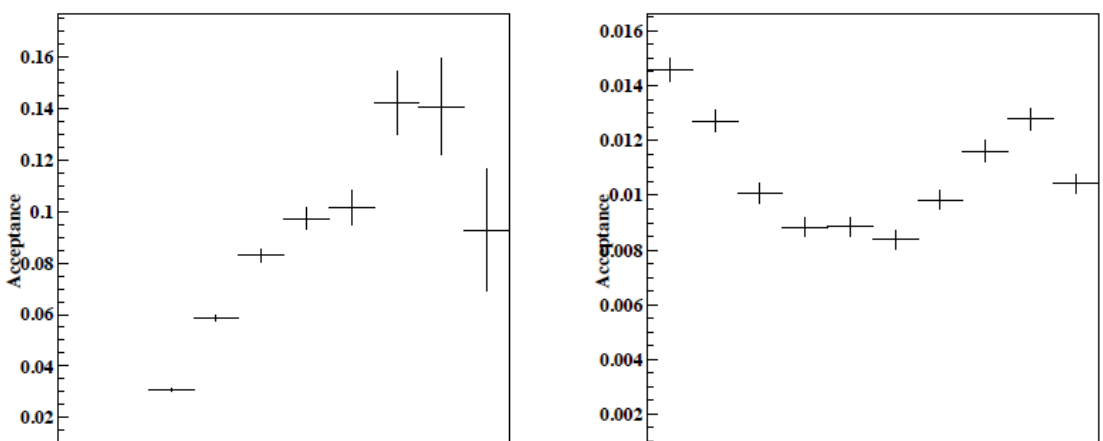

The t- and $\cos\theta^*$ dependancies for $\pi^+\pi^-$ (left) and $p\bar{p}$ (right) final states are shown in **Figures 4.31** and **4.32** for pair invariant mass range from 1.9 GeV to 2.5 GeV.

Acceptances were obtained for K^+K^- channel as well. These acceptance values were used in order to extract yields and cross sections for all three channels, see below.

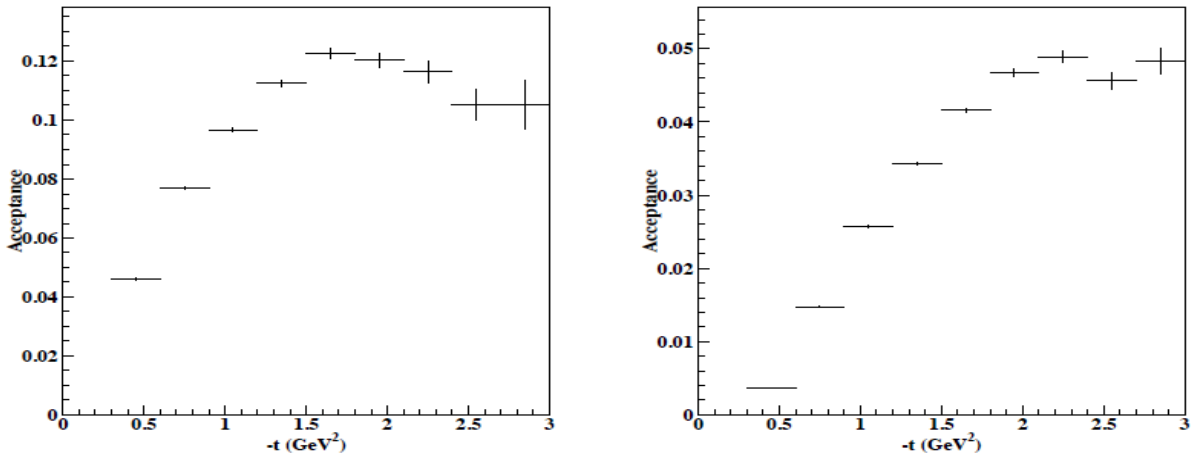

Figure 4.31 Detector acceptance for $\pi^+\pi^-$(left) and $p\bar{p}$ in the invariant mass region from 1.9 GeV to 2.5 GeV as a function of transferred momentum squared.

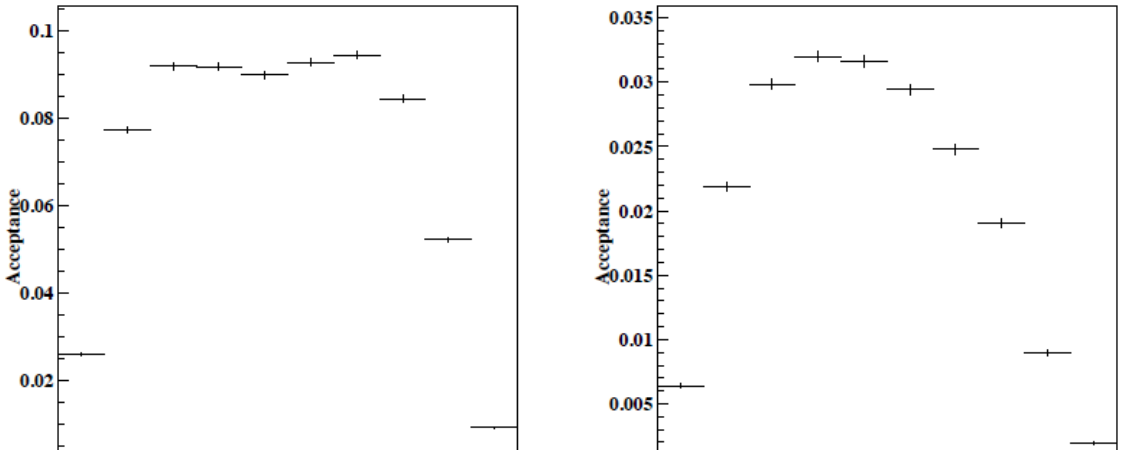

Chapter 5

5.1 Results

The final results of this analysis are presented in forms of differential cross sections of exclusive coherent photoproduction of $p\bar{p}$, K^+K^- and $\pi^+\pi^-$ pairs on deuterium in a wide range of pair invariant mass and as a function of the pair invariant mass, $M(h^+h^-)$ transferred momentum squatted, t, and the scattering angle of the positively charged particle in the pair helicity frame (CM system of the pair with z-axis in the direction of pair CM three-momentum), $cos\,\theta_{CM}$. Due to limited statistics, the cross sections are integrated over the tagged photon energy range from 4.5 GeV to 5.6 GeV (energy region in the trigger).

The differential cross section in each bin of the kinematical variable x was defined as:

$$\frac{d\sigma}{dx} = \frac{n_i}{L \cdot \epsilon_i} \cdot \eta \tag{5.1}$$

where n_i is the number of events in the given bin, ϵ_i is the detector effciency (acceptance), L is the luminosity, and the η is for the trigger effciency correction. The luminosity is calculated as a product of the incoming photon flux, N_γ, integrated in the energy range from 4.5 GeV to 5.6 GeV, and the number of target nuclei:

$$L = \frac{N_\gamma \cdot \rho_D \cdot l_t \cdot N_A}{A} \tag{5.2}$$

where the N_γ was calculated using the "gflux" files for each of 205 production runs used for the analysis (see **Appendix**). The density of the LD2 target was taken as $\rho_D = 0{,}169\ g/cm^3$, $N_A = 6{,}022 \times 10^{23}\ mol^{-1}$ is the Avogadro number, l_t is the length of the liquid deuterium target and was taken as 40 cm, and the A is the atomic number of the deuteron. The trigger effciency determined in previous "eg3 run" analysis [**5.1**] was used. For data acquired in 2004 this

effciency factor was 1.7. For 2005 data the normalization factor was 3.1. The systematic errors on extracted cross sections are dominated by uncertainties of the trigger effciency normalization factors and by acceptances.

The uncertainties for the trigger effciency corrections was estimated to be $\sim 30\%$, the acceptance correction uncertainties $\sim 25\%$. These factors give overall systematic uncertainties of order of $\sim 40\%$ (including couple % uncertainty for the photon flux normalization and the target density). For K^+K^- final state, an additional 15% uncertainty is added due to final state selection cuts.

As a check for cross section extraction procedures, cross secton of the reaction $\gamma d \to \rho^0 d'$ was extracted and compared with SLAC measurements [**5.2**]. The ρ events were selected using a cut on the invariant mass of the $\pi^+\pi^-$, $0.55\,GeV < M(\pi^+\pi^-) < 0.9\,GeV$. This selection of the ρ^0 events does not account for the background under the ρ peak and the $\rho^0 \to \pi^+\pi^-$ events above the $\pi^+\pi^-$ invariant mass of 0.9 GeV, and therefore introduces an additional systematic error in the cross section calculation. The systematic uncertainties due to such a simple selection was estimated to be 25%. The estimate was done using the number of events in the tail of the $\pi^+\pi^-$ invariant mass distribution from ρ^0 decay above 0.9 GeV from the simulation, and the estimates of the non-resonant $\pi^+\pi^-$ background under the ρ^0 in the selected mass range from the hydrogen data analysis. In **Figure 5.1** differential cross sections, $\frac{d\sigma}{dt}$ (left) and $\frac{d\sigma}{d\cos\theta_{CM}}$ (right), for coherent ρ^0 photoproduction on deuterium are shown. In the t-dependence graph the filled symbols are SLAC measurements.

In **Figure 5.1** the lowest $|t|$-point, at 0.7 GeV^2, is at the edge of the detector acceptance (forward going pions) and has much larger uncertainties due to the acceptance corrections than what was quoted above. The rest of the

points are in reasonable agreement with SLAC data. The CM π^+ angular dependance of the cross section has $1 - cos^2\theta_{CM}$ dependence as expected from SCHC. As in the case of small $|t|$ point on the left graph, the highest $cos\,\theta_{CM}$ point is at the edge of the detector acceptance, has much larger uncertainties and has not been included in the fit (shown with dashed line on the graph).

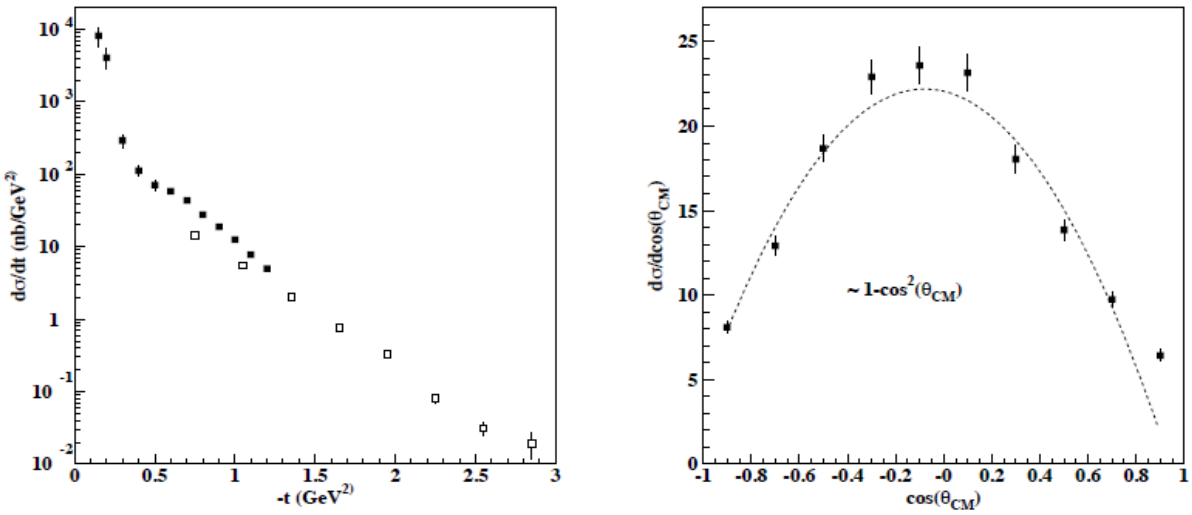

Figure 5.1 The differential cross section of coherent $\boldsymbol{\rho^0}$ photoproduction on deuterium as function transferred momentum squared (left graph) and the angle of $\boldsymbol{\pi^+}$ in the $\boldsymbol{\rho}$ helicity frame. The black points on the left graph are the old measurements from SLAC. The dashed line on the right graph is a fit with the function $\mathbf{a + b \cdot \cos\theta_{CM} + c \cdot \cos^2\theta_{CM}}$. The cross section are integrated over

In **Figure 5.2** the differential cross section, $\frac{d\sigma}{dM}$, is shown as a function of the pair invariant mass for all three coherent channels. For each reaction the

invariant mass range is covers from the threshold to 2.5 GeV. In the region of overlaps, the cross section of coherent kaon pair production (filled triangles) is 3 to 4 times smaller than $\pi^+\pi^-$ (filled squares) or $p\bar{p}$ (open squares) cross sections. Likewise, above the invariant mass of 1.95 GeV, the cross section for coherent $p\bar{p}$ production is larger than $\pi^+\pi^-$ production cross section by a factor of $\times 1.5$.

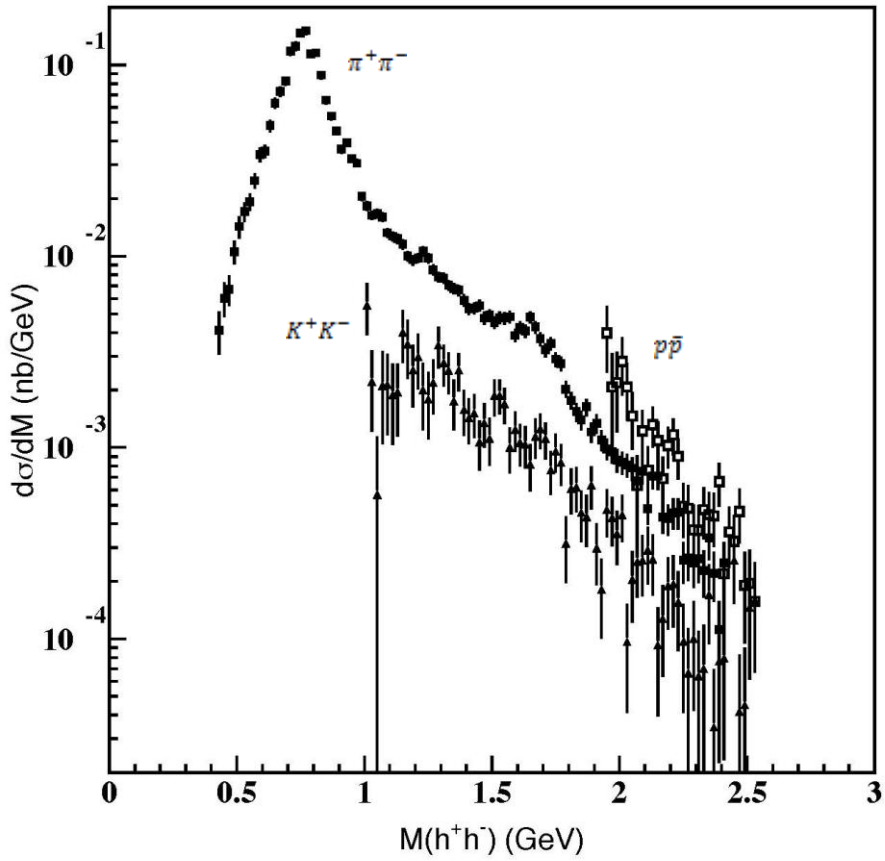

Figure 5.2 The differential cross section of coherent $\mathbf{p\bar{p}}$, $\mathbf{K^+K^-}$, and $\boldsymbol{\pi^+\pi^-}$ photoproduction on deuterium as function of pair invariant mass. The cross sections are integrated over photon energy range from 4.5 to 5.6 GeV.

In **Table.5.1,** values for cross sections and statistical errors for all three coherent channels are shown for mass range between 1.95 GeV and 2.53 GeV. The integrated total cross section for $p\bar{p}$ production is the kinematic of this analysis in the acceptance region of CLAS is σ**=0,68 ± 0.061 pb**.

Table 5.1 Differential cross section, $\frac{d\sigma}{dM}$ in nb/GeV, for three coherent reactions.

M(h^+h^-) GeV	$\sigma(\pi^+\pi^-)$	$\pm\delta\,\sigma(\pi^+\pi^-)$	$\sigma(K^+K^-)$	$\pm\delta\,\sigma(K^+K^-)$	$\sigma(p\bar{p})$	$\pm\delta\sigma(p\bar{p})$
1.95	0.98E-03	0.13E-03	0.47E-03	0.13E-03	0.40E-02	0.15E-02
1.97	0.95E-03	0.12E-03	0.43E-03	0.12E-03	0.21E-02	0.10E-02
1.99	0.86E-03	0.12E-03	0.36E-03	0.11E-03	0.22E-02	0.98E-03
2.01	0.84E-03	0.11E-03	0.44E-03	0.12E-03	0.28E-02	0.95E-03
2.03	0.81E-03	0.11E-03	0.97E-04	0.56E-04	0.21E-02	0.69E-03
2.05	0.78E-03	0.11E-03	0.20E-03	0.84E-04	0.15E-02	0.49E-03
2.07	0.67E-03	0.10E-03	0.25E-03	0.90E-04	0.63E-03	0.28E-03
2.09	0.75E-03	0.11E-03	0.26E-03	0.91E-04	0.12E-02	0.35E-03
2.11	0.48E-03	0.85E-04	0.29E-03	0.97E-04	0.76E-03	0.25E-03
2.13	0.71E-03	0.10E-03	0.26E-03	0.92E-04	0.13E-02	0.32E-03
2.15	0.71E-03	0.10E-03	0.93E-04	0.54E-04	0.11E-02	0.28E-03
2.17	0.44E-03	0.81E-04	0.13E-03	0.64E-04	0.69E-03	0.21E-03
2.19	0.42E-03	0.80E-04	0.19E-03	0.77E-04	0.10E-02	0.25E-03
2.21	0.46E-03	0.85E-04	0.19E-03	0.79E-04	0.12E-02	0.25E-03
2.23	0.46E-03	0.86E-04	0.16E-03	0.70E-04	0.90E-03	0.22E-03
2.25	0.26E-03	0.63E-04	0.97E-04	0.56E-04	0.49E-03	0.16E-03
2.27	0.27E-03	0.65E-04	0.66E-04	0.47E-04	0.48E-03	0.15E-03
2.29	0.25E-03	0.64E-04	0.10E-03	0.58E-04	0.37E-03	0.13E-03
2.31	0.26E-03	0.66E-04	0.64E-04	0.45E-04	0.37E-03	0.13E-03
2.33	0.23E-03	0.63E-04	0.70E-04	0.49E-04	0.47E-03	0.14E-03
2.35	0.34E-03	0.78E-04	0.17E-03	0.76E-04	0.45E-03	0.14E-03
2.37	0.22E-03	0.64E-04	0.35E-04	0.35E-04	0.44E-03	0.14E-03
2.39	0.11E-03	0.46E-04	0.77E-04	0.54E-04	0.66E-03	0.17E-03
2.41	0.25E-03	0.70E-04	0.79E-04	0.56E-04	0.22E-03	0.98E-04
2.43	0.22E-03	0.67E-04	0.00E+00	0.00E+00	0.36E-03	0.13E-03
2.45	0.18E-03	0.63E-04	0.26E-03	0.11E-03	0.32E-03	0.12E-03
2.47	0.14E-03	0.55E-04	0.42E-04	0.42E-04	0.46E-03	0.15E-03
2.49	0.14E-03	0.58E-04	0.45E-04	0.45E-04	0.19E-03	0.95E-04
2.51	0.16E-03	0.65E-04	0.15E-03	0.84E-04	0.19E-03	0.97E-04
2.53	0.27E-04	0.27E-04	0.16E-03	0.92E-04	0.16E-03	0.91E-04

The cross section of $p\bar{p}$ production does not exhibit any resonance structure between 1.95 GeV and 2.5 GeV, as shown separately in **Figure 5.3**.

The t-dependance of cross sections for both $\pi^+\pi^-$ and $p\bar{p}$ are shown in **Figure 5.4**. The t- dependance is studied for two invariant mass ranges, $1.9\ GeV < M < 2.5\ GeV$ (left graph) and $2.2\ GeV < M < 2.3\ GeV$ (right graph). The open symbols on the graphs are for $p\bar{p}$ final state, the filled symbols are for pion final state. On both graphs, the $p\bar{p}$ points are fited with an exponential function, shown with the dashed lines. For the wider mass range the t-dependance is slightly softer, 1.54 vs. 1.74 for slopes, respectively. The numerical values of t-dependance of cross section for $\pi^+\pi^-$ and $p\bar{p}$ are present

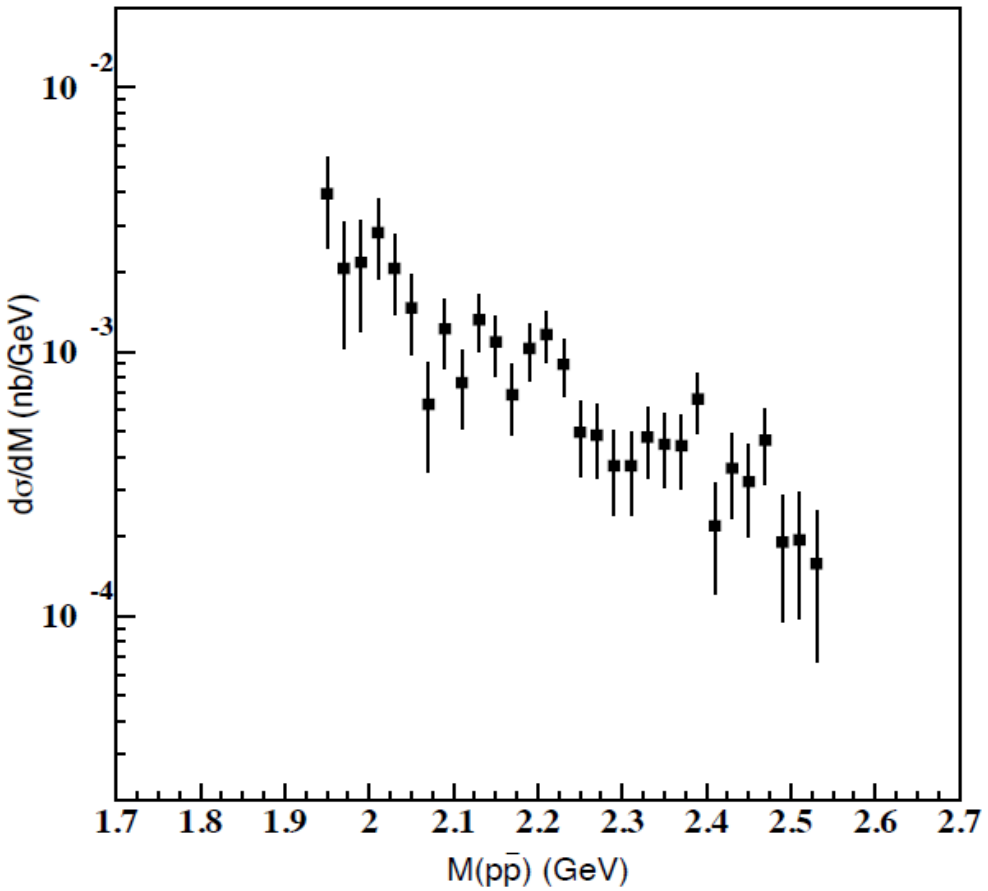

Figure 5.3 The differential cross section of coherent $\mathbf{p\bar{p}}$ photoproduction on deuterium as function of $\mathbf{p\bar{p}}$ invariant mass.

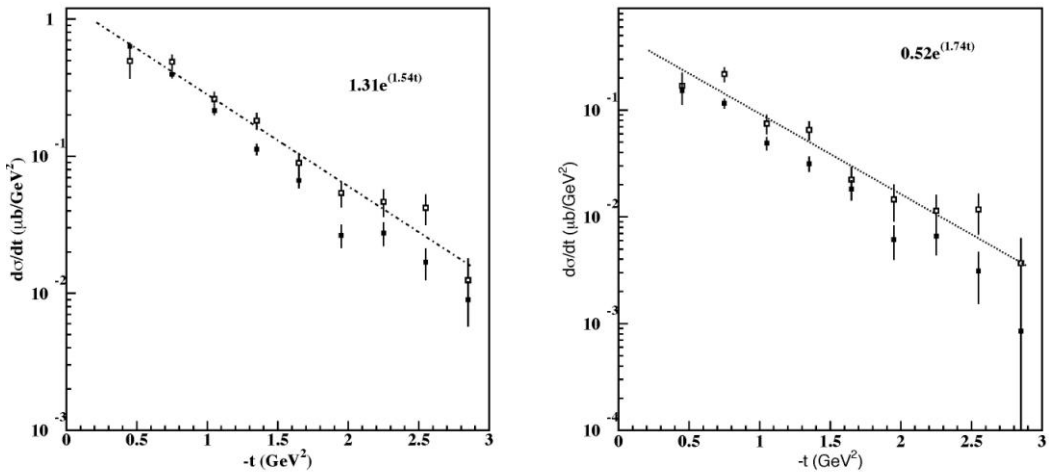

Figure 5.4 The differential cross section of coherent $\mathbf{p\bar{p}}$ (open symbols), and $\boldsymbol{\pi^+\pi^-}$ (filled symbols) photoproduction on deuterium as function of transferred momentum. The left graph for the paor invariant mass range from 1.9 GeV to 2.5 GeV. On the right, the t-dependence for the invariant mass range 2.1 GeV to 2.3 GeV.

The $cos\,\theta_{CM}$-dependence of the cross sections for $\pi^+\pi^-$ and $p\bar{p}$ was also studied in two different invariant mass regions as well. In **Figure 5.5** these dependencies are shown. The left graph is for the pair invariant mass range from $1.9\ GeV < M < 2.5\ GeV$, the right one is for $2.2 GeV < M < 2.3\ GeV$. The open symbols on the graphs are for $p\bar{p}$ final state, the filled symbols are for pion final state. The $cos\,\theta_{CM}$ distributions were fitted with function:

$$f = a + b \cdot \cos\theta_{CM} + c \cdot \sin\theta_{CM} \cdot \cos\theta_{CM} + d \cdot \cos^2\theta_{CM} \qquad (5.3)$$

The numerical values of cross section and statistical errors are shown in **Tables 5.4** and **5.5.** The point at $cos\,\theta_{CM} = 0.9$ was not included in the fit. For $p\bar{p}$ in both mass regions the $cos\,\theta_{CM}$ and $cos^2\,\theta_{CM}$ terms are dominant, while for the pion pair production the $cos^2\,\theta_{CM}$ is dominant. More detail angular analysis will be needed for correct determination of the spin of the intermediate states.

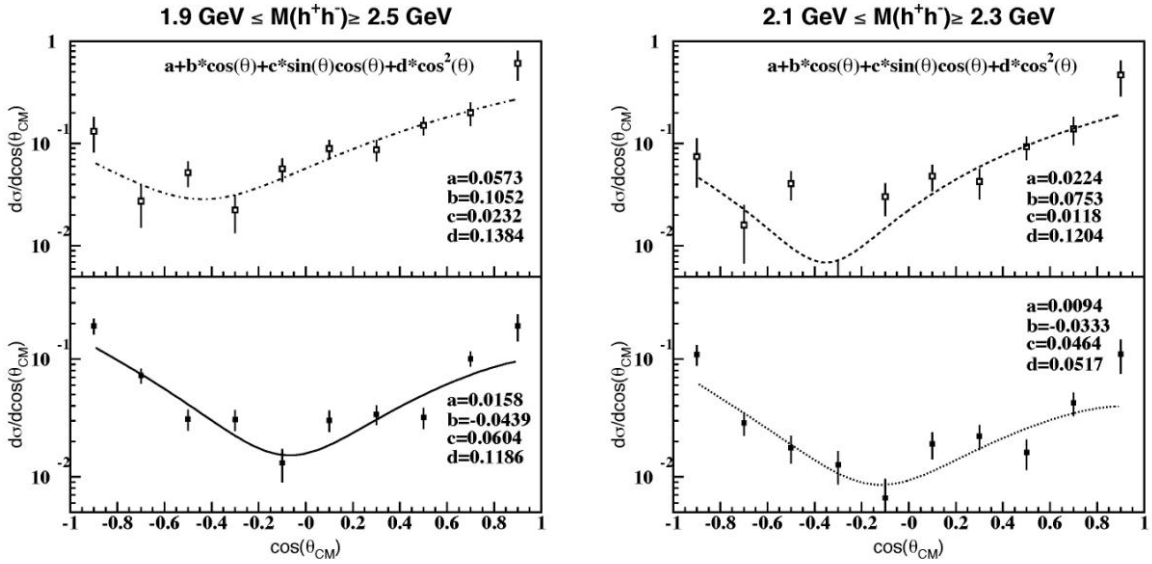

Figure 5.5: The differential cross section of coherent $p\bar{p}$ (open symbols), and $\pi^+\pi^-$ (filled symbbols) photoproduction on deuterium as function of positive particle angle in the pair helicity frame. The left graph is for the pair invariant mass range from 1.9 GeV to 2.5 GeV. On the right, the –

$\cos\theta_{CM}$	$\sigma(\pi^+\pi^-)$	$\pm\delta\sigma(\pi^+\pi^-)$	$\sigma(p\bar{p})$	$\pm\delta\sigma(p\bar{p})$
0.45	0.60E+00	0.39E-01	0.50E+00	0.13E+00
0.75	0.38E+00	0.24E-01	0.49E+00	0.63E-01
1.05	0.21E+00	0.16E-01	0.26E+00	0.35E-01

Table 5.2: Differential cross section, $\frac{d\sigma}{dt}$ in nb/GeV^2, for $\pi^+\pi^-$ and $p\bar{p}$ coherent photoproduction on deuterium integrated in the invariant mass range of pair from 1.9 GeV to 2.5 GeV.

1.35	0.11E+00	0.11E-01	0.18E+00	0.25E-01
1.65	0.64E-01	0.79E-02	0.89E-01	0.16E-01
1.95	0.26E-01	0.50E-02	0.54E-01	0.12E-01
2.25	0.27E-01	0.53E-02	0.47E-01	0.11E-01
2.55	0.16E-01	0.43E-02	0.42E-01	0.11E-01
2.85	0.79E-02	0.30E-02	0.12E-01	0.56E-02

Table 5.3: Differential cross section, $\frac{d\sigma}{dt}$ in nb/GeV^2, for $\pi^+\pi^-$ and $p\bar{p}$ coherent photoproduction on deuterium integrated in the invariant mass range of pair from 2.1 GeV to 2.3 GeV.

$\cos\theta_{CM}$	$\sigma(\pi^+\pi^-)$	$\pm\delta\,\sigma(\pi^+\pi^-)$	$\sigma(p\bar{p})$	$\pm\delta\sigma(p\bar{p})$

-0.90	0.19E+00	0.29E-01	0.13E+00	0.50E-01
-0.70	0.72E-01	0.10E-01	0.27E-01	0.12E-01
-0.50	0.31E-01	0.62E-02	0.52E-01	0.15E-01
-0.30	0.31E-01	0.63E-02	0.23E-01	0.92E-02
-0.10	0.13E-01	0.42E-02	0.57E-01	0.15E-01
0.10	0.30E-01	0.62E-02	0.90E-01	0.19E-01
0.30	0.34E-01	0.64E-02	0.87E-01	0.21E-01
0.50	0.32E-01	0.65E-02	0.15E+00	0.31E-01
0.70	0.10E+00	0.15E-01	0.20E+00	0.52E-01
0.90	0.19E+00	0.48E-01	0.61E+00	0.19E+00
1.95	0.61E-02	0.22E-02	0.15E-01	0.55E-02
2.25	0.66E-02	0.22E-02	0.11E-01	0.47E-02
2.55	0.31E-02	0.16E-02	0.12E-01	0.49E-02
2.85	0.85E-03	0.86E-03	0.37E-02	0.26E-02

-t	$\sigma(\pi^+\pi^-)$	$\pm\delta\sigma(\pi^+\pi^-)$	$\sigma(p\bar{p})$	$\pm\delta\sigma(p\bar{p})$
0.45	0.15E+00	0.23E-01	0.17E+00	0.56E-01
0.75	0.12E+00	0.12E-01	0.22E+00	0.34E-01
1.05	0.49E-01	0.69E-02	0.75E-01	0.16E-01
1.35	0.31E-01	0.52E-02	0.65E-01	0.13E-01
1.65	0.18E-01	0.39E-02	0.22E-01	0.71E-02

Table 5.4: Differential cross section, $\frac{d\sigma}{dm_{\pi\pi}dt}$ in nb, for $\pi^+\pi^-$ and $p\bar{p}$ coherent photoproduction on deuterium integrated in the invariant mass range of pair from 1.5 GeV to 2.5 GeV

Table 5.5: Differential cross section, $\frac{d\sigma}{d\cos\theta_{CM}}$ in nb, for $\pi^+\pi^-$ and $p\bar{p}$ coherent photoproduction on deuterium integrated in the invariant mass range of pair from 1.5 GeV

$\cos\theta_{CM}$	$\sigma(\pi^+\pi^-)$	$\pm\delta\,\sigma(\pi^+\pi^-)$	$\sigma(p\bar{p})$	$\pm\delta\sigma(p\bar{p})$
-0.90	0.11E+00	0.22E-01	0.75E-01	0.38E-01
-0.70	0.29E-01	0.65E-02	0.16E-01	0.92E-02
-0.50	0.18E-01	0.47E-02	0.41E-01	0.13E-01
-0.30	0.13E-01	0.40E-02	0.37E-02	0.37E-02
-0.10	0.66E-02	0.30E-02	0.30E-01	0.11E-01
0.10	0.19E-01	0.49E-02	0.48E-01	0.14E-01
0.30	0.22E-01	0.53E-02	0.43E-01	0.14E-01
0.50	0.16E-01	0.47E-02	0.93E-01	0.24E-01
0.70	0.42E-01	0.96E-02	0.14E+00	0.42E-01
0.90	0.11E+00	0.36E-01	0.47E+00	0.18E+00

Summary

In this analysis, for the first time, we studied coherent production of hadron anti-hadron pairs on deuterium, $\gamma d \to h^+h^-d'$ using up to 5.5 GeV photon beam at large invariant mass region. The aim of the analysis was to investigate the invariant mass region of hadron pair above 2 GeV in order to check claims of several groups on existence of meson resonances. Two states decaying to $p\bar{p}$ have been reported in the past, one at 2.02 GeV, another at 2.2 GeV. Coherent production on deuterium has an advantage compared to the production on hydrogen. It eliminates ambiguities in the production mechanism, and contributions from s- and u-channels, only t-channel production is allowed. The hadron pairs that have been studied are $\pi^+\pi^-$, K^+K^-, and $p\bar{p}$. The fully exclusive final states were analyzed where together with hadron pair, the recoil deuterium was detected as well. Besides three exclusive final sates with detected deuteron, the reaction $\gamma d \to pp\pi^-$ also was studied and events that fit in the kinematics of this reaction were excluded in the second step of the analysis.

The analysis were carried out using data acquired with the CLAS detector in experimental Hall-B at Jefferson lab (USA). The Hall-B bremsstrahlung photon tagging facility has been used to produce tagged bremsstrahlung photon beam of up to 5.5 GeV energy. The target was 40 cm long liquid deuterium located ~40 cm upstream of the CLAS nominal center. The whole run, called CLAS "EG3" run period, was divided into two parts that differ in trigger settings. During the first part of the run, November-December of 2004, the main trigger was tagger hodoscopes in relevant energy region in

coincidence with a three prong event in CLAS. In the second half, January 2005, the CLAS start counter also was included in the trigger.

The CLAS torus was set to -1930 A during entire run, the negative sign corresponds to the direction of negatively charged particles bent outwards from the beam.

The physics analysis proceeded in two steps. First, using the exclusivity of the final states, the three-momentum conservation was used to select three charged tracks in final sates and to select correct hit in the tagger spectrometer hodoscope, which corresponds to the photon that produced the event in CLAS. In the second step, using loose particle identification cuts, final states have been identified. The particle identification in CLAS uses time-of-flight technique, in this analysis, in addition to time-of-flight the energy deposition in the scintillator counters has been used to aid identification of deuterons.

For identification of the three coherent exclusive reactions, the energy conservation was found to be a powerful kinematical cut. With the same three-momentum of final state particles, the differences of total energies in different final states, $\pi^+\pi^-$, K^+K^-, and $p\bar{p}$ are much bigger than the detector resolution and allows a clean separation of these reactions.

The final results of the analysis are presented in forms of distributions of events as a function of different physics quantities, the invariant mass of the pair, transferred momentum squared, t, and the decay angular distributions of positive hadron in the pair rest frame. The distributions were detector efficiency corrected using simulations. The event generator did not include any resonances, just a phase space. The GEANT3 model of CLAS was used together with GEANT post processor to include detector malfunctions.

Simulated events were processed with exactly the same software that was used for analysis of experimental data.

With limited statistics, no resonances have been seen in the invariant mass distributions of $p\bar{p}$ above 2 GeV after acceptance corrections. Similarly, no unknown resonances seen in $\pi^+\pi^-$ or K^+K^-final states. In pion final state ρ^0 is clearly seen, as well as Φ-meson in the K^+K^- final state. The t –dependences in all three channels exhibit exponential dependence, with slope getting softer at large invariant masses. The cross sections in all three reactions have been calculated using measured photon flux, target nuclei, and the trigger efficiency. The cross section for coherent ρ^0 photoproduction was compared with previously measured cross sections at SLAC and found to be in reasonable agreement. The decay angular distribution of π^+ shows correct behavior expected form SCHC.

The comparison of cross sections of three coherent reactions in the region of large invariant masses, >2 GeV, showed that kaon final state has 4-5 times lower yield than other two. Most importantly it turns out that the $p\bar{p}$ production rate is almost the same, even slightly higher, than production rate of $\pi^+\pi^-$. This is unexpected, since this indicates that t-channel photoproduction to 3-quarks and 3-antiquarks has the same rate as diffraction to 2-quarks and 2-antiquarks. Somewhat similarly large yield was observed by L3 collaboration on LEP [**6.1**], where they measured much higher $e^+e^- \rightarrow p\bar{p}$ cross section than what was expected from naive quark model. The inclusion of di-quarks in the model calculations gave the measured cross section. In our case also, it might be that photon diffraction is not just to 3-q and 3-$\bar{q}$, but to combination of di-quark pairs and $q\bar{q}$, **Figure 6.1** . Model calculations will be

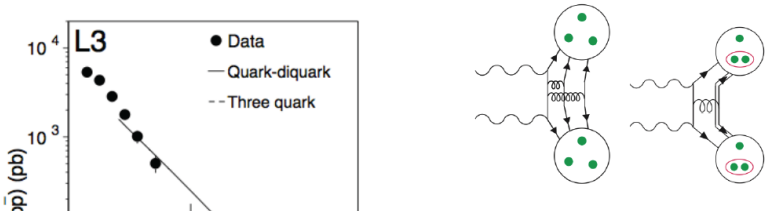

needed to understand underlying production mechanism. More details about di-quarks one can find in Appendix

This first results on coherent production of hadron pairs on deuterium showed promising avenue for studying meson resonances. Higher statistics experiments with some what higher energies will be needed for final resolution of previous claims. Observed large cross section of $p\bar{p}$ production requires more theoretical studies.

Appendix

❖ Sector by sector

➢ Particle identification

All procedures shown in section 4.2.2 have been done for all CLAS sectors. The mass squared have been calculated using the momentum, p, and velocity, β: $m^2 = \frac{p^2}{\beta^2/(1-\beta^2)}$, where β was defined using the measured time in scintillator counters (CLAS TOF counters), t_{SC}, and the path length from the production vertex to TOF counters, R_{SC}, measured by the DC tracking. In **Figure ap.1, ap.2** the mass squared distribution respectively for positively charged and negatively

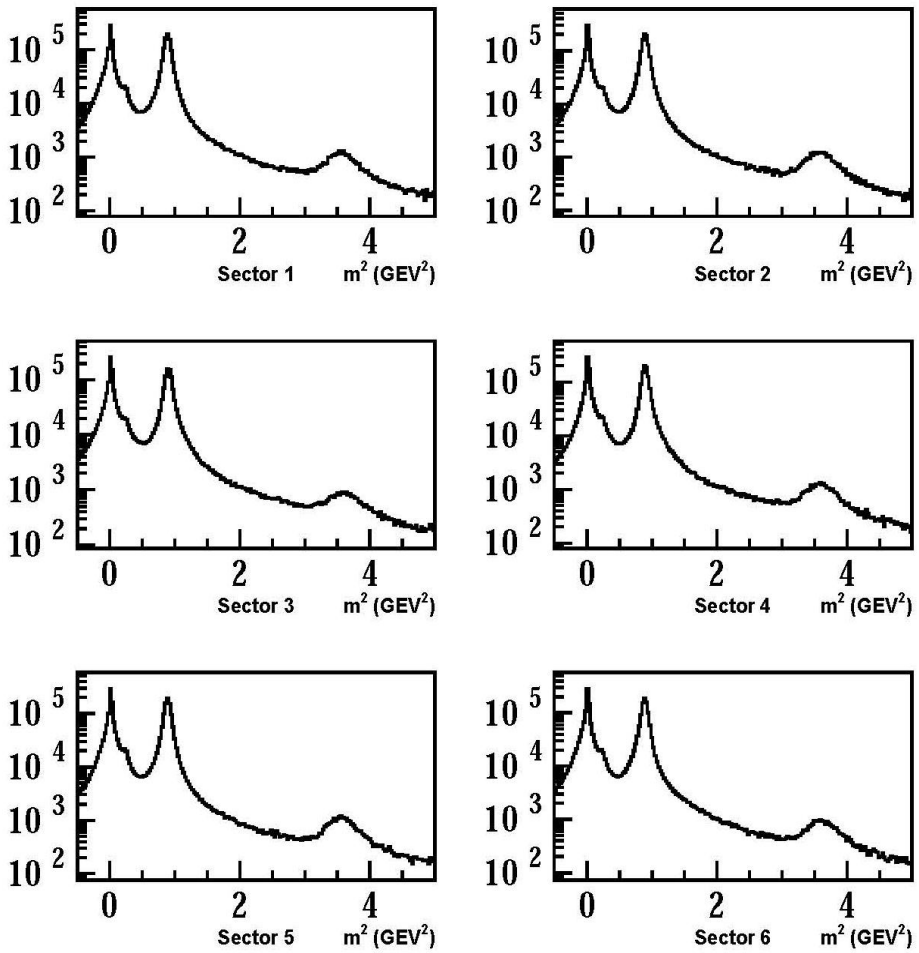

Figure ap.1. Mass square distributions for positively charged tracks.

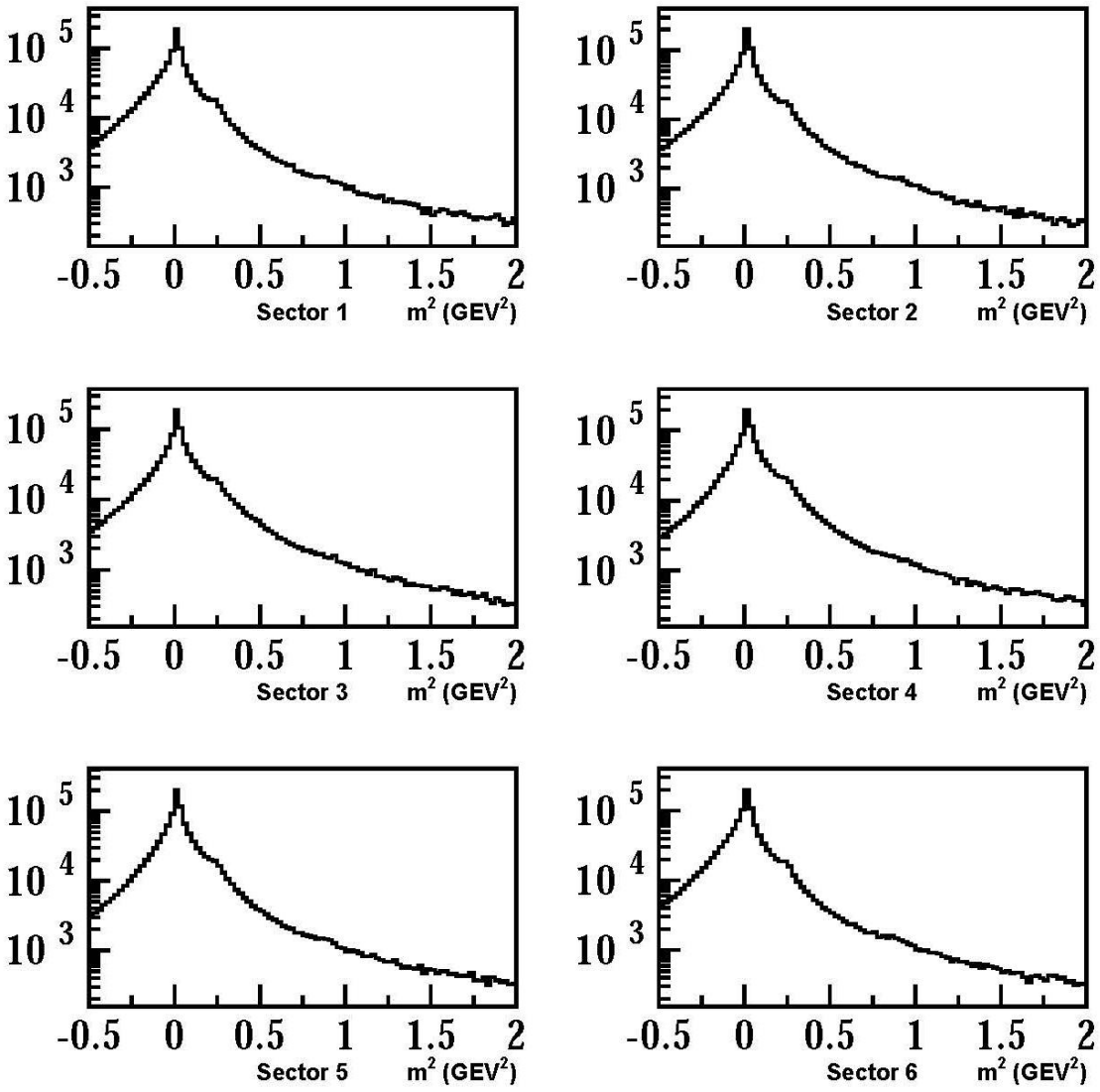

Figure ap.2. Mass square distributions for positively charged tracks.

➢ **Deuteron identification**

As mentioned in subsection **4.3.2,** for identification of deuteron candidates cut on the energy deposition in scintillator counters were applied, which is represented in **Figure ap.3**.

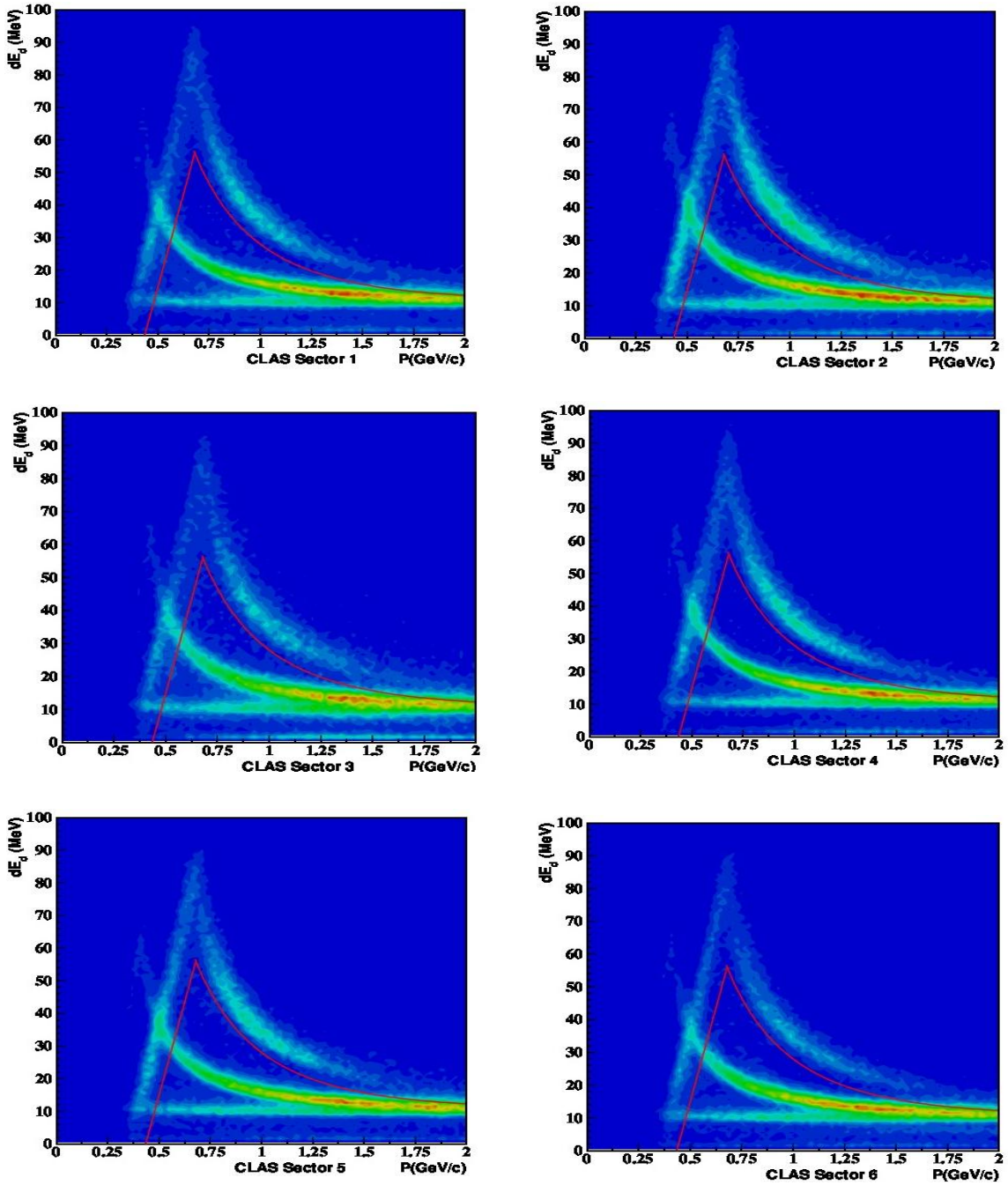

Figure ap.3. Energy loss in SC paddles by deuteron candi-dates as

The cut on deposited energy according to Equation (4.8) and (4.9) were used for deuteron in each sector of CLAS detector. The vertex time distribution of deuteron candidates as a function of momentum in each sector is shown in **Figure ap.4**.

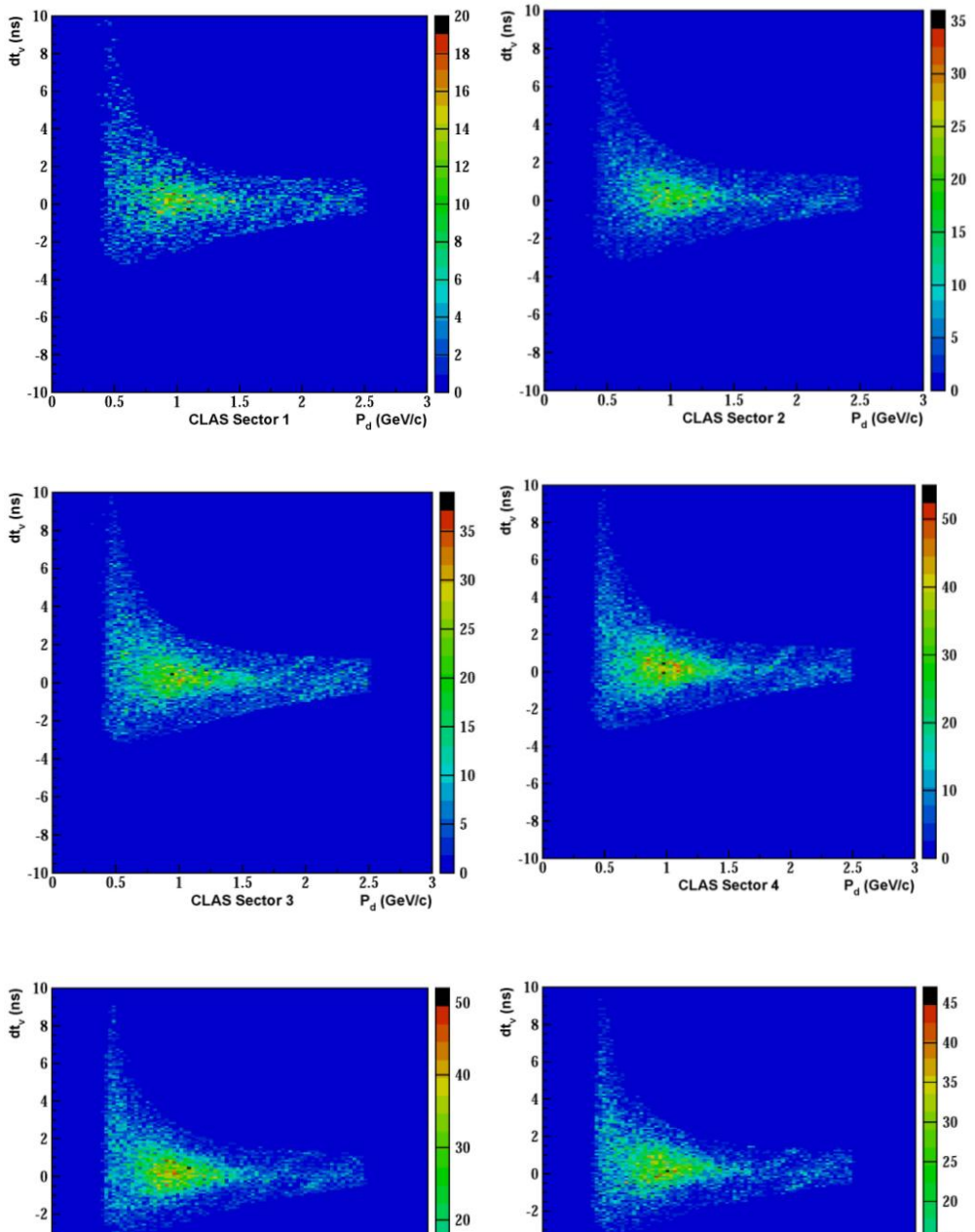

For final samples of deuteron selection $\pm 3\sigma$ cut on vertex time (**Equation 4.10)** were used for all 6 sectors. After cut on vertex time the energy loss of deuteron in scintillator counters as a function of deuteron momentum is represented in **Figure ap.5**, demonstrating a clean identification of deuterons.

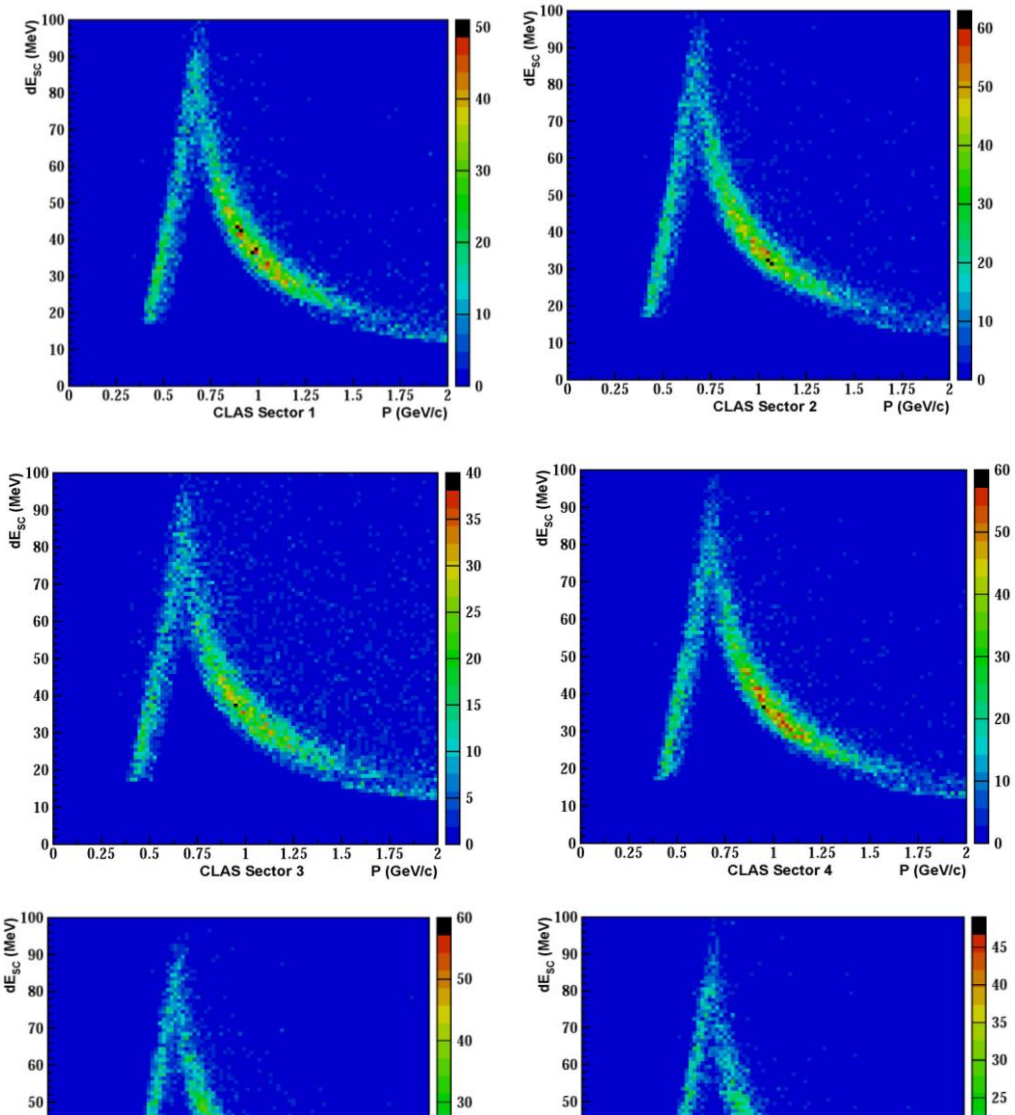

The scattering angle versus momentum for all three final state particles in $\pi^+\pi^-d$ reaction in each CLAS sector shown in **Figures ap.6, ap.7, ap.8.**

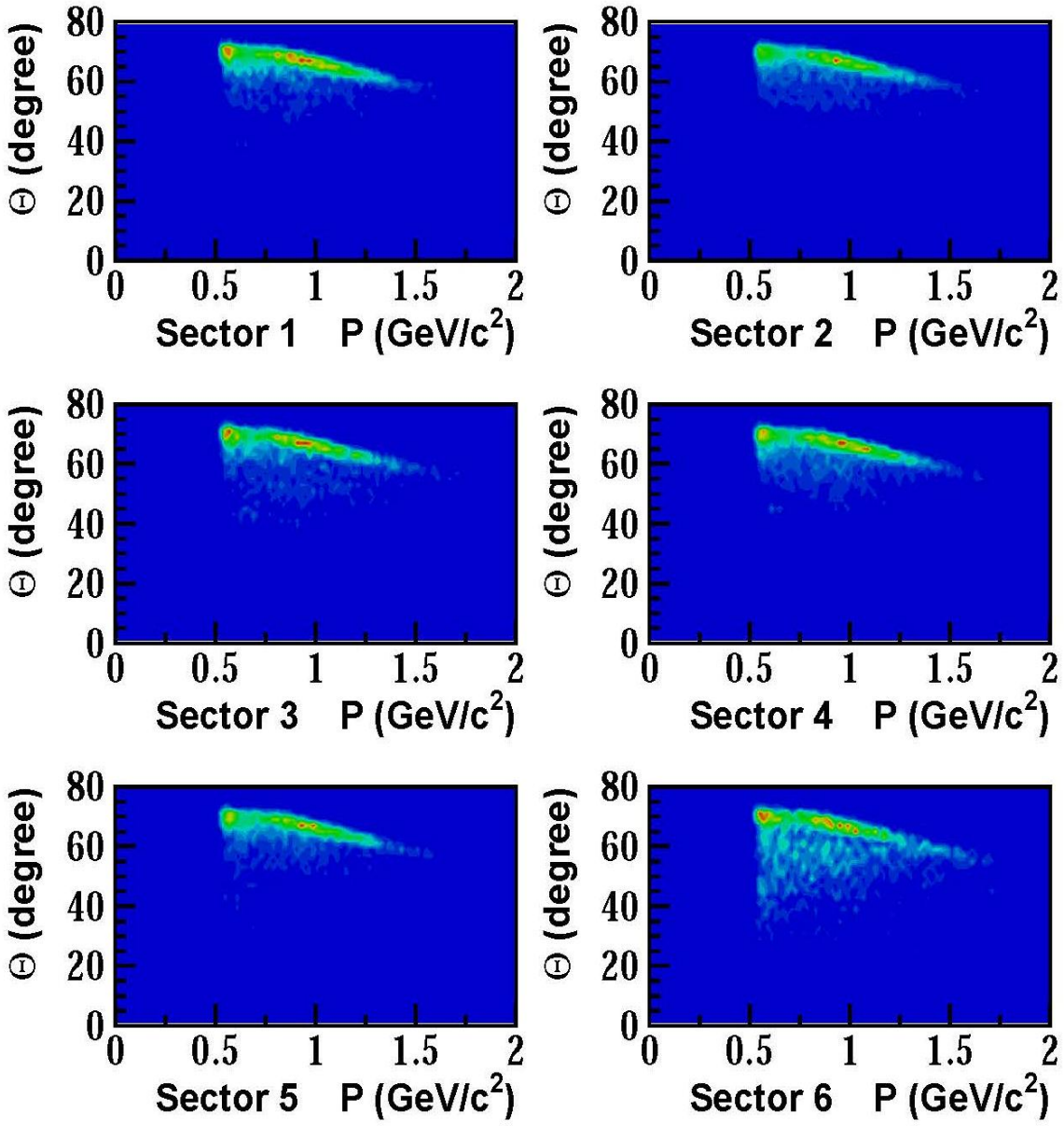

Figure ap.6. The scattering angle θ, vs momentum for deuteron for final $\pi^+\pi^-d$ events

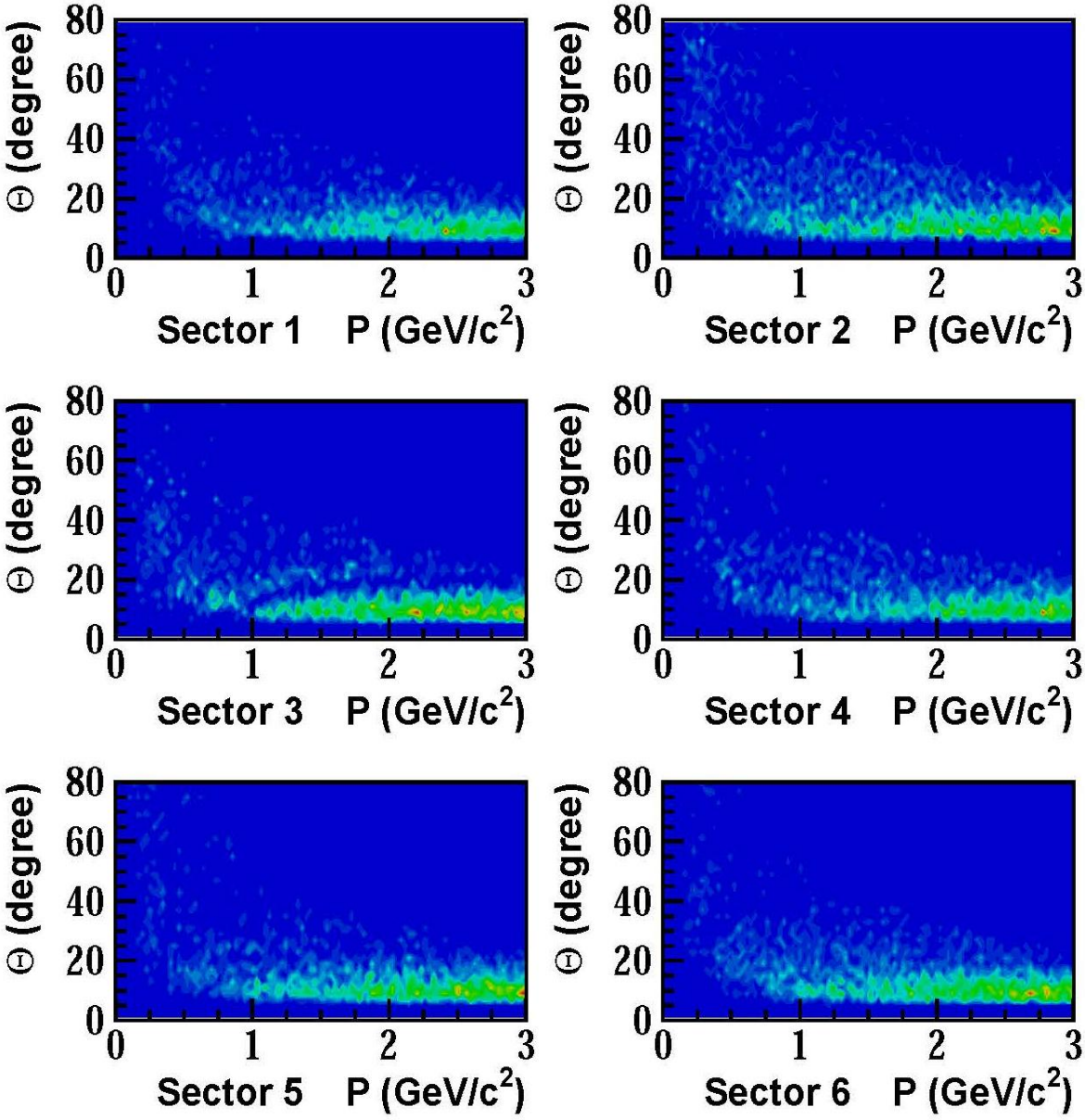

Figure ap.7. The scattering angle θ, vs momentum for π^- for final $\pi^+\pi^- d$ events

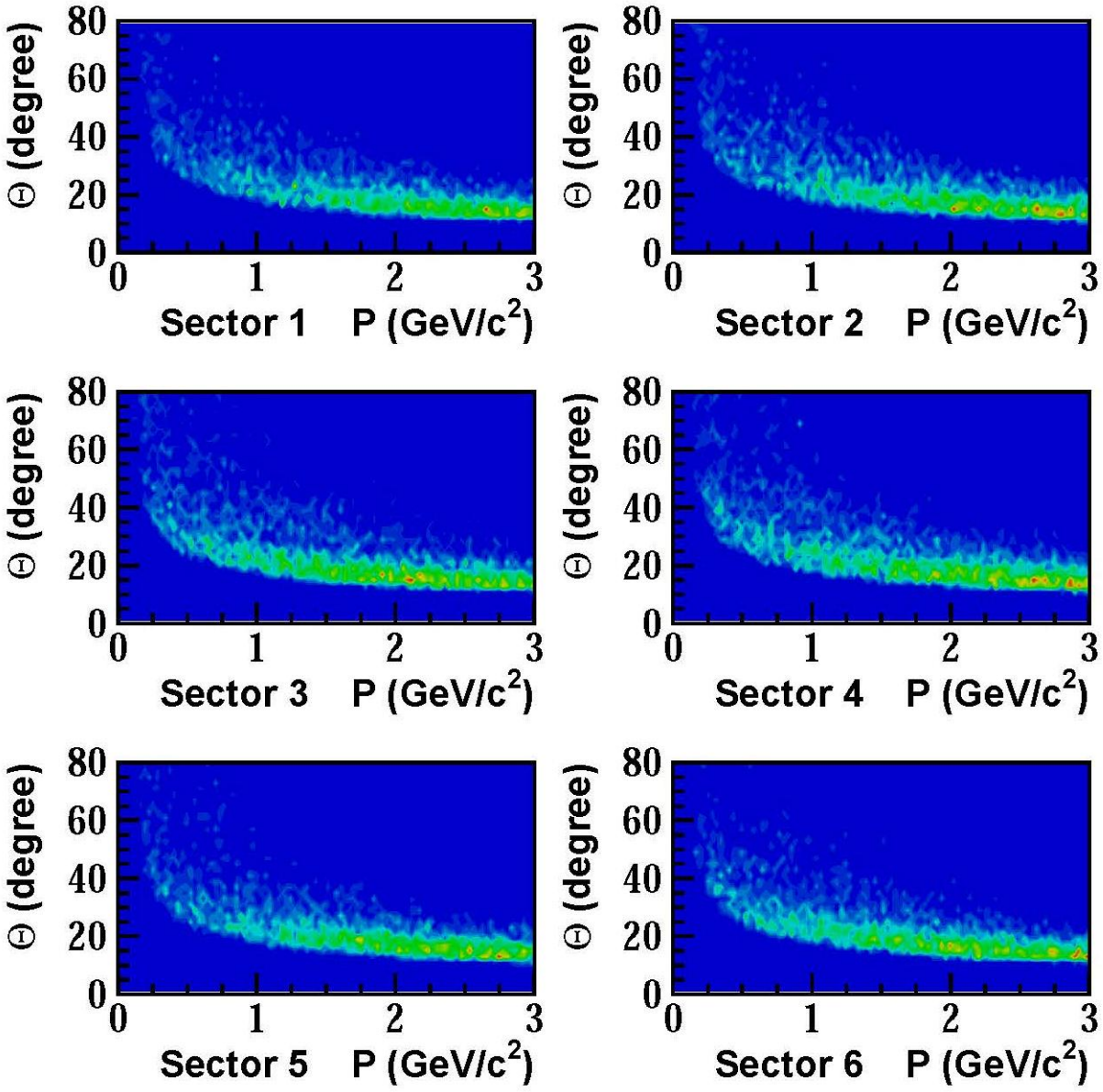

Figure ap.8. The scattering angle θ, vs momentum for π^+ for final $\pi^+\pi^-$d events

➢ **Final state K^+K^-d**

The scattering angle versus momentum for all three final state particles in K^+K^-d reaction in each CLAS sector shown in **Figures ap.9, ap.10, ap.11.**

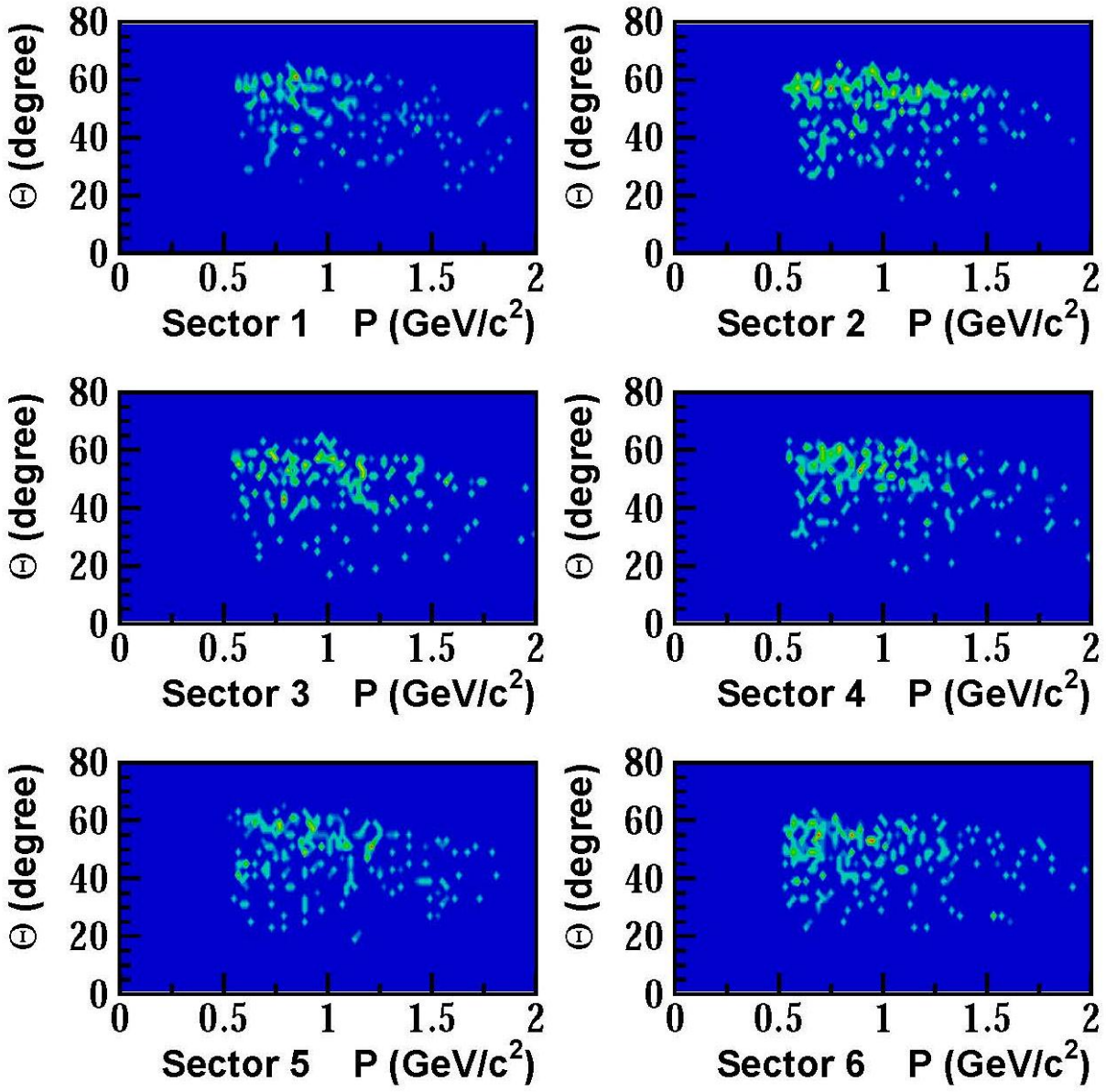

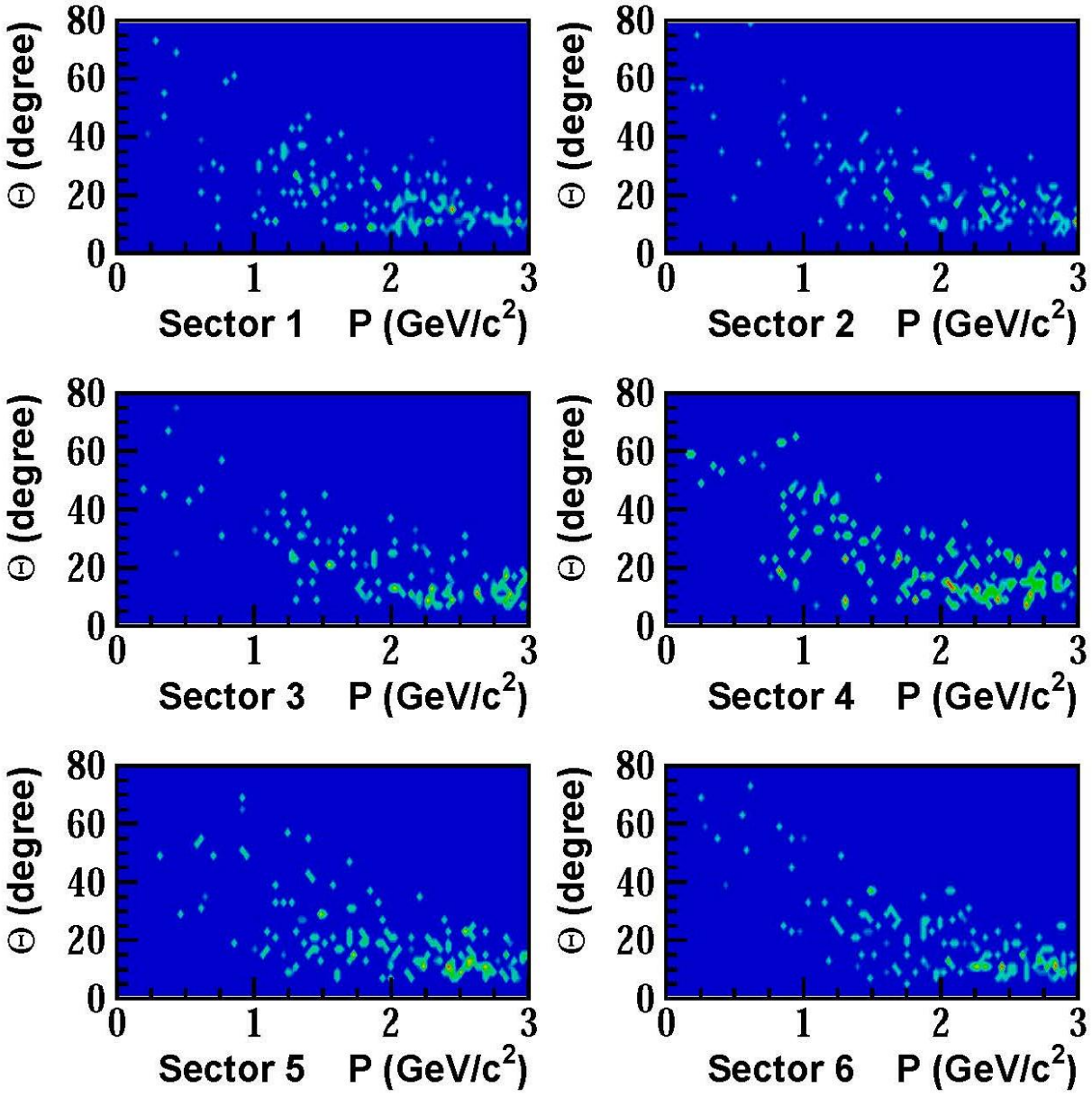
Θ (degree)
80
60
40
20
0
0
1
2
3
Sector 1 P (GeV/c²)
Sector 2 P (GeV/c²)
Sector 3 P (GeV/c²)
Sector 4 P (GeV/c²)
Sector 5 P (GeV/c²)
Sector 6 P (GeV/c²)

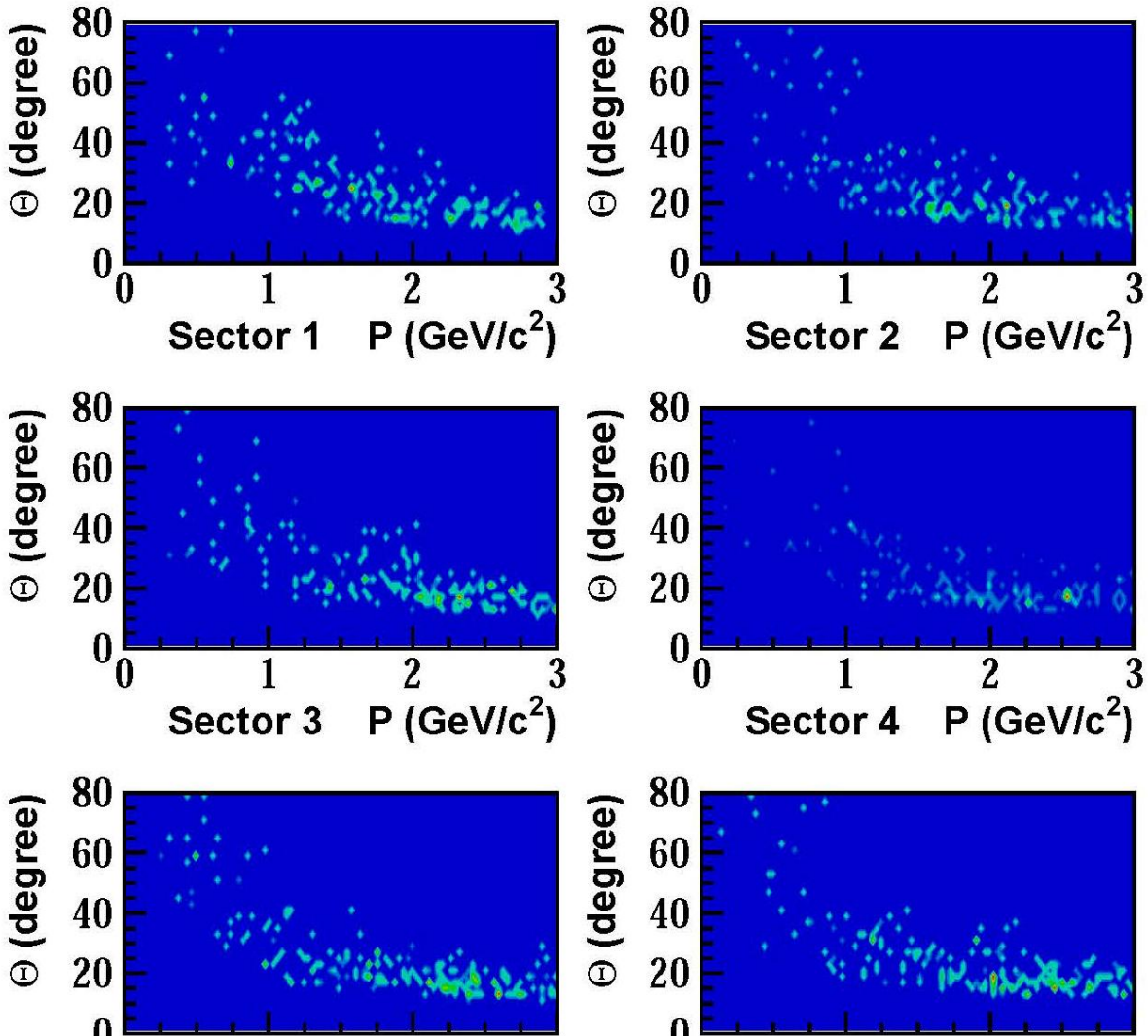
Θ (degree)
80
60
40
20
0
0
1
2
3
Sector 1 P (GeV/c²)
Sector 2 P (GeV/c²)
Sector 3 P (GeV/c²)
Sector 4 P (GeV/c²)

➢ **Final state $p\bar{p}d$**

The scattering angle versus momentum for all three final state particles in K^+K^-d reaction in each CLAS sector shown in **Figures ap.12, ap.13, ap.14.**

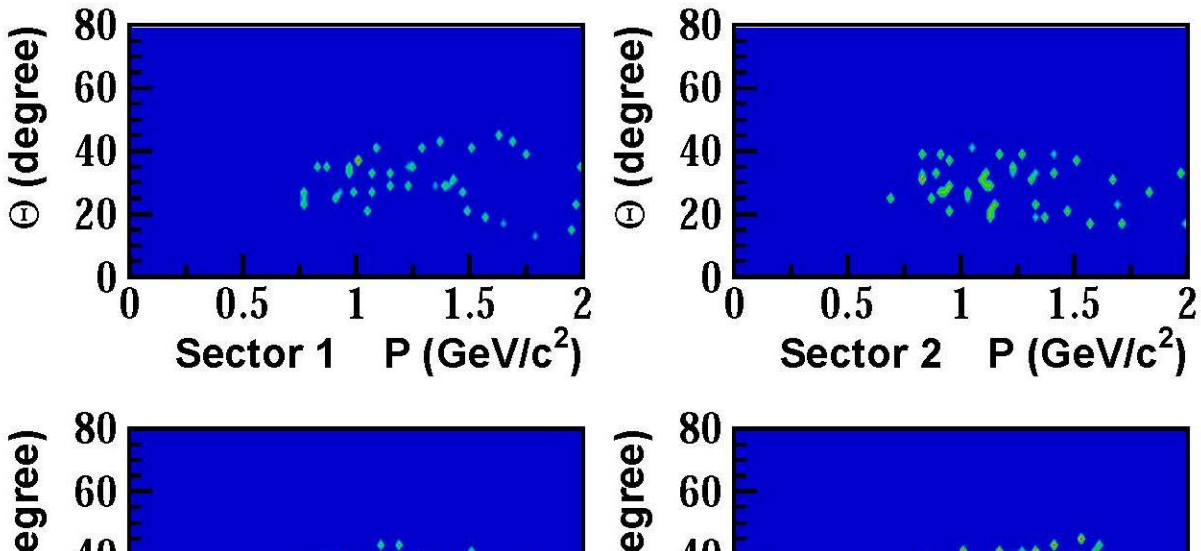

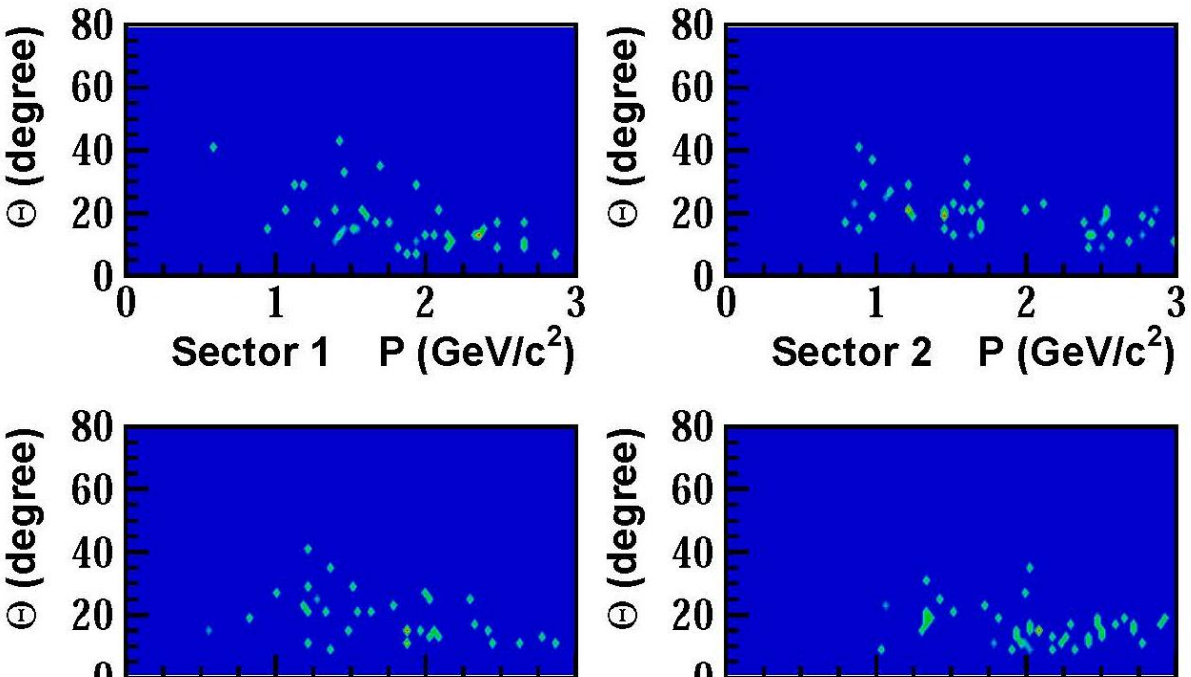
Θ (degree)
80
60
40
20
0
0
1
2
3
Sector 1 P (GeV/c²)
Sector 2 P (GeV/c²)

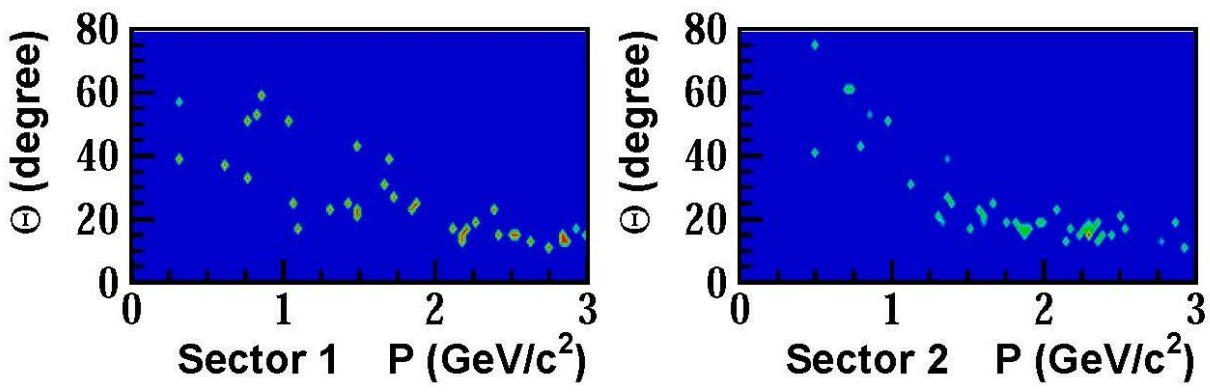
Θ (degree)
80
60
40
20
0
0
1
2
3
Sector 1 P (GeV/c²)
Θ (degree)
80
60
40
20
0
0
1
2
3
Sector 2 P (GeV/c²)

❖ Photon Flux for CLAS eg3 run period

As mentinoed in **Chapter 5**, **Equation 5.2,** Luminosity: $L = \frac{N_\gamma \cdot \rho_D \cdot l_t \cdot N_A}{A}$

where the N_γ was calculated using the "gflux" files for each of 205 production runs used for the analysis, ($\rho_D = 0{,}169\ g/cm^3$, $N_A = 6{,}022 \times 10^{23}\ mol^{-1}$, $l_t =$ 40 cm, A=1). One of the important pieces of the cross section calculation is the number of photons incident on the target at different energies, which is called photon flux (gflux: N_γ).

This analysis uses the tagger region corresponding to the energy of 4.5-5.5 GeV. During the photon calcutaion process, the gflux was calculated for each photon energy bin with the effciency of the tagger system already included.

As we talked in **Chapter 3** The CLAS tagging system tags bremsstrahlung photon with energies ranging from 25% to 95% of the incoming electron energy, which is about 1.15-5.50 GeV for eg3 run period and the photon flux for each 100 MeV Energy bin has been calculated. The total photon flux for all good runs for Energy E>4.5GeV is $\mathbf{N_\gamma = 12.72 \times 10^{12}}$

❖ Diquarks

A diquark [**7.1**][**7.2**], or diquark correlation/clustering, is a hypothetical state of two quarks grouped inside a baryon. Corresponding models of baryons are referred to as quark–diquark models. The diquark is often treated as a single subatomic particle with which the third quark interacts via the strong interaction. The existence of diquarks inside the nucleons is a disputed issue,

but it helps to explain some nucleon properties and to reproduce experimental data sensitive to the nucleon structure. Diquark–antidiquark pairs have also been advanced for anomalous particles such as the X (3872). The forces between the two quarks in a diquark is attractive when both the colors and spins are antisymmetric. When both quarks are correlated in this way they tend to form a very low energy configuration. This low energy configuration has become known as a diquark. Many scientists theorize that a diquark should not be considered a particle. Even though they may contain two quarks they are not colour neutral, and therefore cannot exist as isolated bound states. So instead they tend to float freely inside hadrons as composite entities; while free-floating they have a size of about 1 fm. This also happens to be the same size as the hadron itself. Diquarks are the conceptual building blocks, and as such give scientists an ordering principle for the most important states in the hadronic spectrum. There are many different pieces of evidence that prove diquarks are fundamental in the structure of hadrons. One of the most compelling pieces of evidence comes from a recent study of baryons. Diquarks are important in the formation and properties of baryonium and mesonlike semistable states. Many spin effects observed in high-energy exclusive reactions pose severe problems for the pure quark picture of baryons and might be explained by the introduction of diquarks as hadronic constituents. There is considerable controversy, not about the existence of diquarks in hadrons, but about their properties and their effects.

Bibliography

[**1.0**] Particle Data Group, http://particleadventure.org

[**1.1**] M.N. Focacci et al., *Mass Spectrum of bosons from 500 to 2500 MeV in the*

fraction $\pi^- + p \to p + X^-$ *observed by a missing-mass spectrometer.*

Phys. Rev. Lett. Vol.17, number 16, (1966), pp. 890-893

[**1.2**] D. Cline et al., *Energy-Dependent Structure in Backward-Hemisphere* $p\bar{p}$

Elastic Scattering and High-Mass Bosons.

Phys. Rev. Lett. Vol. 21, (1968), pp. 1268-1271

[**1.3**] R. Bizzarri et al., $p\bar{p}$ *backward scattering and s-channel resonances: Upper*

limit to the $p\bar{p}$ *coupling of the S(1929) meson.*

Phys. Rev.D, Vol. 6, Issue 1, (1972), pp. 160-163.

[**1.4**] A.S. Carroll et al., *Observation of structure in* $\bar{p}p$ *and* $\bar{p}d$ *total cross section*

below 1.1 GeV/c^*.

Phys. Rev. Lett. Vol. 32, number 5, (1974), pp. 247-250.

[**1.5**] T.E. Kalogeropoulos and G.S. Tzanakos, *Observations of narrow antiproton-neutron resonances near threshold.*

Phys. Rev. Lett. Vol. 34, Issue 16-21, (1975), p 1047.

[**1.6**] V. Chaloupka et al., *Measurement of the total and partial* $p\bar{p}$ *cross section between 1901 and 1950 MeV.*

Phys. Lett.B Vol.61, Issue 5, (1976), pp. 487-492.

[**1.7**] P. Benkheiri et al., *Evidence for two narrow* $\bar{p}p$ *resonances at 2020 MeV and 2200 MeV.*

Phys. Lett. Vol.B68, number 5, (1977), pp.483-486.

[**1.8**] B.G. Gibbard et al., *Cross sections and possible resonances in* $\bar{p}p$ *electroproduction.*

Phys. Rev. Lett. Vol. 42, number 24, (1979), pp. 1593-1596.

[**1.9**] S.U. Chung et al., *Search for narrow* $p\bar{p}$ *states in the reaction* $\pi^- p \to p\pi^- \bar{p}p$ *at 16 GeV/c.*

Phys.Rev.Lett 45, (1980), pp.1611-1614

[**1.10**] D. Aston et al., *Proton-antiproton states in high energy photoproduction.*

Phys. Lett., Vol.93B, number 4, (1980), pp.517-520.

[**1.11**] J. Bodenkamp et al., *Cross section and* $\bar{p}p$ *invariant mass distribution of the reaction* $\gamma p \to p\bar{p}p$ *at* $4.7 \leq E_\gamma \leq 6.6\ GeV$.

Phys. Lett.B, Vol.133, number 3,4, (1983), pp.275-278.

[**1.12**] A. Ferrer, A.A. Grigoryan, V.F. Perepelitsa, P. Sonderegger, *Comprehensive evidence for a narrow* $\bar{p}p$ *state of mass 2.02 GeV/*c^2.

Eur. Phys.J C10, (1999), pp.249-263.

[**1.13**] K. Abe et al. (Belle Collaboration), *Observation of* $B^\pm \to p\bar{p}K^\pm$.

hep-ex/0202017 (2002), pp.1-6

[**1.14**] J.Z. Bai et al. (BES Collaboration), *Observation of a near-threshold enhancement in the* $\bar{p}p$ *mass spectrum from radiative* $J/\psi \to \gamma p\bar{p}$ *decays.*

hep-ex/0303006 (2003), pp.1-5

[**1.15**] D. Bridges et all., *Anti-proton annihilations in deuterium at rest Into two pions: Evidence for* $\bar{\mathrm{p}}\mathrm{N}$ *bound states near threshold.*

Phys.Lett.B, Vol.180, Issue 3, (1986), pp.313-318

[**1.16**] O.D. Dalkarov et al., *Evidence for a bound NN(1870) state produced in the* $pd \to ps5\pi$ *reaction.*

Phys.Lett.B, Vol. 392, Issues 1-2, (1997), PP. 229-233.

[**2.1**] B.A. Mecking et al. *The cebaf large acceptance spectrometer (CLAS).*

NIM, A503, (2003), pp. 513–553.

[**2.2**] M.D. Mestayer et al. *The CLAS Drift Chamber System.*

NIM, A449, (2000), 81-111.

[**2.3**] G. Adams et al. *The CLAS Cerenkov Detector.*

NIM, A465, (2001), 414-427.

[**2.4**] E.S. Smith. *The time-of-flight system for CLAS.*

NIM, A432, (1999), 265-298.

[**2.5**] M. Amarian et al., *The CLAS Forward Electromagnetic Calorimeter.*

NIM, A460, (2001) 239-265.

[**2.6**] S.Taylor et al., *The CLAS Start Counter.*

NIM, A432, (2001), 484-493.

[**2.7**] D.I. Sobber et al., *The bremsstrahlung tagged photon beam in Hall B at JLAB.*

NIM, A440, (2000), 263-284.

[**2.8**] E. Pasyuk. *Energy loss corrections for charged particles in CLAS.*

CLAS Note, (2007-016), 2007

[**3.1**] CLAS-CVS packages/user_ana.

[**3.2**] E.S. Smith and S. Stepanyan, *Considerations for the eg3 hardware.*

CLAS-NOTE 2004-038

[**4.1**] L. Elouadrhiri, V. Burkert, S. Stepanyan, H.Egiyan. *Charged Particle Identification in CLAS.*

CLAS-Note 98-004

[**4.2**] Y.S. Ghandilyan. *Identification of multiparticle final states in completely*

exclusive reactions based on the topology and kinematics of events. **J.Contemp.Phys. 50(2015) no.4, 302-311**, Izv.Akad.Nauk Arm.SSR,Fiz. 50920150 no.4, 410-421

[**4.3**] CLAS collaboration (R. Dikson (Carnegie Mellon U., Pittsburg, Pennsylvania) et al.), *Photoproduction of the $f_1(1285)$ Meson*, **Phys.Rev. C93 (2016) no.6, 065202**

[**5.1**] L. Graham, K. Park, and R.Gothe. CLAS-AnalysisNote 2009-106.

[**5.2**] R.Giese, SLAC-178 (1974).

[**6.1**] L3 collaboration, *Proton-antiproton pair production in two-photon collisions at LEP*, **Physics Letters B 571 (2003), pp.11-20**

[**7.1**] https://en.wikipedia.org/wiki/Diquark

[**7.2**] M. Anselmino et al., *Diquarks*. **Rev.Mod.Phys. Vol.65, No.4, (1993), pp.1199-1233**